

# Title

Hamzah Hussain

University College London  
Department of Physics and Astronomy

Submitted to University College London in fulfilment  
of the requirements for the award of the degree of Doctor of Philosophy

Submitted 2020

# Declaration

I, Hamzah Hussain confirm that the work presented in this thesis is my own. Where information has been derived from other sources, I confirm that this has been indicated in the thesis.

# Abstract

# Acknowledgements

# Contents

<b>List of Figures</b>	<b>8</b>
<b>List of Tables</b>	<b>10</b>
<b>1 Introduction</b>	<b>11</b>
1.1 Author's Contributions . . . . .	13
<b>2 Neutrino Phenomenology and Double Beta Decay</b>	<b>14</b>
2.1 The Standard Model Neutrino . . . . .	14
2.2 Origins of Neutrino Mass . . . . .	15
2.2.1 Neutrino Mixing and Oscillation Phenomenology . . . . .	16
2.2.2 Oscillation in a Vacuum . . . . .	17
2.2.3 Oscillations in Matter . . . . .	18
2.2.4 Oscillations Parameters . . . . .	19
2.3 Mass Hierarchy . . . . .	20
2.3.1 CP Violation . . . . .	21
2.4 Beyond Standard Model Neutrino Mass . . . . .	21
2.4.1 Dirac Mass . . . . .	21
2.4.2 Majorana Mass . . . . .	22
2.4.3 See-Saw Mechanism . . . . .	23
2.5 Neutrino Mass Constraints . . . . .	24
2.5.1 Beta Decay . . . . .	24
2.5.2 Cosmological Constraints . . . . .	26
2.5.3 Neutrinoless Double Beta Decay . . . . .	27
2.6 Beta Decay . . . . .	28
2.7 Two Neutrino Double Beta Decay ( $2\nu\beta\beta$ ) . . . . .	30
2.8 Neutrinoless Double Beta Decay ( $0\nu\beta\beta$ ) . . . . .	31
2.8.1 Light Neutrino Exchange . . . . .	33
2.8.2 Majoron Emission . . . . .	34
2.8.3 Right Handed Current . . . . .	36
2.9 Open Questions on the Nature of Neutrinos . . . . .	38
2.9.1 CP Violation . . . . .	38
2.9.2 Single and Higher State Dominance . . . . .	38
2.9.3 Nuclear Matrix Elements . . . . .	38
<b>3 The SuperNEMO Demonstrator</b>	<b>39</b>
3.1 The SuperNEMO Demonstrator Design . . . . .	40

3.1.1	Detector Structure . . . . .	41
3.1.2	Commissioning Progress . . . . .	44
3.1.3	Detector Calibration . . . . .	46
3.1.4	Expected Sensitivity . . . . .	46
3.2	Backgrounds Sources . . . . .	46
3.2.1	Other DBD Experiments . . . . .	49
3.2.2	Magnetic Coil and Shielding . . . . .	49
3.3	Motivation for Magnetic Field Studies . . . . .	50
3.3.1	The Realistic Field . . . . .	51
3.3.2	Magnetic Shield Testing . . . . .	53
<b>4</b>	<b>Analysis Techniques</b>	<b>54</b>
4.1	Falaise . . . . .	54
4.1.1	Simulation . . . . .	55
4.1.2	Reconstruction . . . . .	56
4.1.3	Visualization . . . . .	56
4.1.4	Secondary Particle Information . . . . .	57
4.1.5	Sensitivity Module . . . . .	58
4.2	Reconstructed Topologies . . . . .	59
4.2.1	Electrons and Positrons . . . . .	59
4.2.2	Gammas . . . . .	60
4.2.3	Alphas . . . . .	61
4.3	Internal/External Hypothesis . . . . .	63
4.4	Number of Expected Events . . . . .	66
4.5	Half-Life Calculation . . . . .	67
4.5.1	Half Life Approximation . . . . .	68
4.6	Limit Setting Procedures . . . . .	70
4.6.1	Poissonian Window Approximation . . . . .	70
4.6.2	Helene Method . . . . .	70
4.6.3	Feldman-Cousins . . . . .	71
4.7	Minimum Detectable Activity . . . . .	71
<b>5</b>	<b>Double Beta Decay Event Selection</b>	<b>73</b>
5.1	Neutrinoless Double Beta Decay ( $0\nu\beta\beta$ ) . . . . .	73
5.2	Identifying Double Beta Events . . . . .	74
5.2.1	2e Channel Selection . . . . .	74
5.2.2	2e Channel Optimization . . . . .	75
5.2.3	Most Impactful Cuts . . . . .	77
5.3	Two Neutrino Double Beta Decay ( $2\nu\beta\beta$ ) . . . . .	78
5.3.1	SuperNEMO Sensitivity with $2\nu\beta\beta$ Background Only . . . . .	81
5.4	Summary of Double Beta Decays . . . . .	82

---

<b>6</b>	<b>Estimation of Backgrounds for SuperNEMO</b>	<b>83</b>
6.1	Background Classification and DBD Mimicking Mechanisms . . . . .	84
6.1.1	Internal Background . . . . .	84
6.1.2	Radon Backgrounds . . . . .	88
6.1.3	External Backgrounds . . . . .	89
6.2	Background Activities . . . . .	91
6.2.1	Table of Activities . . . . .	91
6.3	Background Simulations . . . . .	93
6.3.1	Table of Simulations . . . . .	93
6.4	Background Results . . . . .	94
6.4.1	Internal Backgrounds . . . . .	94
6.4.2	Radon Backgrounds . . . . .	98
6.4.3	External Backgrounds . . . . .	100
6.4.4	Total Background Contributions . . . . .	103
6.4.5	$\gamma$ Channels . . . . .	104
<b>7</b>	<b>Sensitivity And Optimization</b>	<b>105</b>
7.0.1	External Background Mechanism for DBD Candidates . . . . .	106
7.1	Background Optimization . . . . .	107
7.1.1	Minimum Opening Angle . . . . .	107
7.1.2	Minimum Angle Optimization . . . . .	108
7.1.3	No Adjacent Calorimeter Hits . . . . .	110
7.1.4	Tl Energy Split . . . . .	111
7.1.5	Optimization Results . . . . .	112
7.1.6	Window Region Optimization . . . . .	113
7.1.7	Final Sensitivities For The Three Magnetic Fields . . . . .	116
<b>8</b>	<b>Conclusion</b>	<b>117</b>

# List of Figures

2.1	Hierarchy [7] . . . . .	20
2.2	DiracCoupling [9] . . . . .	22
2.3	BetaSpectrum [11] . . . . .	25
2.4	msquared [12] . . . . .	26
2.5	HierarchyLimit . . . . .	27
2.6	SEMF [16] . . . . .	30
2.7	2vFeynman [16] . . . . .	31
2.8	0vFeynman [16] . . . . .	32
2.9	BlackBox [22] . . . . .	33
2.10	MajoronEmission [24] . . . . .	35
2.11	MajoronEnergies [25] . . . . .	35
2.12	0vRH [23] . . . . .	36
2.13	RHCurrents [26] . . . . .	37
3.1	DemonsDetector . . . . .	40
3.2	Isotope Properties . . . . .	42
3.3	TrackerCells . . . . .	42
3.4	GeigerMechanismtrum . . . . .	43
3.6	207BiSpectrum . . . . .	45
3.7	LIS . . . . .	46
3.8	Bi214DecayScheme . . . . .	47
3.9	Tl208DecayScheme . . . . .	48
3.11	A . . . . .	50
3.12	A . . . . .	51
3.13	A . . . . .	52
3.14	A . . . . .	53
4.1	Visualization of the Falaise pipeline structure, beginning with simulation and ending with the stored data banks for reconstructed data. . . . .	55
4.2	User interface of the Flvisualize tool used for visually displaying simulated and reconstructed events. The left hand side displays a 2D top view of the detector whereas the right hand side displays a 3D projection of the detector parallel to the foil. . . . .	57
4.3	Representation of a reconstructed event with two charged particle tracks, the first belonging to an electron (blue track) and the second to a positron (green track), with an initial decay vertex on the source foil. . . . .	60
4.4	Representation of a reconstructed event with one electron (blue track) as well as a photon (yellow calorimeter hit with an unassociated/dashed track), with an initial decay vertex on the source foil. . . . .	61



4.5	Representation of a reconstructed event with one electron (blue track) as well as an alpha (short red track), with an initial decay vertex on the source foil. . . . .	62
4.6	Internal probability for $0\nu\beta\beta$ , internal, radon and external backgrounds with reconstructed 2e topologies. The internal probability distributions were calculated using the equation above . . . . .	65
4.7	Energy spectra of $0\nu\beta\beta$ for all three magnetic field configurations, highlighting the region of interest (2.8 - 3.2 MeV) . . . . .	69
4.8	Helene where $\sigma_b$ is the error on the background and $\alpha$ is equal to 1 - CL . . . . .	71
5.1	2e energy spectra for $0/2\nu\beta\beta$ double beta candidate events. . . . .	79
5.2	Single electron energy spectra for $0/2\nu\beta\beta$ double beta candidate events. . . . .	80
5.3	$\text{Cos}\theta$ spectra for $0/2\nu\beta\beta$ double beta candidate events of all energies. . . . .	80
6.1	Illustrations of the dominant mechanisms, through which beta decaying internal backgrounds mimic double beta candidate events. . . . .	85
6.2	Simplified decay scheme for $^{208}\text{Tl}$ undergoing beta decay into $^{208}\text{Pb}$ , illustrating the most common transition lines, with the energies in keV. . . . .	86
6.3	Simplified decay scheme for $^{214}\text{Bi}$ undergoing beta decay into $^{214}\text{Po}$ , illustrating the most common transition lines, with the energies in keV. . . . .	87
6.4	A . . . . .	89
6.5	Illustrations of the dominant mechanisms, through which external backgrounds interacting with the source foil mimic double beta candidate events. . . . .	90
6.6	InternalSpectrum . . . . .	97
6.7	0 . . . . .	99
6.8	Energy spectra of all external $^{208}\text{Tl}$ double beta candidate events. . . . .	101
6.9	Energy spectra of all 8" Main wall backgrounds for no field. 1 billion . . . . .	102
7.1	Event display illustrating the mechanism resulting in external $^{208}\text{Tl}$ producing a double beta candidate event. . . . .	106
7.2	No field angular distributions for signal and backgrounds, including the theoretical maximum angle for two charged particles striking adjacent calorimeters (dashed line). . . . .	108
7.3	$\text{Cos}\theta$ distribution for different backgrounds, including the theoretical maximum angle for two charged particles striking adjacent calorimeters (dashed line). . . . .	108
7.4	Minimum opening angle vs sensitivity for the three magnetic field configurations. Maximal sensitivity is achieved around a minimum angle of $70^\circ$ . . . . .	109
7.5	Illustration of the adjacent calorimeter hit definition. Any hit within a block horizontally, vertically or diagonally adjacent to the original hit is labelled an adjacent calorimeter hit. . . . .	110

# List of Tables

1	- [6]	19
2	$0\nu\beta\beta$ cut flow for the three B field configurations. Each row lists a short description of the cut as well as the concurrent detection efficiency.	76
3	$2\nu\beta\beta$ cut flow and number of expected events for all three magnetic field configurations. Each row lists a short description of the cut as well as the concurrent detection efficiency for each magnetic field.	78
4	$0/2\nu\beta\beta$ detection efficiency as well as the number of expected events for $2\nu\beta\beta$	81
5	$0/2\nu\beta\beta$ detection efficiency as well as the number of expected events for $2\nu\beta\beta$	82
6	Total activities for all backgrounds simulated with an internal, radon and external vertex. The activity (mBq) for each isotope is given alongside the expected exposure of 6.25 Kg over 2.5 years of running time. For internal $^{208}\text{Tl}$ and $^{214}\text{Bi}$ the activities are provided as an upper limit. For the external backgrounds the listed activities are given in Bq.	91
7	Simulation vertex locations and the isotopes simulated at those locations	93
8	Internal $^{208}\text{Tl}$ cut flow for the three magnetic field configurations. Each row lists a short description of the cut as well as the concurrent detection efficiency.	94
9	Internal $^{214}\text{Bi}$ cut flow for the three magnetic field configurations. Each row lists a short description of the cut as well as the concurrent detection efficiency.	96
10	Number of expected events for all internal backgrounds for the three magnetic field configurations. The activities used to calculate the number of expected events are upper limits and so no systematic error is given.	97
11	Detection efficiency of all radon simulations for the three magnetic field configurations.	98
12	Number of simulations and expected events for external $^{208}\text{Tl}$ on the 8" Main wall PMTs for the three magnetic field configurations.	100
13	Number of expected events of the different background isotopes and their locations within the detector. The total number of expected backgrounds for all three magnetic fields is also provided.	103
14	$0\nu\beta\beta$ detection efficiency before and after the different optimization cuts.	112
15	Number of expected backgrounds before and after the different optimization cuts.	112
16	Signal detection efficiency, number of expected events and sensitivity to $0\nu\beta\beta$ for different regions of interest in the range from 2.6 to 3.2 MeV. Values provided are for the no field scenario after the additional minimum angle optimization.	114
17	Number of expected events for the most significant backgrounds as a with changing ROI	114
18	Signal detection efficiency, number of expected events and sensitivity to $0\nu\beta\beta$ for different regions of interest in the range from 2.6 to 3.2 MeV. Values provided are for the no field scenario after the additional minimum angle optimization.	116

# Chapter 1

## Introduction

Although neutrinos are the most abundant matter particles in the known Universe, their low interaction cross sections have made the neutrino one of the most mysterious particles in the Standard Model (SM) of particle physics. Historically, the Standard Model has been extremely successful at accurately predicting a number of parameters, most recently however, the discovery of neutrino oscillation was beyond any Standard Model prediction for the neutrino. Neutrinos were known to exist in three different flavour eigenstates,  $\nu_e$ ,  $\nu_\mu$  and  $\nu_\tau$  however the phenomenon of neutrino oscillation allows the neutrinos to mix between the different flavour eigenstates. Most importantly, the observation of neutrino oscillation proved that neutrinos were in fact massive particles, contradictory to the standard model prediction of massless neutrinos. Additionally, this raised the question of whether the non-zero neutrino mass is a Dirac or Majorana mass. If the neutrino has a Dirac mass, like the other Standard Model fermions, then the neutrino and anti-neutrino would be distinctly unique particles, whereas if the neutrino has a Majorana mass, the neutrino would be its' own antiparticle.

One such method for investigating the nature of neutrino mass is to examine the beyond Standard Model (BSM) interaction of neutrinoless double beta decay ( $0\nu\beta\beta$ ). Neutrinoless double beta decay is a hypothesised nuclear decay and the neutrinoless analogue of two neutrino double beta decay ( $2\nu\beta\beta$ ), which is an exotic rare nuclear decay resulting in the emission of two beta electrons and two associated neutrinos from the same nucleus. Observing neutrinoless double beta decay would affirm the Majorana nature of the neutrino whilst providing additional insight into the absolute neutrino mass scale and hierarchy.

Many experiments have been developed to probe and measure the hypothetical  $0\nu\beta\beta$  decay including the SuperNEMO detector, which is the successor to the previous NEMO-3 experiment that ran and collected data for number of different double beta decaying isotopes between 2003 and 2011. The complete SuperNEMO detector design comprises of 20 smaller demonstrator modules, each holding between 5 and 7 Kg of the double beta decaying isotope  $^{82}\text{Se}$ . Currently a single SuperNEMO demonstrator module is undergoing construction and commissioning in the Laboratoire Souterrain de Modane. The demonstrator module combines unique tracking and calorimetry techniques in order to study the 6.25 Kg of  $^{82}\text{Se}$  source foil located at the centre of the demonstrator. The tracking capabilities of the SuperNEMO demonstrator allows the trajectory of reconstructed charged particles to be determined with high accuracy in three dimensions and the segmented calorimeters allows for the energies of individual particles to be measured. Also, there is the option

to apply a magnetic field to the tracker volume, in order to identify particles via their curvature in response to the applied field. Reconstructed particle kinematics combined with particle identification can be used to efficiently reject multiple backgrounds, however the currently proposed magnetic field may in fact not provide the best performance for the demonstrator module and there is also the possibility of taking data without turning on the magnetic field from the beginning.

A short description of each chapter is provided below:

- i The first chapter includes an introduction to neutrino phenomenology as well as the underlying physics of double beta decay.
- ii Chapter two overviews the SuperNEMO experiment and demonstrator module, including the relevant backgrounds for  $^{82}\text{Se}$  double beta decay. Also, the definition of the realistic magnetic field is given \*\*\*
- iii Chapter three gives a description of the different analysis techniques used in the thesis, including the internal software package Falaise. Additionally, the reconstructed topologies of different particles are described and how they come together to measure particles in particular decay channels. Finally, the tools needed to estimate the total signal and background contributions as well as the overall sensitivity of the study are given.
- iv Chapter four provides an in depth description of the double beta decay event selection used to determine if a reconstructed event has a double beta topology. Furthermore, the detection efficiency for  $0\nu\beta\beta$  and the contribution from the irreversible background  $2\nu\beta\beta$  are discussed.
- v In chapter six, descriptions for the different classifications of backgrounds are provided and the contribution of those backgrounds to the  $^{82}\text{Se}$  sensitivity are shown.
- vi Chapter 7 discusses the optimization process for reducing the prominent backgrounds from the previous chapter and provides estimations for the overall sensitivity using the statistical approximations discussed in the analysis techniques chapter.
- vii The final chapter concludes the magnetic field study, providing suggestions for how to approach the installation of the magnetic field or whether a magnetic field should in fact be used with the SuperNEMO demonstrator module, based on the results of the study.

## 1.1 Author's Contributions

# Chapter 2

## Neutrino Phenomenology and Double Beta Decay

The neutrino was first proposed by Wolfgang Pauli in 1930, following observations of continuous energy spectra from  $\beta$  decay electrons. Pauli suggested the existence of a small uncharged particle, emitted alongside the  $\beta$  electron, allowing the decay to conserve energy, momentum and spin. Enrico Fermi coined the name neutrino in reference to the similarly uncharged neutron, following its discovery by James Chadwick in 1932.

Having no electric or colour charge made the neutrino very difficult to identify from low intensity beta decaying isotopes and it wasn't until the 1950s that experimental evidence of the neutrino was first discovered at the Savannah River Nuclear Reactor. **\*\*\*Ref\*\*\*** Cowan and Reines erected a nearby detector and successfully used the giant flux of antineutrinos coming from the reactor to illustrate the process of inverse beta decay, winning them the 1995 Nobel Prize. Over the following half century, further breakthroughs were made in the field of neutrino physics, including the discovery of multiple neutrino flavours,  $\nu_{electron}$ ,  $\nu_{muon}$  and  $\nu_{tau}$ , corresponding to the three charged leptons. In the late 1960s, the Homestake experiment first measured the incoming solar neutrino flux as roughly 1/3 to 1/2 of the hypothesised flux [1], ultimately resulting in the discovery of neutrino oscillation and non-zero neutrino mass.

### 2.1 The Standard Model Neutrino

The Standard Model of particle physics describes fundamental particles and their interactions through the three underlying forces, the electromagnetic, the strong nuclear and the weak nuclear force. It is a renormalizable quantum field theory with an  $SU(3) \times SU(2) \times U(1)$  symmetry, representing the strong, weak and electromagnetic interactions respectively.

$$\underbrace{SU(3)}_{Strong} \times \underbrace{SU(2) \times U(1)}_{Electroweak}$$

Predictions made by the Standard Model have been experimentally probed and proven to a high degree of accuracy, although the model falls short in certain aspects, in particular, the non-zero mass of neutrinos. Within the Standard Model neutrinos are massless, but we know, from observing oscillations, this is false. Fermions cannot have an explicit gauge invariant mass term

in the Standard Model Lagrangian and only gain their mass via spontaneous symmetry breaking. The absence of the right handed neutrino (or left handed anti-neutrino) does not allow the neutrino to couple to the Higgs and so the neutrino does not gain a Yukawa mass term from the Standard Model spontaneous symmetry breaking. The origin of neutrino mass is still unclear, however we know the Standard Model is wrong and neutrinos do have a non-zero mass.

Mass dirac vs Major \*\*\*

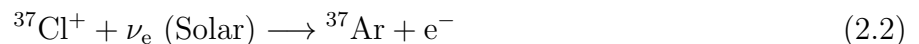
## 2.2 Origins of Neutrino Mass

Neutrino oscillation was first proposed by Bruno Pontecorvo, akin to the oscillation observed with Kaons,

$$K^0 \longleftrightarrow \bar{K}^0 \quad (2.1)$$

However, this proposal was rejected, as a massless neutrino should not undergo oscillation. Results from the Homestake [1] experiment indicated a deficit in the number of expected solar neutrinos, with only 1/3 of the expected number being measured during the experiment, indicating the solar neutrinos were undergoing some interaction causing the flux to reduce.

Electron neutrinos produced by proton-proton fusion in the centre of the sun were used to induce the radiochemical transmutation of  $^{37}\text{Cl}$  into  $^{37}\text{Ar}$  via the inverse beta process



Many tons of a  $^{37}\text{Cl}$  containing compound were used to interact with the solar neutrinos and the resulting  $^{37}\text{Ar}$  gas was collected and measured to estimate the neutrino interaction rate. The deficit of electron neutrinos found in the Homestake experiment was later dubbed the "Solar neutrino problem" and it wasn't until the end of the 20th century when experiments such as Kamiokande-II and SNO (Sudbury Neutrino Observatory) validated the results of the Homestake experiment and determined the number of solar electron neutrinos was suppressed as a result of neutrino oscillation [2].

Pontecorvos initial proposals made in [3] and [4] were and the neutrino was shown to have a non-zero mass contradictory to the Standard Model expectation. In response to the proposal of neutrino oscillations, theorists have postulated

The implication of this discovery

Oscillation -¿ Higgs coupling...?

Three flavour states from Z invisible width

PMNS

### 2.2.1 Neutrino Mixing and Oscillation Phenomenology

Neutrinos are produced in weak decays and are emitted in their weak flavour eigenstates  $\nu_e$ ,  $\nu_\mu$  and  $\nu_\tau$ . The flavour eigenstates propagate as plane waves corresponding to superpositions of the mass eigenstates  $\nu_1$ ,  $\nu_2$  and  $\nu_3$ . The mixing between the flavour states and the mass states is described by the unitary PMNS (Pontecorvo-Maki-Nakagawa-Sakata) matrix [5],

$$U_{PMNS} = \begin{pmatrix} U_{e1} & U_{e2} & U_{e3} \\ U_{\mu1} & U_{\mu2} & U_{\mu3} \\ U_{\tau1} & U_{\tau2} & U_{\tau3} \end{pmatrix} = \underbrace{\begin{pmatrix} 1 & 0 & 0 \\ 0 & c_{23} & s_{23} \\ 0 & -s_{23} & c_{23} \end{pmatrix}}_{\text{Atmospheric}} \underbrace{\begin{pmatrix} c_{13} & 0 & s_{13}e^{-i\delta} \\ 0 & 1 & 0 \\ -s_{13}e^{i\delta} & 0 & c_{13} \end{pmatrix}}_{\text{Cross-mixing}} \underbrace{\begin{pmatrix} c_{12} & s_{12} & 0 \\ -s_{12} & c_{12} & 0 \\ 0 & 0 & 1 \end{pmatrix}}_{\text{Solar}} \quad (2.3)$$

with  $c_{ij} = \cos \theta_{ij}$ ,  $s_{ij} = \sin \theta_{ij}$ .  $\theta_{ij}$  are mixing angles that have been experimentally calculated and represent the mixing between the mass stated  $i$  and  $j$ . Finally  $\delta$  represent the neutrino CP violating phase. If the neutrino is a Majorana particle (to be discussed in section 2.4.2), additional CP violating phases  $\alpha_1$  and  $\alpha_2$  can be added to the PMNS matrix in equation 2.3, by post-multiplication with the following,

$$\begin{pmatrix} e^{\frac{i\alpha_1}{2}} & 0 & 0 \\ 0 & e^{\frac{i\alpha_2}{2}} & 0 \\ 0 & 0 & 1 \end{pmatrix} \quad (2.4)$$

$U_{PMNS}$  relates the flavour and mass eigenstates as,

$$\begin{pmatrix} \nu_e \\ \nu_\mu \\ \nu_\tau \end{pmatrix} = \begin{pmatrix} U_{e1} & U_{e2} & U_{e3} \\ U_{\mu1} & U_{\mu2} & U_{\mu3} \\ U_{\tau1} & U_{\tau2} & U_{\tau3} \end{pmatrix} \begin{pmatrix} \nu_1 \\ \nu_2 \\ \nu_3 \end{pmatrix} \quad (2.5)$$

The mixing of flavour and mass eigenstates can be used to illustrate how neutrino oscillation implicitly infers the non-zero mass of neutrinos, starting with oscillations in a vacuum.



## 2.2.2 Oscillation in a Vacuum

From equation 2.3, the relationship between a single flavour and mass eigenstate can be written as,

$$|\nu_\alpha\rangle = \sum_i U_{\alpha i} |\nu_i\rangle \quad (2.6)$$

where  $\alpha$  represents the flavour states  $\nu_{e,\mu,\tau}$  and  $i$  the mass states  $\nu_{1,2,3}$ . The mass states  $\nu_i$  evolve according to the Schrödinger equation and so the time evolution of the mass eigenstate can be written as (in natural units),

$$|\nu_i(t)\rangle = e^{-i(E_i t - p_i L)} |\nu_i(0)\rangle \quad (2.7)$$

where  $L$  is the distance travelled and  $m_i$  the mass of the eigenstate.

The relativistic energy, as a result of the low neutrino mass, can be approximated as,

$$E_i = \sqrt{p_i^2 + m_i^2} = p_i \left(1 + \frac{m_i^2}{p_i^2}\right)^{1/2} \approx p_i + \frac{m_i^2}{2p_i} \quad (2.8)$$

and so the time evolution becomes,

$$|\nu_i(t)\rangle = e^{-i(m_i^2/2p_i)L} |\nu_i(0)\rangle \quad (2.9)$$

When taking  $E \approx p$  for the relativistic neutrino, equation 2.6 can be written as,

$$|\nu_\alpha(L)\rangle \approx \sum_i U_{\alpha i} e^{-i(m_i^2/2E)L} |\nu_i\rangle = \sum_{i,\beta} U_{\alpha i} U_{\beta i}^* e^{-i(m_i^2/2E)L} |\nu_\beta\rangle \quad (2.10)$$

The probability for  $\nu_\alpha$  oscillating to  $\nu_\beta$  is,

$$P(\alpha \rightarrow \beta)(L) = |A(\alpha \rightarrow \beta)(L)|^2 = |\langle \nu_\beta | \nu_\alpha(L) \rangle|^2 \quad (2.11)$$

where  $A$  is the transition amplitude for  $\nu_\alpha \rightarrow \nu_\beta$ .

Using equation 2.10, the transition probability is,

$$P_{\nu_\alpha \rightarrow \nu_\beta}(L) = \sum_{i,j} U_{\alpha i}^* U_{\beta i} U_{\alpha j} U_{\beta j}^* e^{-i(\Delta m_{ij}^2/2E)L} \quad (2.12)$$

with  $\Delta m_{ij}^2 = m_i^2 - m_j^2$  the mass difference between the two mass eigenstates.

According to equation 2.12, in order for oscillations to occur, the  $\Delta m_{ij}^2$  term must be non-zero.  $\Delta m_{ij}^2$  is a mass squared difference and so the absolute mass of the neutrino eigenstates cannot be determined directly from oscillations in a vacuum. By measuring the oscillation of one neutrino flavour to another, the mass squared difference can be determined by controlling for the distance travelled  $L$  and the energy of the neutrino  $E$ .

### 2.2.3 Oscillations in Matter

Neutrino oscillations also occur in matter, however the presence of significantly dense matter alters the behaviour of the neutrino as it passes through. Neutrinos of all flavours are able to interact with matter via neutral current interactions, exchanging an intermediary  $Z_0$  boson. However, the prevalence of electrons in matter, allows for the charged current interaction between the  $\nu_e$  and electron, with the exchange of a  $W^-$  boson, to occur. As a result, the flavour states undergo different interactions when traversing matter, altering the oscillatory behaviour of the neutrinos. The changing oscillatory behaviour of the neutrinos in matter is known as the Mikheyev-Smirnov-Wolfenstein or MSW effect.

One of the most important examples of the MSW effect is the propagation of solar neutrinos through the sun. The MSW effect is sensitive to both the electron density and neutrino energy. When neutrinos are produced in the centre of the sun, during proton-proton fusion, the significant density at the centre of the sun results in the neutrinos being skewed towards the heavier mass eigenstate. However as the density decreases away from the sun and eventually becomes negligible as the neutrino leaves the sun, the neutrino is in the mass eigenstate  $\nu_2$ , and so does not mix as it propagates through space until it reaches earth. Measuring these solar neutrinos provides data for the  $\Delta m_{21}^2$ .

\*\*\*\* Dirac mass and alpha term \*\*\*\*

## 2.2.4 Oscillations Parameters

Parameter	Value
$\sin^2(\theta_{12})$	$0.307 \pm 0.013$
$\Delta m_{21}^2$	$(7.53 \pm 0.18) \times 10^{-5} \text{ eV}^2$
$\sin^2(\theta_{23})$ IH	$0.539 \pm 0.022$
$\sin^2(\theta_{23})$ NH	$0.546 \pm 0.021$
$\Delta m_{32}^2$ IH	$(-2.524 \pm 0.034) \times 10^{-3} \text{ eV}^2$
$\Delta m_{32}^2$ NH	$(2.453 \pm 0.033) \times 10^{-3} \text{ eV}^2$
$\sin^2(\theta_{12})$	$(2.20 \pm 0.07) \times 10^{-2}$
$\delta$ CP violating phase	$1.36_{-0.16}^{+0.20} \pi \text{ rad}$
$\langle \Delta m_{21}^2 - \Delta \bar{m}_{21}^2 \rangle$	$< 1.1 \times 10^{-4} \text{ eV}^2, \text{ CL} = 99.7\%$
$\langle \Delta m_{32}^2 - \Delta \bar{m}_{32}^2 \rangle$	$(-0.12 \pm 0.25) \times 10^{-3} \text{ eV}^2$

Table 1: - [6]

The PMNS matrix shown in equation 2.3 has a number of measurable parameters as shown in table 1. Various neutrino based experiments have been run in the previous few decades in order to improve the constraints set on the PMNS parameters, particularly, the mixing angles and mass squared differences. Reactor and accelerator experiments are the primary detectors used for probing neutrinos and the associated PMNS parameters. Reactor experiments use neutrino fluxes from nearby nuclear reactors in order to measure the neutrino flux whereas accelerator experiments generate a neutron beam that is measured firstly at a near detector and finally at a far detector.

Neutrino oscillation experiments have continued to improve on the previously set constraints for the mixing angles and mass squared differences, however some questions continue to be left unanswered. Currently, only the sign of the  $\Delta m_{12}^2$  is measurable and so the ordering of the mass constraints is still unknown. Additionally, the CP violating parameters  $\delta$  and  $\alpha_i$  are still \*poorly understood.

## 2.3 Mass Hierarchy

Neutrino oscillation established the non-zero finite mass of the neutrino, antithetical to the Standard Model picture of the massless neutrino. Currently, the sign of the  $\Delta m_{32}$  term is indistinguishable resulting in the two hypothesised mass eigenstate orderings, the normal hierarchy (NH) and the inverted hierarchy (IH). Observations of the pure  $\nu_2$  solar neutrinos described in section 2.2.3 inferred the sign of the  $\Delta m_{21}$  term, confirming  $m_{\nu_1} < m_{\nu_2}$ . If the  $\Delta m_{32}$  sign is positive ( $\Delta m_{32} > \Delta m_{21} > 0$ ) the neutrino mass ordering follows the normal hierarchy, whereas if the  $\Delta m_{32}$  sign is negative ( $\Delta m_{32} < 0 < \Delta m_{21}$ ), the inverted hierarchy reigns. The NH and IH are illustrated in figure 2.1.

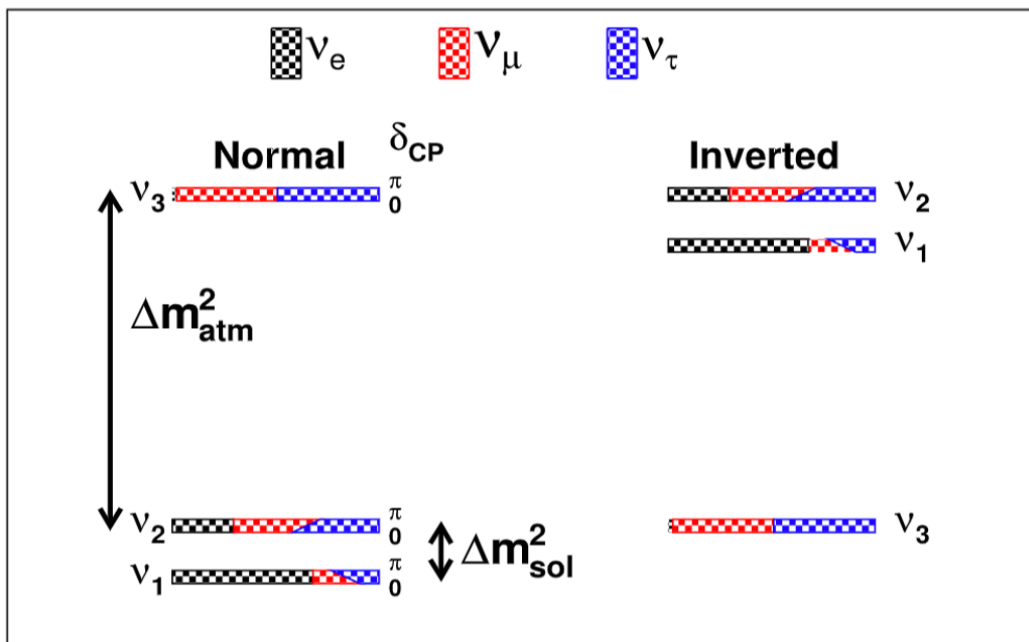


Figure 2.1: Hierarchy [7]

If the normal hierarchy is correct, the lightest mass eigenstate  $\nu_1$  would correspond strongly with the electron neutrino, analogous to the to the charged leptons, whereas, if the inverted hierarchy is proven, the lightest mass eigenstate would correspond strongly with the  $\nu_\mu$  and  $\nu_\tau$ . Ongoing experimental data puts a preference on the normal mass ordering, with a  $>2.5\sigma$  statistical significance, taking into account double beta decay, cosmological measurements and oscillation data [8], although \*\*\*

### 2.3.1 CP Violation

## 2.4 Beyond Standard Model Neutrino Mass

As previously highlighted, the standard model prediction of the massless neutrino has been demonstrably disproven by neutrino oscillation. However, there are several SM extensions that allow for a non-zero neutrino mass term, the most common of which are the Dirac and Majorana methods, which add BSM terms for the neutrino mass corresponding to the different neutrino types. The Dirac neutrino is similar to the other standard model leptons, having a distinct particle and anti-particle, whereas the Majorana neutrino is its own antiparticle. Additionally, the See-Saw mechanism proposes a combination of both Dirac and Majorana terms, where each light neutrino has an associated heavy but inert counterpart.

what's in section \*\*\*

### 2.4.1 Dirac Mass

In the Standard Model neutrinos are incorporated as left handed chiral particles, with no right handed equivalent and vice versa for the antineutrino. Charged leptons and quarks gain their mass through the Yukawa coupling of the left and right handed fields to the Higgs,. In order to couple neutrinos to the Higgs field a right handed neutrino field is added for each neutrino flavour, producing a Dirac mass term  $m_D$ .

The Dirac term in the Lagrangian manifests as,

$$\mathcal{L}^D = -\frac{1}{2}m_\nu^D \bar{\nu}\nu = -\frac{1}{2}m_\nu^D (\bar{\nu}_R\nu_L + \bar{\nu}_L\nu_R) \quad (2.13)$$

with the chirality operators  $P_L = \frac{1}{2}(1 - \gamma_5)$  and  $P_R = \frac{1}{2}(1 + \gamma_5)$  decomposing the neutrino into its left and right handed components. The Dirac neutrino mass term can then be defined as,

$$m_i = g_Y \frac{v}{\sqrt{2}} \quad (2.14)$$

The Dirac approach provides a simple lepton number conserving extension to the Standard Model for the purpose of adding the non-zero neutrino mass, although there are a several ramifications of this method. The Lagrangian includes the three right handed neutrino fields which only interact gravitationally (having no electric or weak charge), making them completely sterile to the other Standard Model particles. Additionally, the value of  $g_Y$  is inexplicably small, many orders of magnitude lower than the corresponding charged lepton couplings.

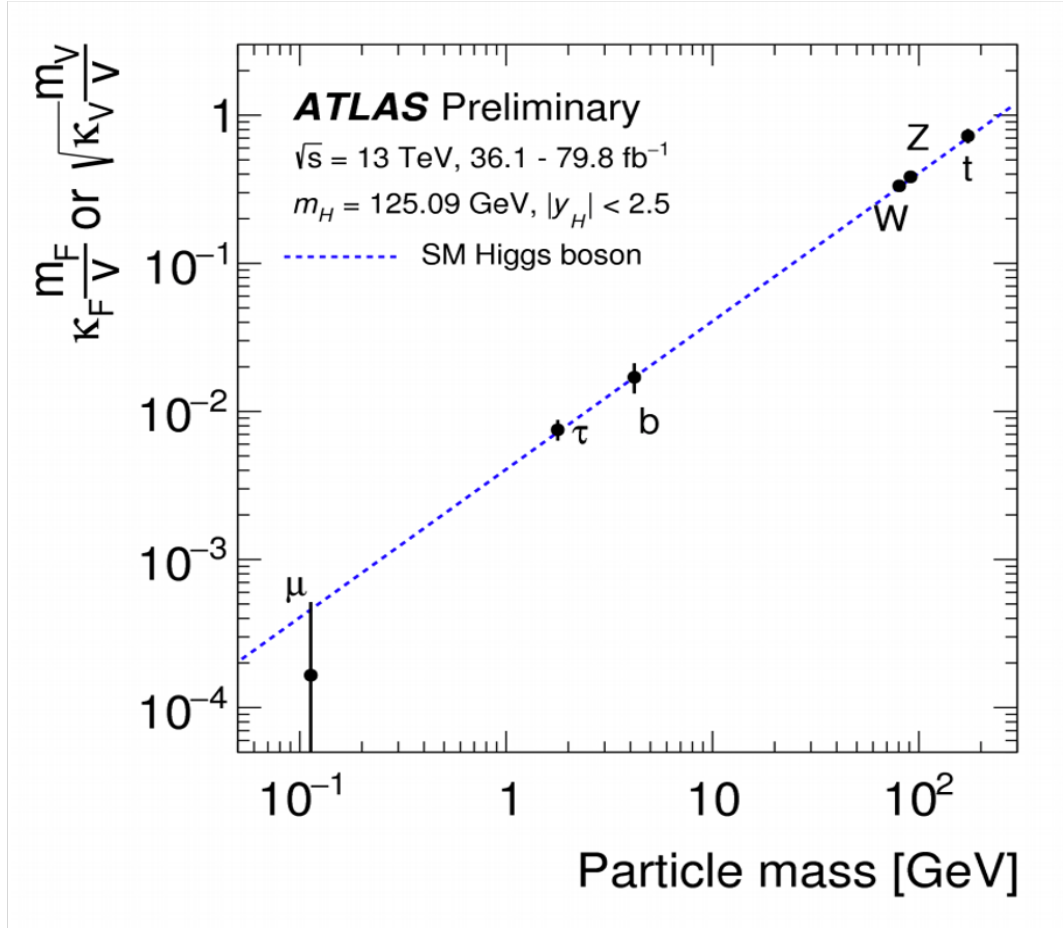


Figure 2.2: DiracCoupling [9]

### 2.4.2 Majorana Mass

The Dirac mass terms attempts to couple the left and right handed neutrino fields in a lepton conserving manner, with the addition of the sterile right handed neutrinos. However, in 1937, Ettore Majorana contemplated whether the left and right handed neutrinos were not independent particles [10] and were in fact related by a charge conjugation shown in equation 2.15,

$$\nu_R = \xi \mathcal{C} \bar{\nu}_L^T \quad (2.15)$$

with  $\xi$  an arbitrary phase factor,  $\mathcal{C}$  the charge conjugation matrix and  $\nu_R$  and  $\nu_L$  the two measured neutrino fields. As shown in equation 2.13, the neutrino can be decomposed into its left and right handed components,

$$\nu = \nu_L + \nu_R \quad (2.16)$$

and using using 2.15 can be rewritten as,

$$\nu = \nu_L + \mathcal{C}\bar{\nu}_L^T = \nu_L + \nu_L^c \quad (2.17)$$

Taking the charge conjugation of the Majorana neutrino and using  $\hat{C}|\psi\rangle = C|\bar{\psi}\rangle$ ,

$$\nu^c = (\nu_L + \nu_L^c)^c = \nu_L^c + \nu_L = \nu \quad (2.18)$$

inferring the neutrino and its charge conjugate are the same particle. Particles which are their own antiparticles are characterized as Majorana particles. Of all the Standard Model fermions, only the neutrino is capable of being a Majorana particle due to its neutral charge. The Majorana term in the Lagrangian is,

$$\mathcal{L}^M = -\frac{1}{2}m_\nu^M \bar{\nu}_L^c \nu_L \quad (2.19)$$

with  $m_\nu^M$  the Majorana mass term. Using the Majorana Lagrangian term, neutrinos are able to acquire mass without a Yukawa coupling, however lepton conservation is violated in the process. Like the Dirac mechanism, the Majorana mass term requires a sterile right handed neutrino, although the Majorana mass provides a better explanation of the difference between the neutrino and charged lepton masses.

### 2.4.3 See-Saw Mechanism

The See-Saw mechanism combines both the Dirac and Majorana mass terms into a single Lagrangian term,

$$\begin{aligned} \mathcal{L}^{D+M} &= \mathcal{L}^D + \mathcal{L}^M \\ &= -\frac{1}{2}m_\nu^D (\bar{\nu}_R \nu_L + \bar{\nu}_L \nu_R) - \frac{1}{2}m_\nu^M \bar{\nu}_L^c \nu_L + h.c. \\ &= -\frac{1}{2} \begin{pmatrix} \bar{\nu}_L & \bar{\nu}_L^c \end{pmatrix} \begin{pmatrix} m_L & m_D \\ m_D & m_R \end{pmatrix} \begin{pmatrix} \nu_R^c \\ \nu_R \end{pmatrix} + h.c \end{aligned} \quad (2.20)$$

The neutrinos in equation 2.20 are not the mass eigenstates because the mass matrix is not diagonal. To find the mass eigenvalues  $m_1$  and  $m_2$ , the mass matrix is first diagonalised, giving

$$m_{\pm} = \frac{1}{2} \left( m_L + m_R \pm \sqrt{(m_L - m_R)^2 + 4m_D^2} \right) \quad (2.21)$$

The See-Saw mechanism  $m_L = 0$  and  $m_D \ll m_R$ , so that the two mass eigenstates become,

$$m_+ \approx m_R \text{ and } m_- \approx \frac{m_D^2}{m_R} \quad (2.22)$$

and the mixing angle

$$\tan(2\theta) = \frac{2m_D}{m_R - m_L} \quad (2.23)$$

The See-Saw mechanism predicts the existence of a heavy GUT scale sterile neutrino, which has a mass of  $m_R$  and a light neutrino of mass  $\frac{m_D^2}{m_R}$ . The heavy sterile neutrino is almost entirely composed of the  $\nu_R$  field explaining why it is unobserved whereas the light neutrino is almost entirely composed of the  $\nu_L$  field, corresponding to the observed left handed neutrino. The type 1 See-Saw mechanism introduces one heavy sterile neutrino for each of the neutrino flavours, independent of an extremely low Yukawa coupling and could potentially explain the minute mass of the neutrino and its partiality for left handedness at current observable energies. The right handed GUT scale neutrino may also provide further insight into matter-anti matter asymmetries, CP violation and beyond standard model Grand Unification Theories if neutrinos are found to be Majorana particles.

Only looking at type 1

## 2.5 Neutrino Mass Constraints

The four main types of experiments used for extracting constraints on the neutrino mass are oscillation, Tritium beta decay cosmology models and finally neutrinoless double beta decay ( $0\nu\beta\beta$ ).

\*\*\*\*\* complete \*\*\* Neutrino experiments have provided constraints on the

KATRIN experiment mass limit for  $\nu_e$

Oscillation parameters already discussed and shown in figure 1, get mass squared differences

### 2.5.1 Beta Decay

Tritium undergoes beta decay into Helium,





with a decay energy of 18.6 KeV. The energy of the electron follows a beta decay spectrum as shown in figure \*\*\* ref. The  $\nu_e$  emitted during the decay reduces the energy of the beta electron, lowering the endpoint of the electron energy spectrum.

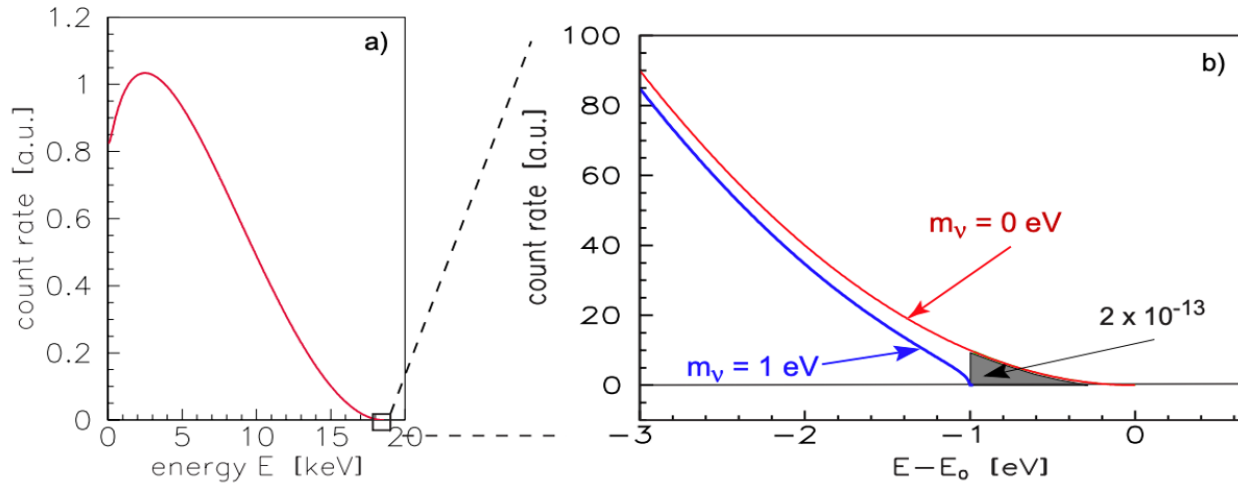


Figure 2.3: BetaSpectrum [11]

By measuring the energy loss of the beta electron with a massive and massless neutrino, the average of the neutrino mass weighted by the mass state coupling to  $\nu_e$ ,

$$\langle m_\beta \rangle = \sqrt{\sum_i |U_{ei}|^2 m_i^2} \quad (2.25)$$

As the beta decay energy of tritium is of low energy, the endpoint is more sensitive to  $\langle m_\beta \rangle$  shifts in the beta electron spectrum, making it a particularly good decay for probing the electron neutrino mass especially considering the simplicity of the decay. The Karlsruhe Tritium Neutrino (KATRIN) experiment currently holds the best upper limit on the mass of the electron neutrino, at  $\langle m_\beta \rangle < 1.1$  eV (at 90% CL)[12], an improvement on the previous upper limit of  $\langle m_\beta \rangle < 2$  eV (at 95% CL) [13]. The KATRIN experiment is expected to improve the sensitivity on  $m_\nu$  by an order of magnitude, to roughly 0.2 eV (at 90% CL), in the next couple of years [12].

\*\*\* find way to talk/reference this \*\*\*

\*\*\*advantage of tritium? \*\*\*

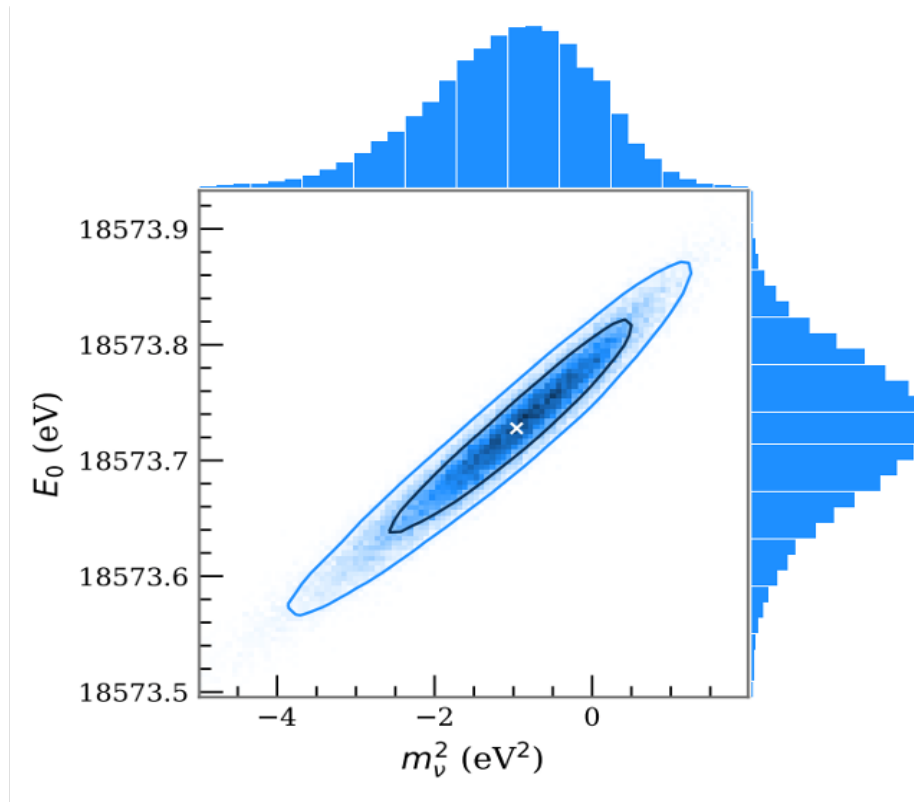


Figure 2.4: msquared [12]

### 2.5.2 Cosmological Constraints

Cosmological observations can yield limits on the sum of the neutrino masses, by combining a number of cosmological observables. Neutrinos played a significant role in the structure and development of the early universe and the influence of neutrinos can be measured using a number of different tools, including, baryonic acoustic oscillation in the cosmic microwave background (CMB), CMB temperature anisotropy and large scale structure formation. Using the minimal  $\Lambda$ CDM +  $\Sigma m_\nu$ , with the most up to date CMB data, the 95% confidence limit for the  $\Sigma m_\nu$  bounds are  $\Sigma m_\nu < 0.12$  eV,  $\Sigma m_\nu < 0.15$  MeV and  $\Sigma m_\nu < 0.17$  MeV for the degenerate, normal and inverted hierarchies respectively [14]. Additionally, the normal hierarchy is mildly preferred to the inverted hierarchy.

The constraints calculated using cosmological data are very dependent on the model used.

results depend on model \*\*\*

\*\*\* CMB picture \*\*\*

### 2.5.3 Neutrinoless Double Beta Decay

If neutrinoless double beta decay is observed and the neutrino shown to be a Majorana particle, the decay could be used to determine the absolute mass of the Majorana neutrino. Using the light neutrino exchange mechanism \*\*\*discussed ref\*\*\* discussed in section\*\*\*, the effective mass of the Majorana neutrino is,

$$\langle m_{\beta\beta} \rangle = \left| \sum_i U_{ei}^2 m_i \right| \quad (2.26)$$

The effective mass of the Majorana neutrino ( $\langle m_{\beta\beta} \rangle$ ) provides a constraint on the limits for the mass of the lightest mass eigenstate dependant upon the correct mass hierarchy. The current best limit on the effective Majorana neutrino mass comes from the KamLAND-Zen experiment [15]. For neutrinoless double beta decay mediated by light neutrino exchange, the upper limit for  $\langle m_{\beta\beta} \rangle$ , derived from the decay half-life, was measured as 61 - 165 meV, shown in figure 2.5, alongside the normal and inverted hierarchy regions for  $\langle m_{\beta\beta} \rangle$  vs  $m_{lightest}$  [15]. The upper limit is given as a range to reflect the uncertainty on the nuclear matrix element calculations.

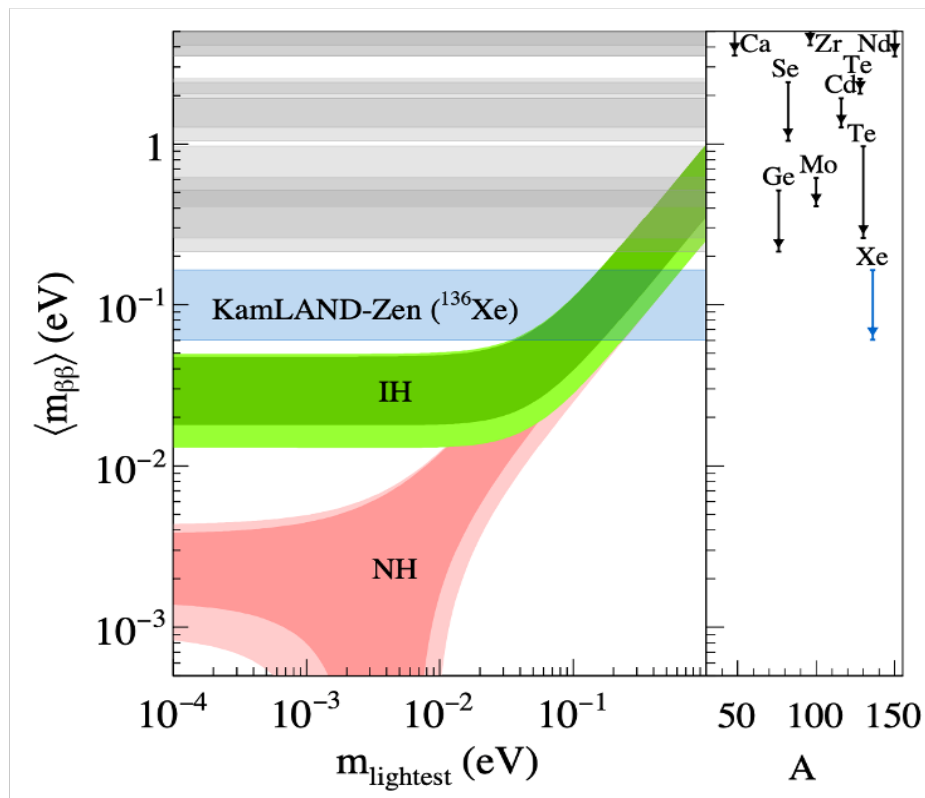


Figure 2.5: HierarchyLimit

An upper limit of 61 - 165 meV almost completely negates the possibility of the effective neutrino mass being found in the quasi-degenerate region, which combines predictions from the normal and inverted hierarchy. Next generation  $0\nu\beta\beta$  experiments are expected to reduce this upper limit in order to validate or deny the presence of the effective neutrino mass in the inverted hierarchy region. Limits on the effective Majorana neutrino mass only hold true if the neutrino is in fact a Majorana particle. If no evidence for  $0\nu\beta\beta$  is found, the limits for observing the decay and identifying neutrinos as Majorana particles becomes more stringent. Neutrinoless double beta decay experiments aim to answer the ongoing question of whether neutrinos are Dirac or Majorana particles. Observations of neutrino oscillation already proved that neutrinos are not massless as currently described in the Standard Model and so the current role of neutrino experiments are to identify the absolute masses of the different neutrino flavour and mass eigenstates whilst attempting to decipher if neutrinos are Majorana particles that fulfil the requirement of being their own antiparticle.

discussed in section **\*\*\*red\*\*\***,

## 2.6 Beta Decay

Beta decay is a type of radioactive nuclear decay, in which a atomic nucleus undergoes a transmutation from one element into another with the emission of a beta particle alongside a corresponding neutrino, conserving both Baryon and Lepton numbers. Beta decay is a weak force, charged current interaction, mediated by a  $W^\pm$  boson. Three different beta decays are commonly observed,  $\beta^-$  decay,  $\beta^+$  decay and electron capture, resulting in the emission of either a neutrino or antineutrino.  $\beta^-$  decay occurs when a neutron decays into a proton, producing an electron and lepton number conserving antineutrino,

$$n \rightarrow p + e^- + \bar{\nu}_e \quad (2.27)$$

$\beta^+$  decay occurs with the decay of a proton into a neutron, emitting a positron and neutrino,

$$p \rightarrow n + e^+ + \nu_e \quad (2.28)$$

and finally, electron capture occurs when an electron is captured by an atomic proton, which decays into a neutron, similar to  $\beta^+$  except with the emission of a sole neutrino.

$$p + e^- \rightarrow n + \nu_e \quad (2.29)$$

For  $\beta^\pm$  decays to occur, the daughter nuclei must have a lower energy than the decaying nuclei, with the energy difference used to create the emitted particles. Moreover, the energy difference must exceed the rest mass energy of the charged lepton and neutrino, with the additional energy providing the particles kinetic energy. Knowing the decay energy of a beta decaying isotope and

measuring the energy of the beta electron provides the energy of the neutrino without directly measuring it. The decay energy is extracted using the mass of the parent and daughter nuclei, which are calculated using the Semi-Empirical Mass Formula (SEMF). The SEMF estimates the mass of an atomic nucleus given the atomic and molecular numbers, in order to determine if the daughter nuclei has a lower energy than the parent, making the decay energetically possible.

The semi-empirical mass formula takes the form,

$$m = Zm_p + (A - Z)m_n - a_V A + a_s A^{2/3} + a_c \frac{Z^2}{A^{1/3}} + a_A \frac{(A - 2Z)^2}{A} + \delta(A, Z) \quad (2.30)$$

where,

$$\delta(A, Z) = \begin{cases} \frac{a_p}{A^{1/2}} & N \text{ even } (A \text{ even}) \\ 0 & A \text{ odd} \\ \frac{-a_p}{A^{1/2}} & N \text{ odd } (A \text{ even}) \end{cases} \quad (2.31)$$

and  $m$  is the mass of the nucleus,  $A$  the mass number and  $Z$  the atomic number. From left to right, terms one and two approximate the mass of the individual nucleons inside the atom. The remaining terms describe the corrections to the mass, from volume, surface, Coulombic, neutron/proton asymmetry and nucleus spin coupling. In an attempt to describe the energetically viable beta decays, the atomic number  $Z$  is plotted below, for a fixed even mass number  $A$ ,

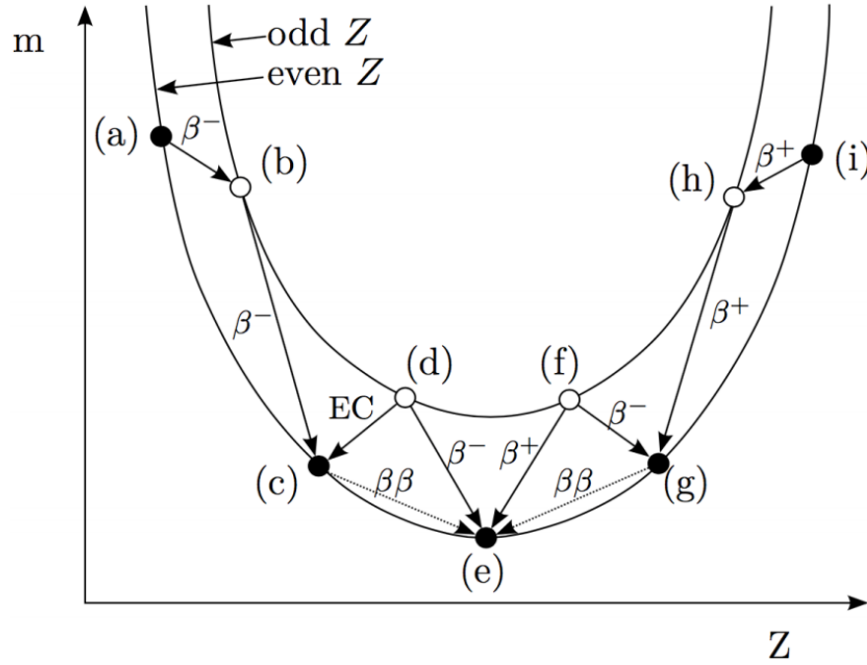


Figure 2.6: SEMF [16]

For an odd value of  $A$ , there is only one curve for  $Z$ , however, as shown in figure 2.6, for an even value of  $A$ , there are two curves, separated by the  $\delta(A, Z)$  term described in equation 2.31. The possible  $\beta^\pm$  transitions between the even and odd  $Z$  curves are shown by the arrows in figure 2.6.

## 2.7 Two Neutrino Double Beta Decay ( $2\nu\beta\beta$ )

As shown in section 2.6, equation 2.30 can be used to determine the mass of a nuclei and whether a particular decay is energetically permitted. For an isotope that is unable to decay directly via beta decay, such as isotope (c) in figure 2.6, it is possible for them to decay via double beta decay. During double beta decay, two neutrons simultaneously undergo  $\beta^-$  decay, resulting in the emission of two electrons and two corresponding electron neutrinos for the two neutrino variation of double beta decay,

$$(A, Z) \rightarrow (A, Z + 2) + 2e^- + 2\bar{\nu}_e \quad (2.32)$$

Double beta decay was first proposed by M. Goepfert-Mayer in 1935 [17] and has been observed in a number of isotopes that have their regular beta decay rate suppressed or forbidden. Like single beta decay, the two emitted electrons lead to a continuous energy spectrum that has an end point at the decay energy  $Q^{\beta\beta}$ .  $2\nu\beta\beta$  has been measured for isotopes including  $^{82}\text{Se}$ ,  $^{100}\text{Mo}$  and  $^{136}\text{Xe}$  and is currently a possible decay for 35 different isotopes. Of the measured double beta decaying

isotopes, the NEMO-3 experiment studied 7 [18], including  $^{82}\text{Se}$  which is the isotope of choice for the SuperNEMO experiment. The reasons for which  $^{82}\text{Se}$  was chosen as the source for SuperNEMO will be discussed further in chapter 3.

$2\nu\beta\beta$  is a second order weak interaction that is allowed in the Standard Model, but is extremely rare, with a measured half-life of the order  $10^{20}$  years. The Feynman diagram of the decay is shown in figure 2.7,

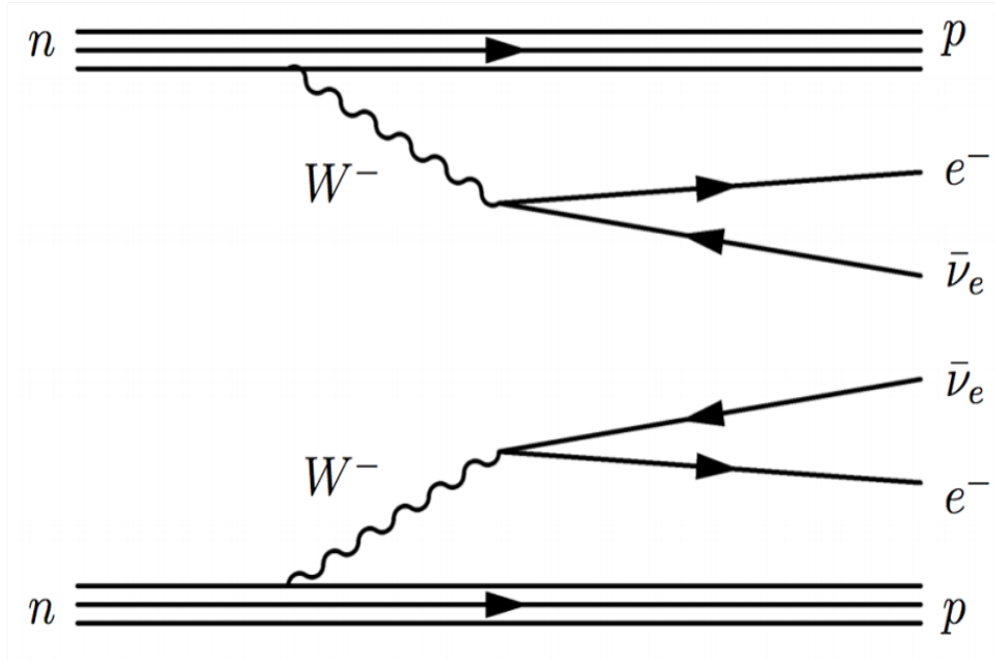


Figure 2.7:  $2\nu\beta\beta$  Feynman [16]

From [19], the half-life  $(T_{1/2}^{2\nu})^{-1}$  of the decay is related to the phase space factor  $G^{2\nu}(Q_{\beta\beta}, Z)$  and the nuclear matrix element  $M^{2\nu}$  as,

$$(T_{1/2}^{2\nu})^{-1} = G^{2\nu}(Q_{\beta\beta}, Z) |M^{2\nu}|^2 \quad (2.33)$$

$G^{2\nu}$  is a four body phase space factor that is calculated analytically and  $M^{2\nu}$  represents the transition probability from the initial to the final state of the decay. Measuring double beta decaying isotopes reduces the uncertainties on the values of  $M^{2\nu}$  improving the precision of the calculated half-life and phase space factors.

## 2.8 Neutrinoless Double Beta Decay ( $0\nu\beta\beta$ )

\*\*\*eegy spectrum 0 vs 2ν.

Neutrinoless double beta decay is the neutrinoless analogue of the double beta decay presented in the previous section and is a hypothesised decay which if observed would demonstrate that the neutrino is a Majorana particle [20].  $0\nu\beta\beta$  was first proposed by W.H. Furry in 1939 [21], as an alternative to the two neutrino decay making the decay a possibility for all double beta decaying isotopes. During neutrinoless double beta decay, two beta electrons are simultaneously emitted, however unlike the two neutrino decay, no antineutrinos are emitted and all the decay energy is carried by the two electrons,

$$(A, Z) \rightarrow (A, Z + 2) + 2e^- \quad (2.34)$$

Without emitting the two associated antineutrinos,  $0\nu\beta\beta$  violates lepton number conservation and is therefore a forbidden standard model interaction. The hypothesised mechanisms through which the neutrinoless decay is thought to occur include light neutrino exchange (neutrino mass mechanism), right handed current, Majoron emission and the more exotic R-parity violating supersymmetry, extra dimensions and squark mixing. If  $0\nu\beta\beta$  is observed, light neutrino exchange is the most natural and expected method of decay as it most closely resembles the current Standard Model decay. Figure 2.8 illustrates neutrinoless double beta decay via light neutrino exchange, where a right handed antineutrino emitted from one  $W$  boson is absorbed as a left handed neutrino, if neutrinos are Majorana particles. \*\*\*not mention exotic decays\*\*\*

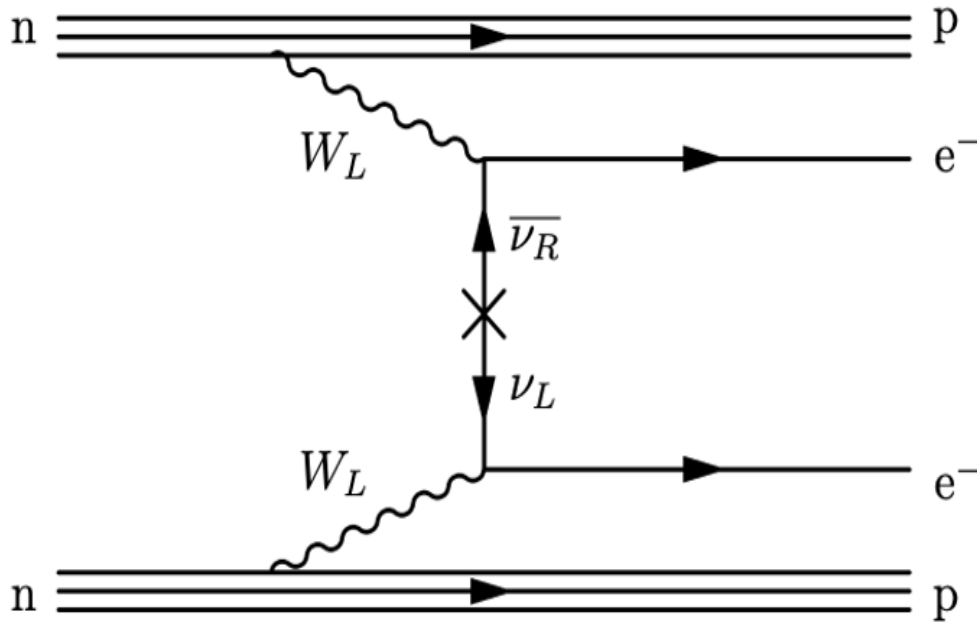


Figure 2.8:  $0\nu\beta\beta$  Feynman [16]

The light neutrino exchange mechanism in figure 2.8 clearly illustrates the Majorana nature of neutrinos however, amongst the other  $0\nu\beta\beta$  mechanisms, neutrinos are often not involved making



conclusions regarding the nature of the neutrino less obvious. In 1980, Schechter and Valle [22] illustrated that for any  $0\nu\beta\beta$  decay, regardless of the beyond Standard Model intermediary process, neutrinos are Majorana even though they are not directly involved in the decay. The  $0\nu\beta\beta$  mechanism can therefore be replaced with a 'Black Box' that is independent of the decay mechanism as shown in figure 2.9.

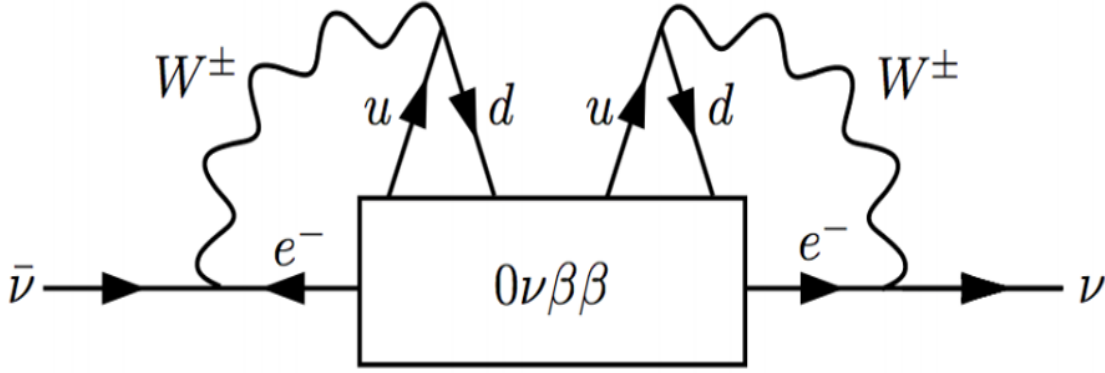


Figure 2.9: BlackBox [22]

For  $0\nu\beta\beta$  decay, the decay rate takes the form,

$$(T_{1/2}^{0\nu})^{-1} = G^{0\nu} (Q_{\beta\beta}, Z) |M^{0\nu}|^2 \eta_{LV}^2 \quad (2.35)$$

where  $G^{0\nu}$  is the two particle phase space factor,  $M^{0\nu}$  the nuclear matrix element for the neutrinoless decay transmission and  $\eta_{LV}$  the lepton number violating parameter that is unique to each of the decay mechanisms. Light neutrino exchange, right handed current and Majoron emission will be briefly discussed in the following sections, focusing on the relationship between the decay mechanism and the corresponding decay rate.

### 2.8.1 Light Neutrino Exchange

As mentioned, light neutrino exchange is the proposed interaction that most closely resembles a current Standard Model interaction, shown in figure 2.8. The decay rate for this interaction is,

$$(T_{1/2}^{0\nu})^{-1} = G^{0\nu} (Q_{\beta\beta}, Z) |M^{0\nu}|^2 \langle m_{\beta\beta} \rangle^2 \quad (2.36)$$

where the lepton number violating parameter in equation 2.35, is replaced by the effective Majorana mass  $\langle m_{\beta\beta} \rangle$ .  $\langle m_{\beta\beta} \rangle$  is defines as,

$$\langle m_{\beta\beta} \rangle = \left| \sum_i U_{ei}^2 m_i \right| \quad (2.37)$$

and for three light active neutrinos with mass  $m_i$ , \*\*\*wording\*\*\*

$$= \left| \cos^2 \theta_{13} (m_1 \cos^2 \theta_{12} + m_2 e^{i\alpha_1} \sin^2 \theta_{12}) + m_3 e^{i(\alpha_2 - 2\delta)} \sin^2 \theta_{13} \right| \quad (2.38)$$

using the PMNS matrix shown in equation 2.3 and the Majorana phases in equation 2.4. From equation 2.38, the decay rate of the light neutrino exchange is sensitive to the absolute scale of the neutrino mass eigenstates.

\*\*\* add more \*\*\*

## 2.8.2 Majoron Emission

\*\*\* talk about B-L \*\*\* the difference between the baryon and lepton numbers

Standard Model extensions have theorized the violation of  $B - L$ , resulting in the manifestation of a Goldstone Boson or Majoron, which could mediate neutrinoless double beta decay.  $0\nu\beta\beta$  mediated by a single Majoron can be expressed as,

$$(A, Z) \rightarrow (A, Z + 2) + 2e^- + \chi^0 \quad (2.39)$$

where  $\chi^0$  is the emitted Majoron. The decay rate for the interaction is given by,

$$\left( T_{1/2}^{0\nu\chi^0} \right)^{-1} = G^{0\nu\chi^0} (Q_{\beta\beta}, Z) \left| M^{0\nu\chi^0} \right|^2 \langle g_{\chi^0} \rangle^2 \quad (2.40)$$

where  $G^{0\nu\chi^0}$   $M^{0\nu\chi^0}$  are as previously defined, and the lepton number violating parameter in equation 2.35 is exchanged for  $\langle g_{\chi^0} \rangle$  which represents the coupling between the Majoron and the neutrino. The Feynman diagram of the decay is shown below,

The measured total electron energy of the decay can be used to infer the Majoron emitting decay mechanism, however with the addition of emitted particles other than the electron, the energy takes on a continuous spectra similar to that observed with  $2\nu\beta\beta$  \*\*\*ref plot with  $0/2\nu$  energy. The shape of the total electron energy spectra is dependent upon the Majoron model used during the decay, which can include up to two different Majorons as shown in figure ??

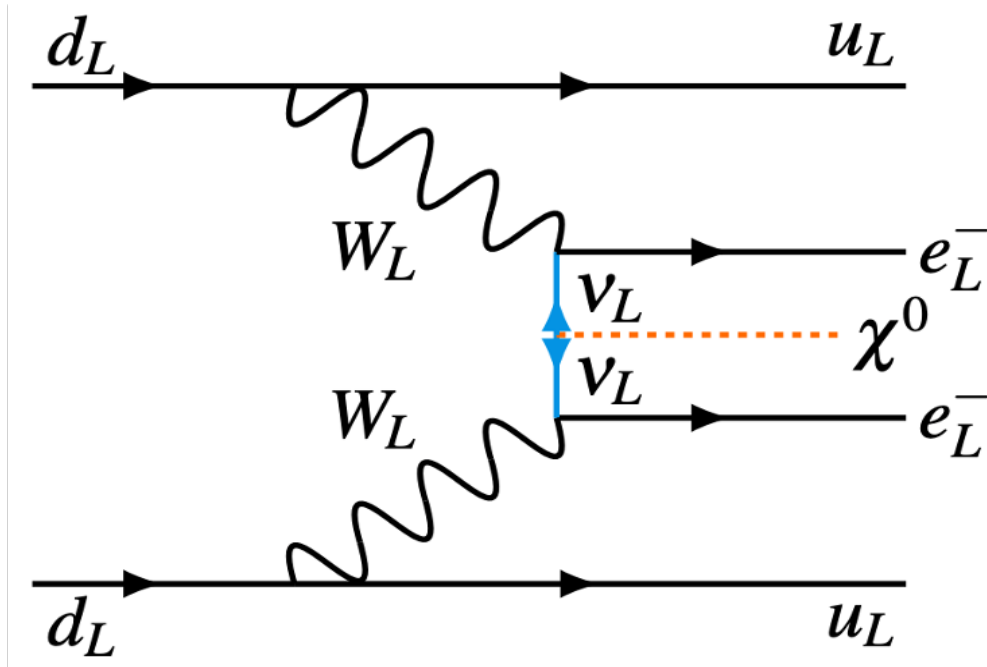


Figure 2.10: MajoronEmission [24]

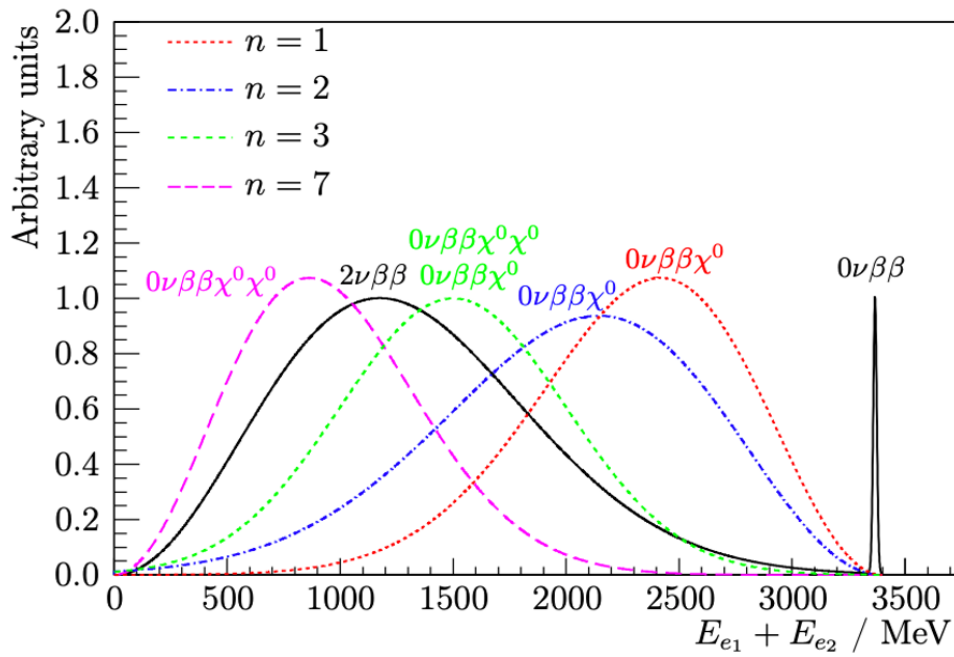


Figure 2.11: MajoronEnergies [25]

### 2.8.3 Right Handed Current

Currently, the weak interaction is only propagated by a left handed  $W$  boson, however by proposing a right handed component of the weak force, a right handed gauge boson, may mediate a neutrinoless double beta decay with only right handed neutrinos. The hypothesized right handed gauge boson may be related to the  $W$  or  $Z$  bosons as a mixture of multiple boson states or could manifest as an entirely novel gauge boson. A Feynman diagram of  $0\nu\beta\beta$  mediated by a right handed  $W$  boson and right handed neutrino is shown in figure 2.12 below,

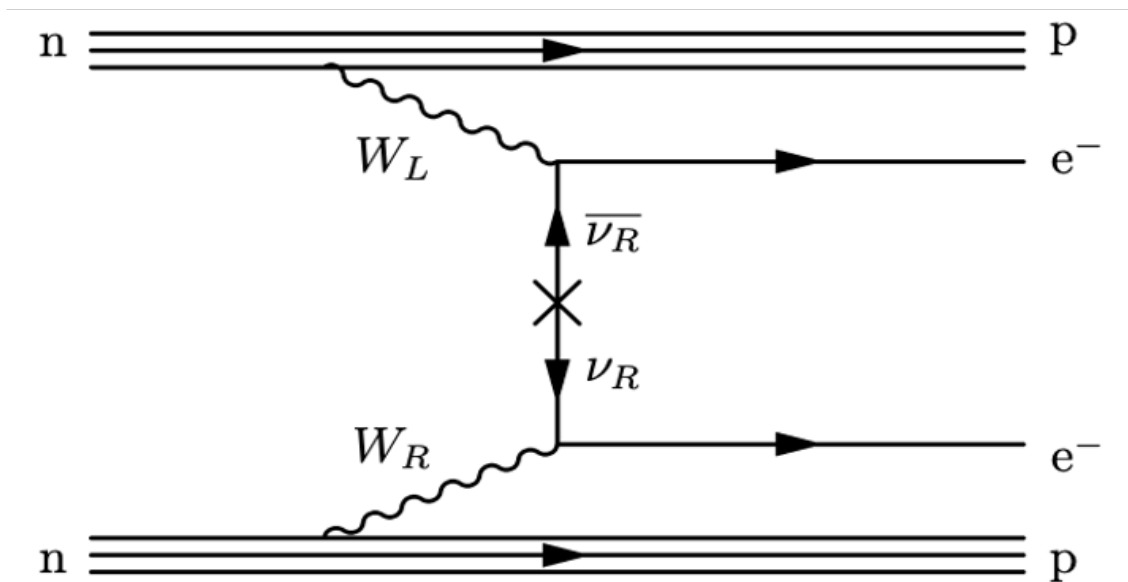


Figure 2.12:  $0\nu\text{RH}$  [23]

In figure 2.12,  $0\nu\beta\beta$  is mediated by a right handed  $W$  boson and right handed neutrino which is a Majorana particle. The alternative decay kinematics may be probed by investigating opening angle and energy distributions as shown in figure 2.13, which highlights the difference in the distributions with changing decay mechanisms. The

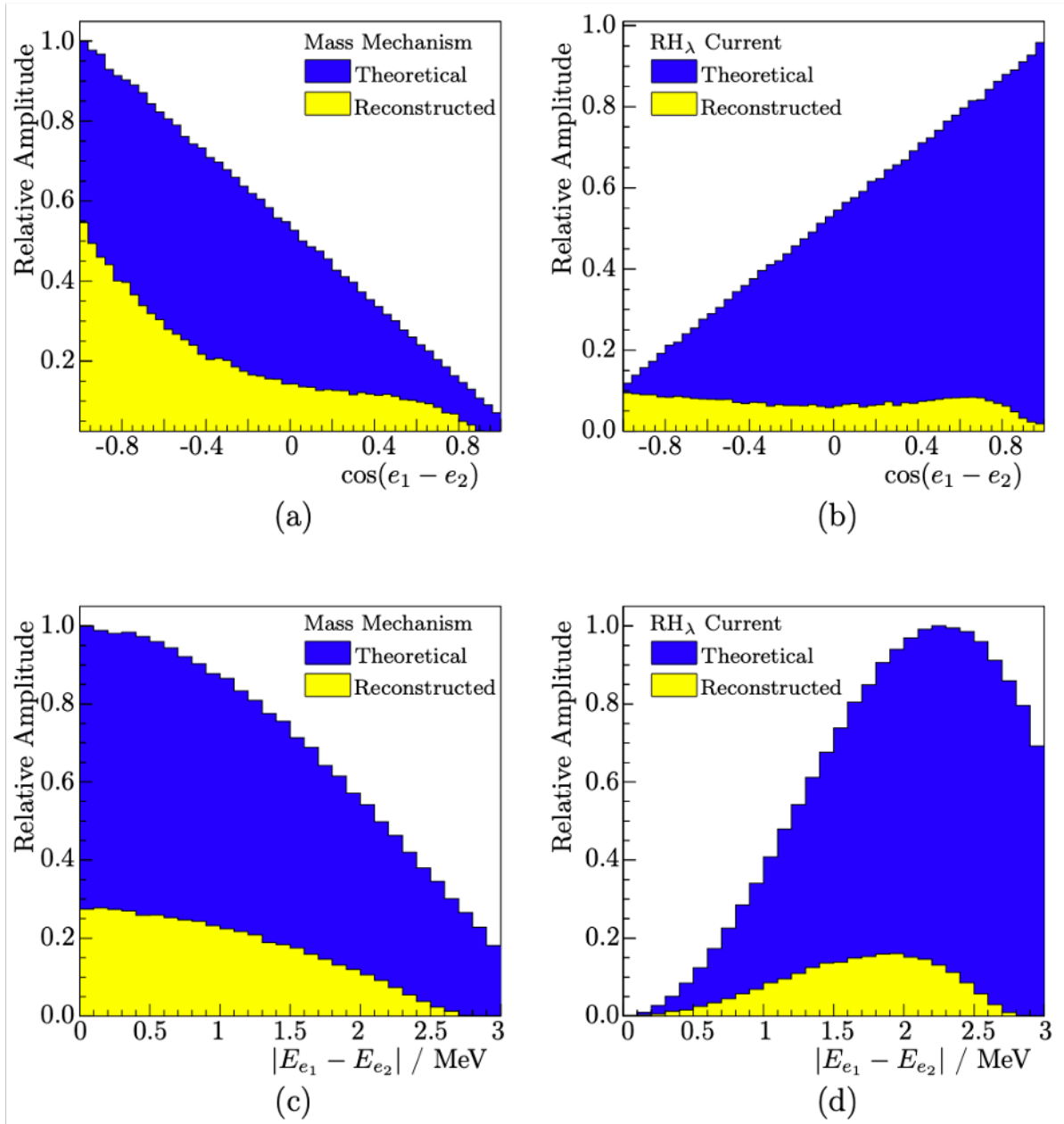


Figure 2.13: RHCURRENTS [26]

## 2.9 Open Questions on the Nature of Neutrinos

### 2.9.1 CP Violation

### 2.9.2 Single and Higher State Dominance

### 2.9.3 Nuclear Matrix Elements

Phenomenology

# Chapter 3

## The SuperNEMO Demonstrator

SuperNEMO is the successor to the NEMO-3 experiment which ran from 2003-2011 collecting data for following double beta decaying isotopes,  $^{100}\text{Mo}$ ,  $^{82}\text{Se}$ ,  $^{130}\text{Te}$ ,  $^{116}\text{Cd}$ ,  $^{150}\text{Nd}$ ,  $^{96}\text{Zr}$  and  $^{48}\text{Ca}$ . Unlike NEMO-3 however, SuperNEMO will focus solely on the isotope  $^{82}\text{Se}$ .

SuperNEMO is located in the underground laboratory, Laboratoire Souterrain de Modane (LSM), located within the Frejus road tunnel linking Modane to Bardonnecchia. The underground location helps to protect the detector from cosmic radiation and further protection comes in the form of iron and water shielding which reduces the impact of the natural radiation found in the surrounding rock.

NEMO-3 used a cylindrical design, divided into 20 equal sections of isotopic source material whereas SuperNEMO uses a modular structure, with the source located at the centre of the detector, surrounded by the tracker and calorimeters. The structure of the detector allows charged particle tracks and energies to be determined as they propagate through the volume of the tracker before finally coming to rest within the calorimeters.

During detector operation, it is expected for the detector to use a magnetic field, applied to the tracker volume to determine the charged of the particles passing through the detector. However, prior to activating the magnetic coil, the influence of different magnetic field configurations will be investigated in this thesis to determine the optimum magnetic field choice for the detectors operational lifetime.

SuperNEMO structure also allows scaling, exchanging isotopes that can be processed into foils  
\*\*\*

\*\*\*shielding\*\*\*

SuperNEMO utilises a

### 3.1 The SuperNEMO Demonstrator Design

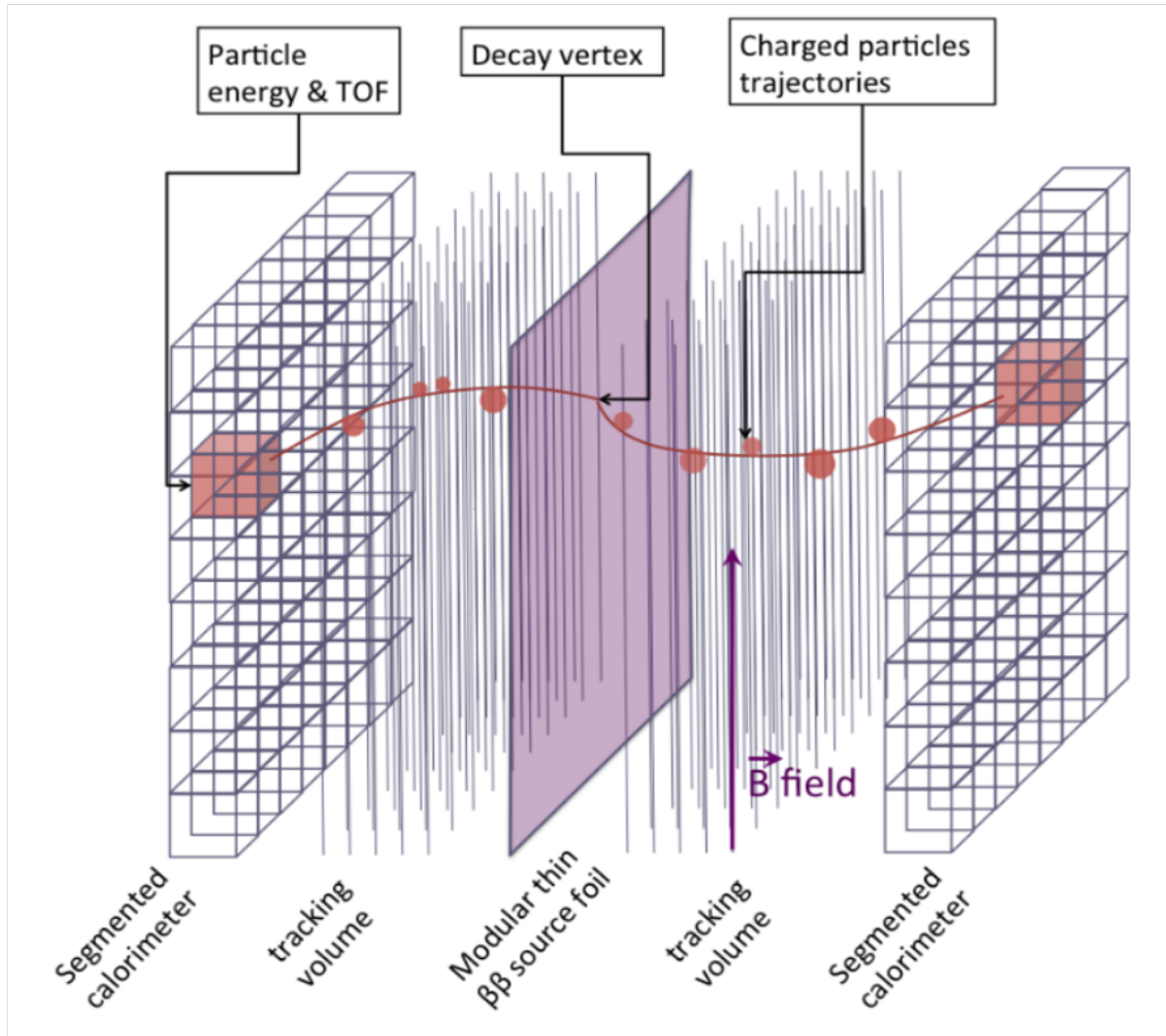


Figure 3.1: DemonsDetector

Unlike previous double beta decay experiments, SuperNEMO (and NEMO-3) uses a source-tracker-calorimeter structure allowing both the particle energy and the associated trajectory to be determined. The structure of the detector provides multiple advantages compared to other double beta decay experiments including,

- i Being able to identify and differentiate all natural radioactive particles, that is, the electron, positron, photon and alpha particle. Furthermore it is possible for SuperNEMO to identify muons that may cross the detector
- ii Identifying multiple particles allows for a variety of decay channels to be investigated, primarily



the two electron channel for double beta decay as well as the  $1e1\alpha$  channel for BiPo measurements or other background decay channels.

- iii State dominance of the  $^{82}\text{Se}$  decay and whether the decay is dominated by a single intermediate state or many higher energy intermediate states
- iv Can be easily scaled to increase the exposure of  $^{82}\text{Se}$  or perhaps investigate other double beta decaying isotopes

However there are also a number of disadvantages as a result of the detector design including,

- i Low source mass, limited by the thickness of the source foil. If the source foil is too thick it will inhibit the emission of electrons from inside the foil reducing the detection efficiency.
- ii Lower detection efficiency and energy resolution compared to germanium and bolometer experiments.

### 3.1.1 Detector Structure

As mentioned, the SuperNEMO detector uses a modular source-tracker-calorimeter with the use of a passive source, that is, a source that is not part of detection unlike the proposed for the germanium experiment LEGEND <sup>\*\*\*ref\*\*</sup>.

The source foil is located at the centre of the detector, surrounded by the tracker volume and finally the calorimeters. The source foil is a thin, mechanically processed foil, that is enriched in  $^{82}\text{Se}$ . The narrowness of the foil allows for improved emission of charged particles from the source foil and into the tracker chamber. In total the source foil mass was measured to be approximately 6.23Kg of enriched  $^{82}\text{Se}$ , whilst being approximately 2.7m in length.

$^{82}\text{Se}$  was selected as the isotope of choice for the SuperNEMO demonstrator, amongst the isotopes used in the NEMO-3 detector because of its relatively high decay energy, reasonable  $2\nu\beta\beta$  half-life, high natural abundance, ease of enrichment and reasonable phase space factor. The properties of the isotopes used in NEMO-3 are shown below

The low decay energy removes a large amount of the low energy backgrounds whilst the remaining factors ensure the availability of  $^{82}\text{Se}$  with a frequent amount of decays.

<sup>\*\*\*cu foil, used for external bg, 34 foils in total, covered in mylar \*\*\*</sup>

To track the trajectories of the charged particles propagating from the source foil, each side of the surrounding tracker chamber comprises of 113 columns of nine drift cells, totalling 2034 cells for both sides of the tracker. Each drift cell contains a central anode wire which is run at a high voltage, surrounded by eight grounded field shaping wires and two ring shaped cathodes at on either end of the cell.

tracker chamber surrounding the source foil <sup>\*\*\*</sup> planar to source foil unlike rounded nemo 3

Isotope	$Q_{\beta\beta}$ (MeV)	$G_{0\nu}$ ( $10^{-15}y^{-1}$ )	$T_{1/2}^{2\nu}$ (y)	$\eta$ (%)
$^{48}\text{Ca}$	4.273	24.81	$6.37^{+0.56}_{-0.69} {}^{+1.21}_{-0.89} 10^{19}$ (NEMO-3)	0.187
$^{76}\text{Ge}$	2.039	2.363	$1.926 \pm 0.094 10^{21}$ (GERDA)	7.8
$^{82}\text{Se}$	2.995	10.16	$9.6 \pm 0.3 \pm 1.0 10^{19}$ (NEMO-3)	9.2
$^{96}\text{Zr}$	3.350	20.58	$2.35 \pm 0.14 \pm 0.16 10^{19}$ (NEMO-3)	2.8
$^{100}\text{Mo}$	3.035	15.92	$6.93 \pm 0.04 10^{18}$ (NEMO-3)	9.6
$^{116}\text{Cd}$	2.809	16.70	$2.8 \pm 0.1 \pm 0.3 10^{19}$ (NEMO-3)	7.6
$^{130}\text{Te}$	2.530	14.22	$6.9 \pm 0.9 10^{20}$ (NEMO-3)	34.5
$^{136}\text{Xe}$	2.458	14.58	$2.165 \pm 0.016 \pm 0.059 10^{21}$ (EXO-200)	8.9
$^{150}\text{Nd}$	3.367	63.03	$9.11^{+0.25}_{-0.22} \pm 0.63 10^{18}$ (NEMO-3)	5.6

Figure 3.2: Isotope Properties

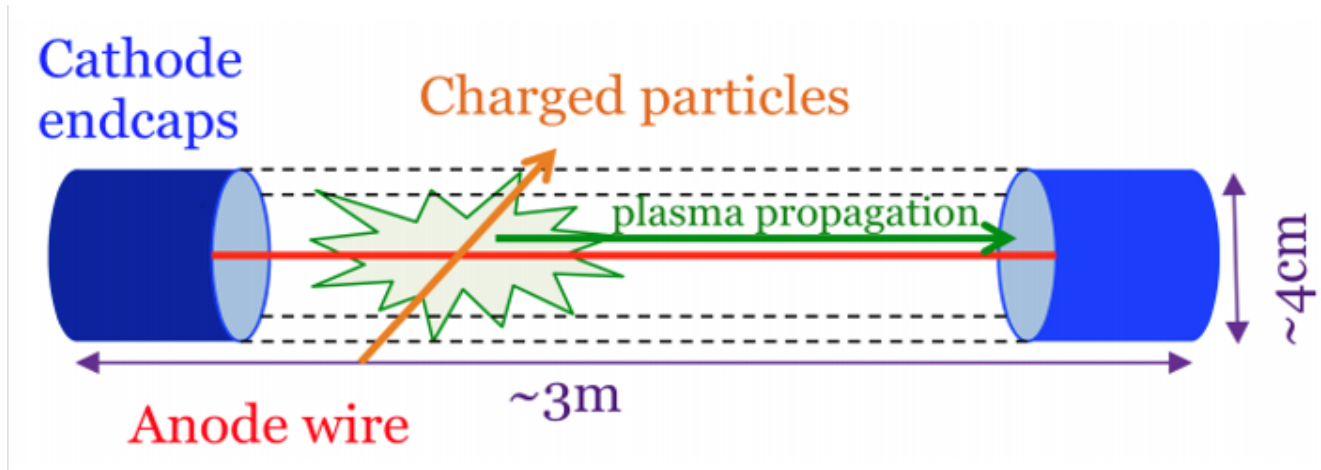


Figure 3.3: TrackerCells

The tracker is filled with gas, a mixture of He (95%), ethyl alcohol (4%) and Ar (1%). As charged particles enter the tracker chamber they ionize the gas and the time taken for the ionized electron shower to drift towards the anode infers the distance of the charged particle from the centre of the cell. Tracker cells are run in Geiger mode, so that \*\*\*\*Geiger definition \*\*\*

Additionally, the two cathode end caps measure how far along the the tracker cell the charged particle was when generating the electronic shower. The combination of these two mechanisms allows the trajectory of the particle to be determined in three dimensions.

The final component of the SuperNEMO demonstrator module structure is the calorimeter wall, which surrounds the tracker. Calorimeters or optical modules (OMs) measure the energy of the charged particles that are emitted from the source foil and come to rest within the calorimeters. Each calorimeter consists of a plastic scintillator as well as a photomultiplier tube (PMT).

The plastic scintillator is made of POPOP (1,4-di-(5-phenyl-2-oxazolyl)benzene) doped polystyrene,

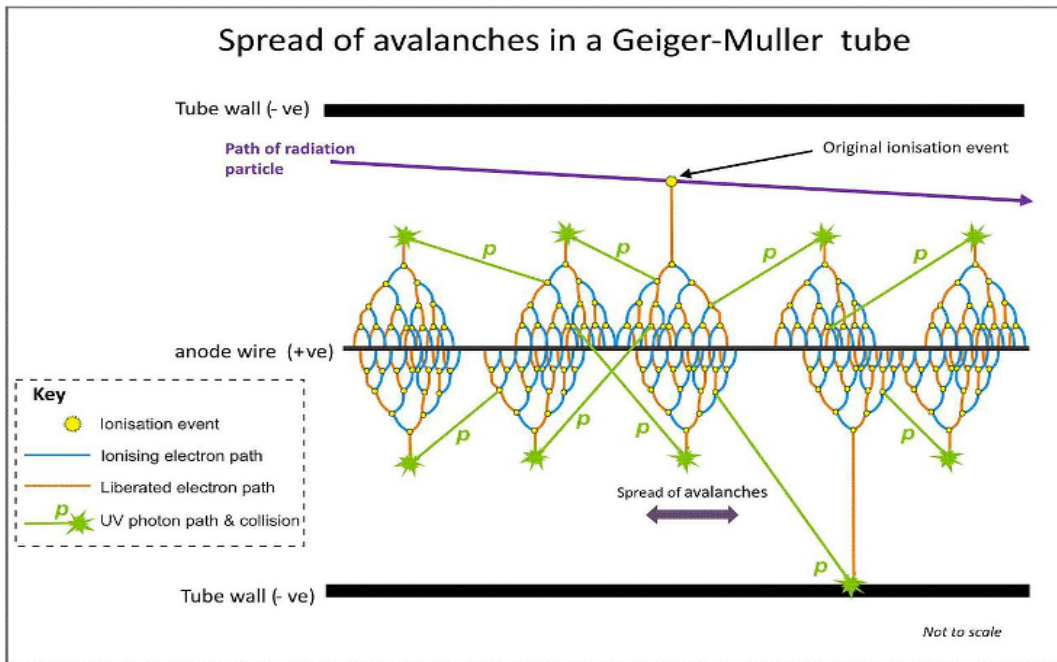
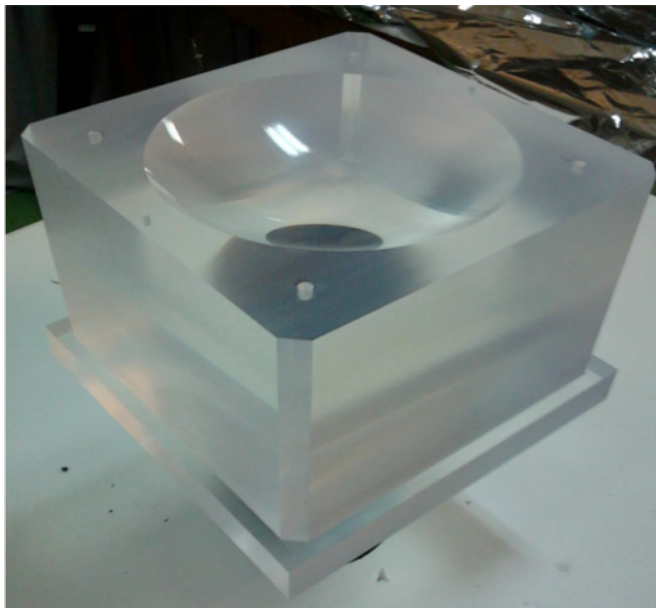


Figure 3.4: GeigerMechanismtrum



(a) ScintCurve



(b) OM

which acts as a wavelength shifter and PTP (para-terphenyl) which increases the light yield during ionization. When an incident particle strikes the plastic scintillator block, it loses energy from multiple scatterings, resulting in a number of photons being emitted proportional to the incident

particle energy. Scintillator blocks are wrapped in both aluminised mylar to increase light collection and protect against UV radiation from the tracker or adjacent OMs and teflon to increase photon collection efficiency.

8.3% energy res FWHM at 1 MeV

Hamamatsu PMTs were recycled from NEMO-3 for use in SuperNEMO and come in two sizes, 8" and 5". The 8" calorimeters provide improved energy resolution and thus mostly confined to the parts of the calorimeter wall with the greatest particle flux. By carving the plastic scintillators, the PMT bulbs can be coupled to them using radiopure glue.

There are a total of six calorimeter walls for SuperNEMO, two of each of the following; Main wall, X wall and the Gamma Veto or Veto wall. Each wall is comprised of a different number of calorimeters with the corresponding PMT size,

- i Main wall: 220 8" calorimeters and 40 5" calorimeters.
- ii X wall: 64 5" calorimeters.
- iii Veto wall: 32 5" calorimeters.

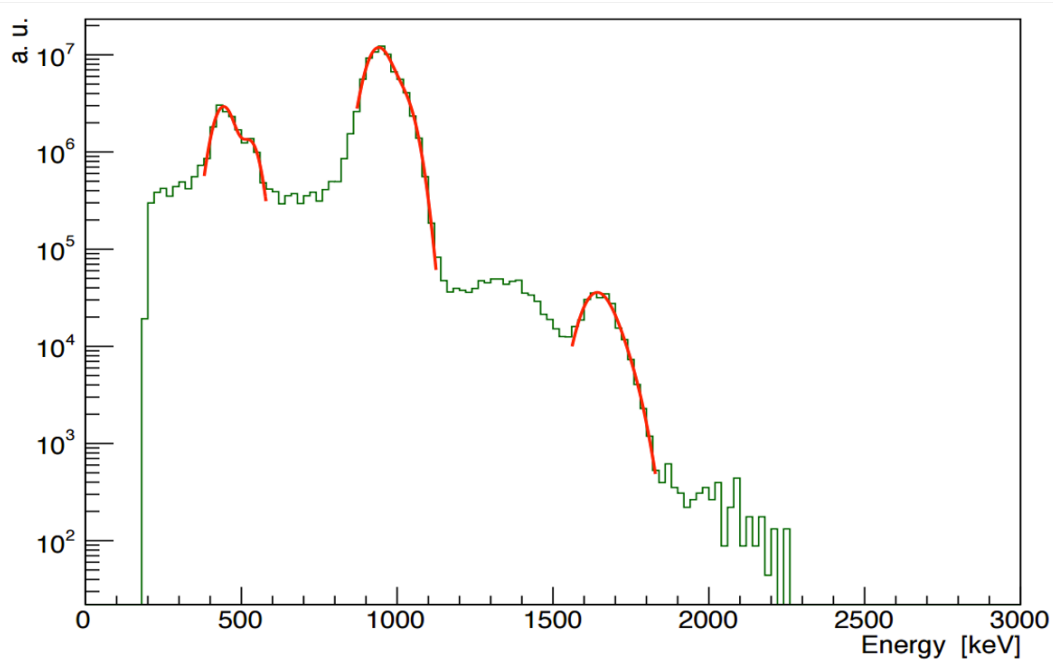
so the total number is doubled for each type of wall.

Unlike NEMO-3 calorimeters, light guides are also used with the calorimeters to further increase the collection efficiency of incident photons. Importantly, the presence of the light guides significantly alters the applied magnetic field inside of the tracker chamber, resulting in a significant non-uniformity of the field. The impact of this will be discussed later\*\*\*.

### 3.1.2 Commissioning Progress

Multiple calibration methods will be used to determine the energy and time responses of the detector to known sources. To perform energy calibration for SuperNEMO,  $^{207}\text{Bi}$  will be deployed within the detector to obtain an absolute energy measurement.  $^{207}\text{Bi}$  undergoes a number of internal conversions, resulting in the emission of electron calibration lines with energies of at 482, 976 and 1682 keV.

For each source, a droplet of  $^{207}\text{Bi}$  in between two layers of mylar will be encapsulated by a radiopure copper frame, following which they will be inserted into the gaps between the source foils via an automatic source deployment system. Calibration is expected to be performed regularly during detector operation to ensure energy measurements are accurate. The  $^{207}\text{Bi}$  internal conversions will be reconstructed from the location of the copper frames to the calorimeters to determine the measure energies compared to the true  $^{207}\text{Bi}$  internal conversion lines. For the purposes of investigating the sensitivity of the experiment to neutrinoless double beta decay in the  $^{82}\text{Se}$  region of interest (2.8-3.2 MeV) the greatest internal conversion energy of 1682 keV will provide the best degree of calibration at those energies.

Figure 3.6:  $^{207}\text{Bi}$  Spectrum

Alongside the  $^{207}\text{Bi}$  deployment close to the source foil, a light injection system (LIS) will also be deployed to perform both time calibration and measure gain for the optical modules. The light injection system uses pulses of ultraviolet light from light emitting diodes, through optical fibres to illuminate OMs and measure their gain. The length of all fibres will be maintained at 20m to avoid any systematic time differences.  $^{241}\text{Am}$  is used as a source with a reference OM to monitor and maintain the light level. In total, the LIS will allow any variations in gain from voltage fluctuations be tracked and corrected with a precision of 1% alongside the time calibration.

Additional time calibration will be performed using  $^{60}\text{Co}$ , which produces two photons, the first being of energy 1.17 MeV and the second, 1.33 MeV. The two photons are emitted almost simultaneously ( $\Delta t = 0.41\text{ps}$ ) from the source at a separation much lower than the time resolution of the PMTs. However, by placing the  $^{60}\text{Co}$  source behind the main wall in one of nine different positions, at known distances from two PMTs, the energies and time separation of the two photons can be measured to determine the offset of the PMTs.

Current status \*\*\*

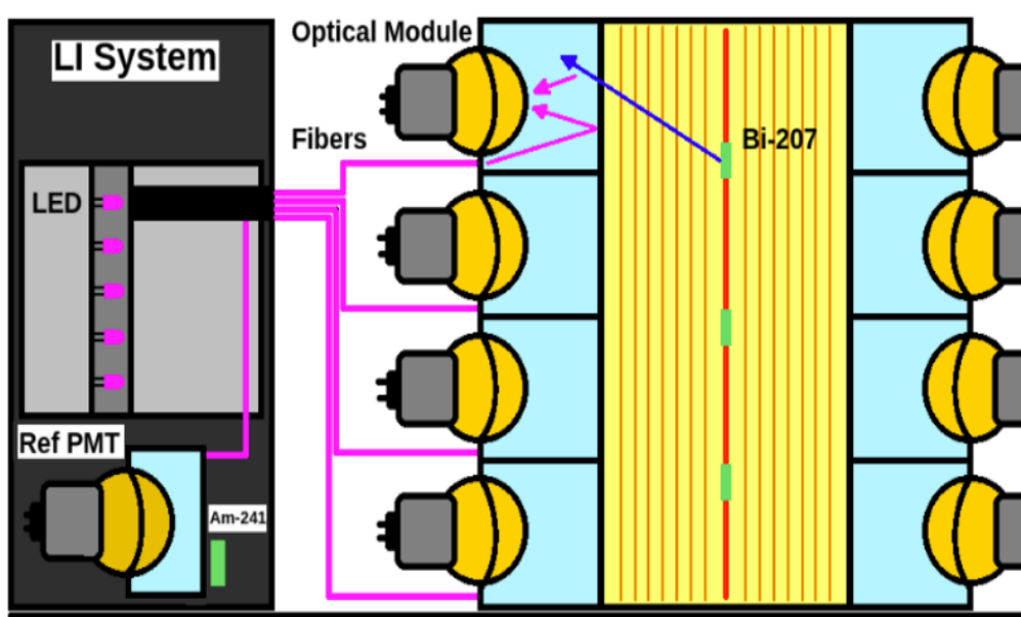


Figure 3.7: LIS

### 3.1.3 Detector Calibration

### 3.1.4 Expected Sensitivity

## 3.2 Backgrounds Sources

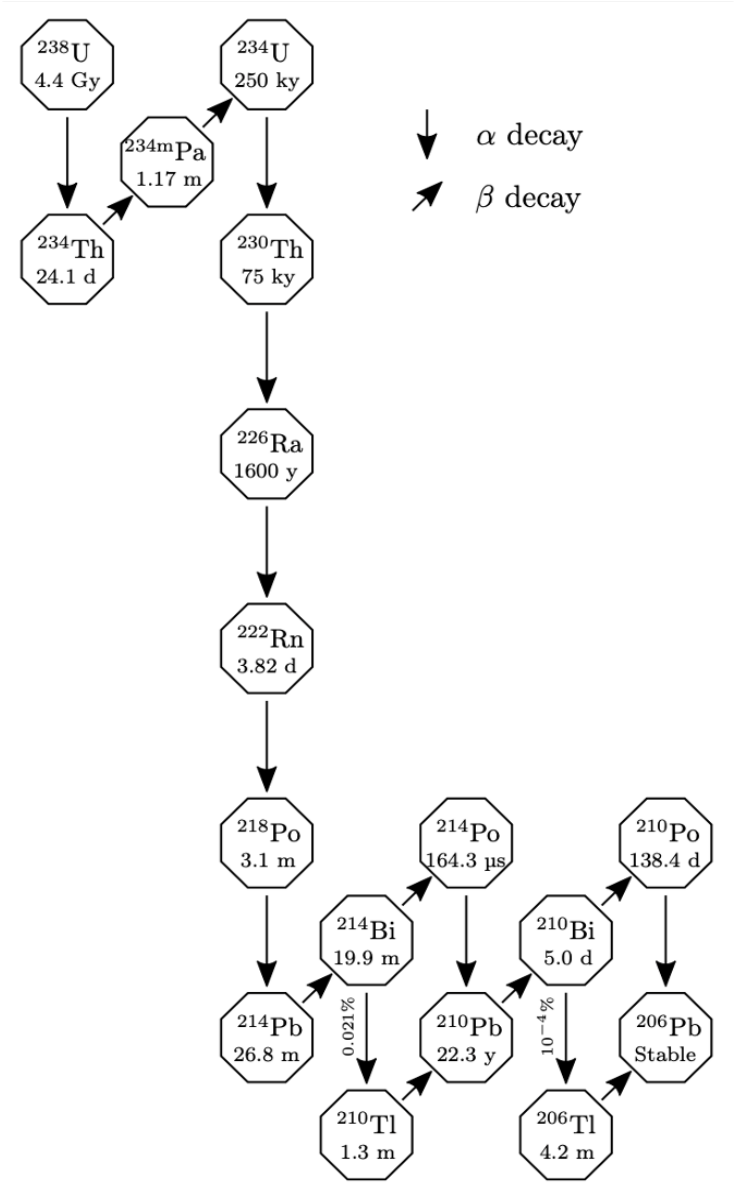


Figure 3.8: Bi214DecayScheme

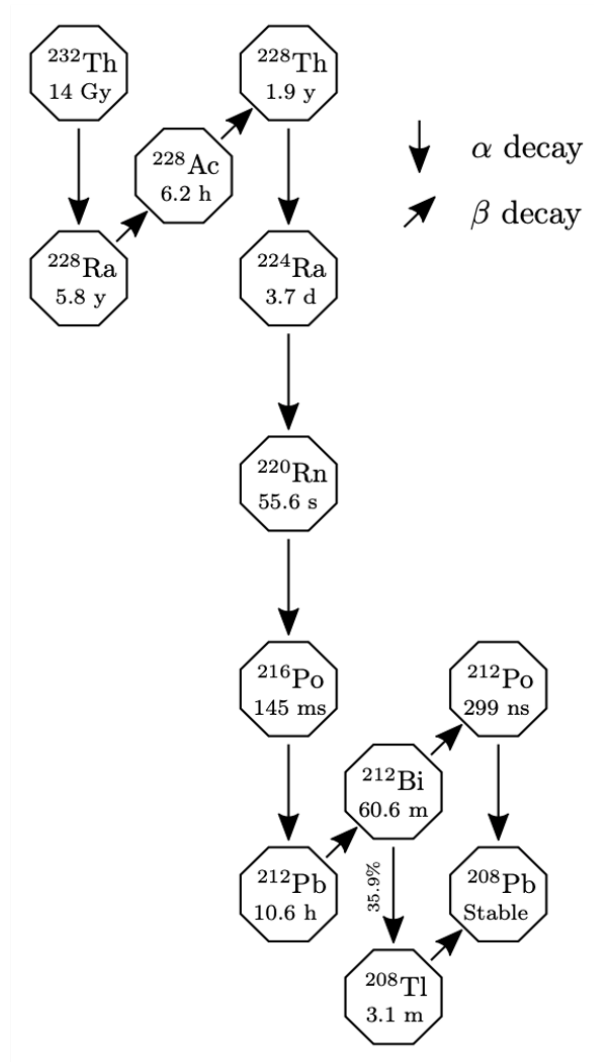


Figure 3.9: Tl208DecayScheme

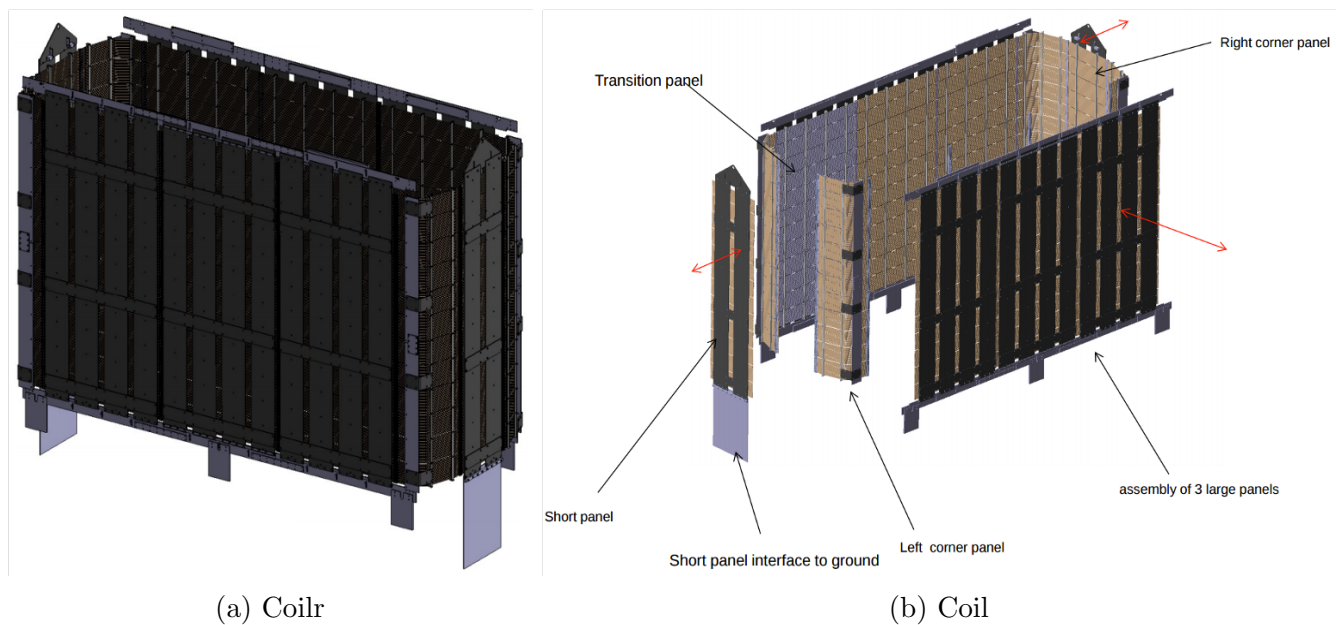


### 3.2.1 Other DBD Experiments

\*\*\*

### 3.2.2 Magnetic Coil and Shielding

The magnetic field for the SuperNEMO detector will be generated by a copper magnetic coil, recycled from old NEMO-3 copper rods. The coil will be built to surround the detector ensuring the magnetic flux is contained within the tracker volume.



The presence of magnetic field inside the glass of a PMT significantly reduces the performance of the PMT even at very low field strengths, figure 3.11

Unlike NEMO-3, SuperNEMO does not use a light guide with the OMs as the PMTs are directly coupled to the plastic scintillators as shown in figure \*\*\*\*ref \*\*\*. As a result, the PMTs are exposed to the tracker volume and the potential magnetic flux. To prevent the PMT performance being reduced by the magnetic field, iron shields will be used to protect the PMTs and remove any magnetic field from within their volume.

Furthermore, it is expected that the coil will be used to generate a magnetic field of approximately 25 Gauss. However it is possible for the strength of the magnetic field to be adjusted by altering the current inside of the coil. The purpose of the magnetic field applied to the tracker volume is to help determine the charge of any particle propagating through the tracker by measuring the magnetic field induced curvature of the particle. Electrons from  $^{82}\text{Se}$  double beta decay are of relatively low energy and so do not require high magnetic field strengths to curve them, however it

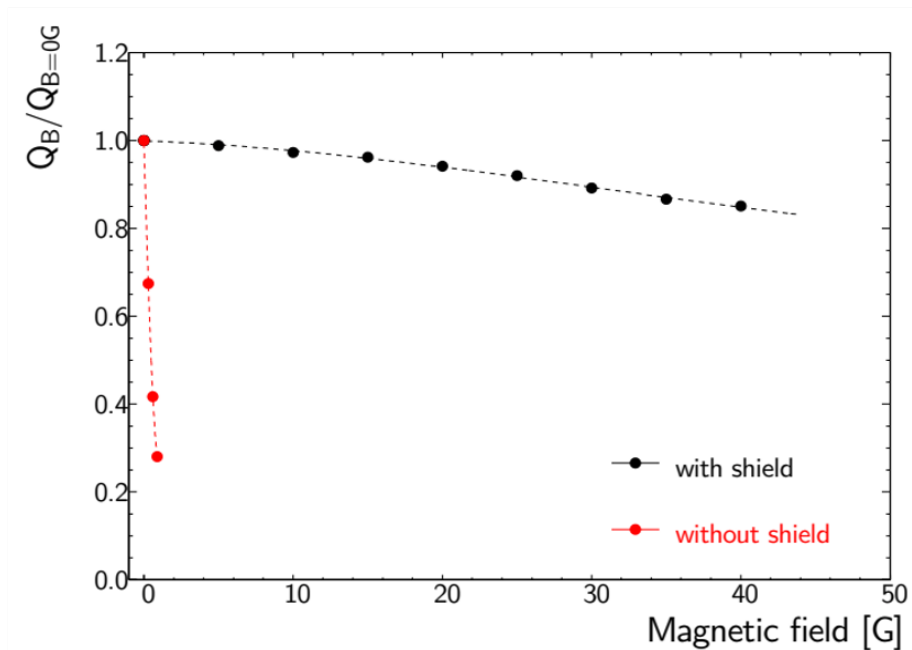


Figure 3.11: A

may be pertinent to use a different field strength if it results in an increase in the detection efficiency of  $0\nu\beta\beta$ .

### 3.3 Motivation for Magnetic Field Studies

The magnetic field allows electrons and positrons to be differentiated by the directionality of their associated track curvatures. It provides a useful tool for removing significant backgrounds, in particular photons with energy greater or equal to 1.02 MeV, which are capable of pair producing an electron positron pair. Other sources of positrons include rare positron emitting decays however they are seldom observed and not expected to be problematic.

\*\*\*pair produce/ show electron curvature \*\*\*

Photon flux inside the detector is extremely high as illustrated by table \*\*\* table of photon flux for different sources\*\*\* so positron identification is a priority. However it may be possible to use the detector without a magnetic field. Removing or reducing the strength of the magnetic field may increase the number of expected background events, however it may also increase the signal reconstruction efficiency, resulting in a net gain in sensitivity. By reducing the positron generating backgrounds by other means, it may be possible to increase the signal efficiency without significantly increasing the background that comes with having a reduced or no field.

Initially, three magnetic field configurations were selected, including the uniform field, no field and the realistic field. The uniform field is defined as having a nominal 25 Gauss field, with uniform strength and shape throughout every part of the detector. No field is characterised by having no magnetic field (0 Gauss) throughout the detector and corresponds to having the magnetic field turned off. The realistic field is a mathematically computed field, representing the shape and strength of the field we expect to see during operation with a nominal 25 Gauss applied via a magnetic coil.

By comparing the detection efficiency of the three magnetic field configurations, a decision can be made as to when or if activating the magnetic field will increase our sensitivity to  $^{82}\text{Se}$  neutrinoless double beta decay. Maximising our sensitivity increases the probability of observing the decay, whilst simultaneously improving the precision of nuclear matrix elements and setting better limits on the decay itself.

### 3.3.1 The Realistic Field

Unlike NEMO-3, magnetic shields are required for the SuperNEMO demonstrator module as a consequence of the detector geometry exposing the PMTs to magnetic flux. The removal of a light-guide coupled to the surface of the PMTs exposes the vacuum tube of the PMT to the magnetic field inside the tracker volume. As shown in figure \*\*\* the presence of a magnetic field is extremely detrimental to the performance of a PMT and so the shielding should ensure that all magnetic flux is removed from the volume of the PMTs.

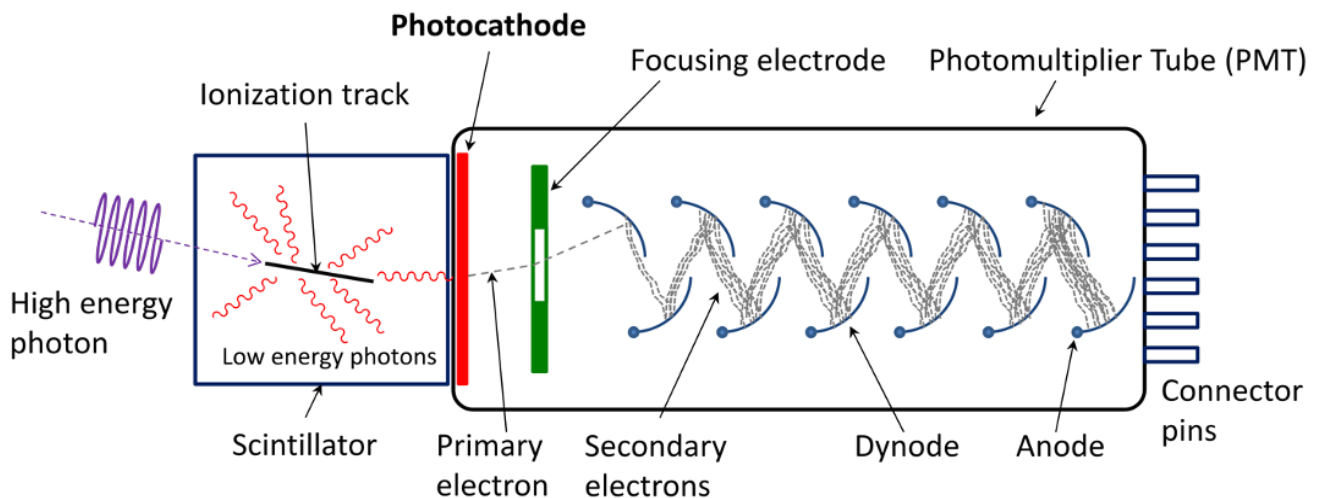


Figure 3.12: A

\*\*\*from wiki

The working mechanism of a PMT involves incoming photons generating photoelectrons that are focused onto the the first dynode. Secondary electron emission from the dynodes carries a charge which is collected by the anode. The collected current provides an output signal to indicate a hit to the calorimeter.

With the addition of a magnetic field, the low energy photoelectron trajectories are altered, reducing the collection efficiency of the dynodes. Even at a field strength of 1 Gauss the reduction in collection efficiency results in a complete loss of signal. Furthermore, there is the possibility of PMT components, in particular, the dynode substrate and the electrode, being permanently magnetised following exposure to weak magnetic fields for long periods of time. The residual magnetization can result in a change to the gain of a PMT, ultimately reducing performance. Over the length of time taken for detector operation any changes in the gain of PMTs should be monitored to ensure the precision of energy measurements are maintained.

As a result of using the magnetic shields however, the shape and strength of the field is altered so that is it no longer uniform in shape or strength. As mentioned earlier, the expected magnetic field is labelled the realistic field and represents the magnetic field altered by the magnetic shielding to protect the PMTs against the magnetic flux in the tracker. The shape and strength of the realistic field is shown in the image below

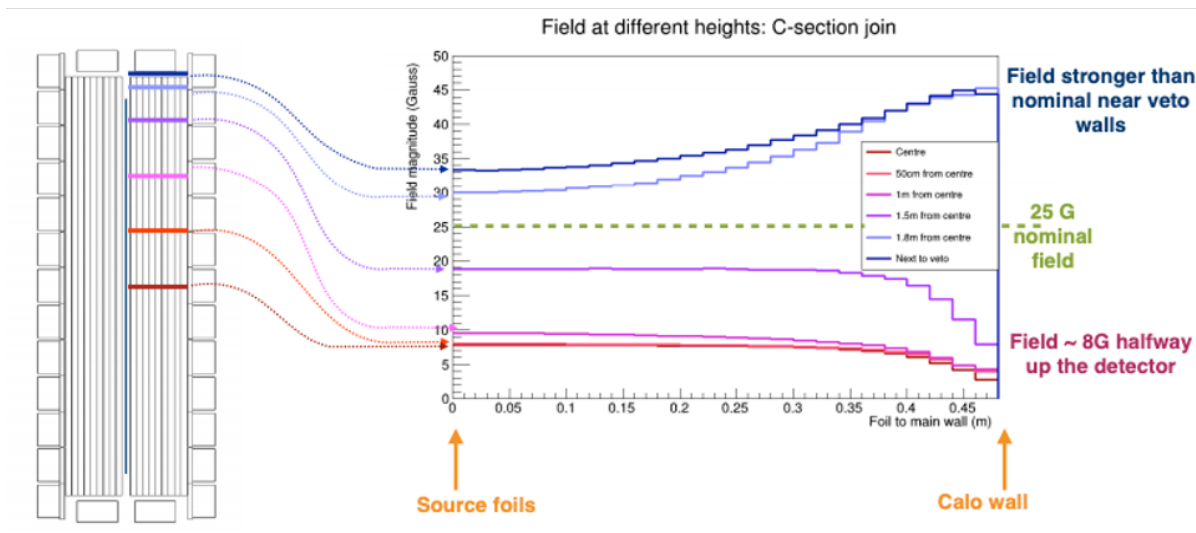


Figure 3.13: A

The main aim of the magnetic field analysis described in this thesis is to compare the performance of the three field configurations to determine which of the three fields is most advantageous for use during and throughout the detectors operational lifetime. Although the uniform field does not correctly depict the non-uniformity of the magnetic field during operation, it provides a nominal representation to compare to the other magnetic fields. Furthermore, by scaling the magnetic field applied by the coil, it is possible to increase the field strength of the realistic field so that it more

closely resembles the uniform field and a more direct comparison can be made.

\*\*\*\*as shown by scaled field\*\*\*\*

No field examines the performance of the detector without an applied magnetic field. If no field displays an increased performance over the realistic and uniform fields it may be advantageous to run the detector without a magnetic field and to remove pair produced backgrounds through other avenues. Additionally, there is the option to run the detector without the magnetic field for a short period of time and to determine at what point, if at all, to turn on the magnetic field during experimentation. Once the magnetic field is turned on, it is impossible to reverse the effects of the applied field on the detector components even if the field is later turned off and so it is important to identify what approach to take and if or when the magnetic field should be applied, as applying the field is irreversible.

\*\*\*maybe more detail on shields, relative permeability, vs field inside field \*\*\* maybe include pic of own magnetic field in 3D

### 3.3.2 Magnetic Shield Testing

Prior to installation, individual magnetic shields were tested to ascertain whether they were still able to significantly reduce magnetic flux from within the volume inside. To measure the efficiency at which the shields remove magnetic flux from within their own volume, the magnetic field with and without shielding was measured. A copper solenoid was connected to a controlled current source to generate a magnetic field. The solenoid was coiled around an impermeable container to retain the field inside of the container. A magnetometer was used to measure the field strength within the container. The field was calibrated to 25G following each measurement and the magnetometer measured the field strength, with and without shielding to determine the influence of the shield on the magnetic field inside of it.

Over 250 shields were tested, both for 8" and 5" PMTs, with the majority expelling over 95% ( $B < 1.25G$ ) of the magnetic field within the shielded volume. Once tested the shields were packed and shipped to the LSM to be installed as part of the detector.



Figure 3.14: A

# Chapter 4

## Analysis Techniques

### 4.1 Falaise

Falaise provides the overarching software environment and is used as the primary tool for the simulation, processing and analysis of data for the SuperNEMO collaboration. Falaise uses the DECAY0 event generator in combination with GEANT4 and the C++ Bayeux library to generate and propagate particles throughout the depiction of the detector geometry.

Falaise is comprised of four principal components:

- Flsimulate  
The primary tool for simulating data
- Flreconstruct  
Pipeline structure used to process the output from flsimulate and produce reconstructed data
- Flvisualize  
Event viewer for the visualization of the detector geometry, simulated and reconstructed data
- LibFalaise  
The core libraries

Data production follows the route displayed in figure 4.1. Firstly, events are simulated, after which the simulated data is processed via a reconstruction pipeline to generate reconstructed data. Reconstructed data incorporates detector effects such as noise and energy resolution into the simulated data, producing data in the same format as the detector electronics.

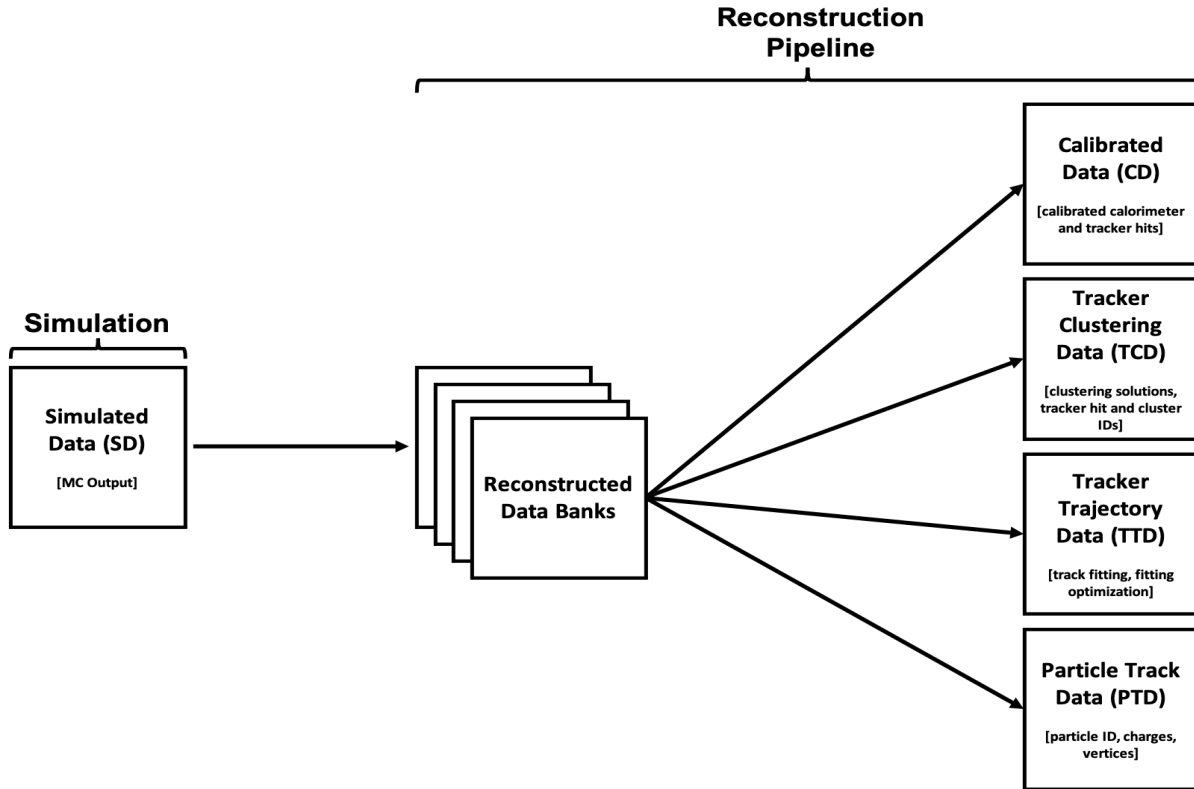


Figure 4.1: Visualization of the Falaise pipeline structure, beginning with simulation and ending with the stored data banks for reconstructed data.

#### 4.1.1 Simulation

Fsimulate is the main simulation tool for SuperNEMO. Fsimulate is a command line program which accepts a configuration file that provides instructions for simulating events. The configuration file allows the user to determine multiple criterion for simulation, including;

- The initial decay particle
- The availability of raw data for secondary particles. Secondary particles are generated as a result of primary particle interactions with the detector (as described by GEANT4).
- Location of the decay vertex
- Number of simulations
- Magnetic field configuration

The DECAY0 event generator [27] is responsible for generating the initial radioactive decay particle with appropriate energies, timing, kinematics and branching ratios. Propagation of decay

particles through the detector is determined by the object-oriented toolkit GEANT4 [28], which simulates the interactions of decay particles with the detector geometry and materials. GEANT4 also manages detector hits, tracks and visualisation for each simulated event. Flsimulate provides a default output file type of Boost over Root I/O (.brio) as suitable input for both reconstruction (flreconstruct) and visualization (flvisualize).

### 4.1.2 Reconstruction

The simulated output is processed with flreconstruct, using a customizable reconstruction pipeline, which runs through the raw data. Modules can be sequentially selected to generate and fill multiple data banks with reconstructed data. The reconstruction pipeline highlighted in figure 4.1 illustrates the data banks and the types of data they include. Calibrated Data (CD) includes data with the addition of detector noise and resolution effects. Tracker Clustering Data (TCD), using pattern recognition software, stores reconstructed tracker hits and clusters. Track fitting and  $\chi^2$  optimization of the clusters is stored in the Tracker Trajectory Data (TTD) and finally particle identification is accomplished, using the CD and TTD banks as inputs in order to identify the particle charges and vertices, storing the data in the Particle Track Data (PTD) bank. Combined, the different data banks provide all the reconstructed data for simulated decays, which provides an accurate depiction of the real data that is processed during detector operation.

An additional factor for reconstruction is the fitting type used by the TrackFit pipeline module. Charged particles can either be fitted with a straight track or a helical track, determined by the  $\chi^2$  of the proposed track. The track with the lowest  $\chi^2$  is selected from amongst the calculated tracks and is fitted to the simulated track. For no field simulations we expect the charged particle tracks to be straight and optimised to straight line fitting, however, for technical reasons, all three magnetic fields had both line and helical fitting active, which were fitted to the tracks solely based on the  $\chi^2$  value of the fitted track. Information regarding the curvature of charged particle tracks with no field was consequently discarded. Gammas are reconstructed using the gamma tracking module and are important for distinguishing the different background channels, such as  $e\gamma$  or  $e2\gamma$ .

### 4.1.3 Visualization

Event display visualization of both raw and reconstructed data is possible using the GUI display, flvisualize. Flvisualize provides an interface for both 2D and expansive 3D visual projections of the detector. Visualised data is shown within the framework of the detector to allow for visual analysis of simulations. The left hand panel of flvisualize provides a 2D display of either the top, side or front of the detector. The second panel displays a 3D projection of the detector including all three spatial dimensions. Flvisualize also provides multiple panels, including a 'Tracks' panel, which displays reconstructed data structures with selective visuals, allowing the user to determine which



visuals they wish to display. The remaining panels, 'Options' and 'Selections', provide additional functions however they are unimportant.

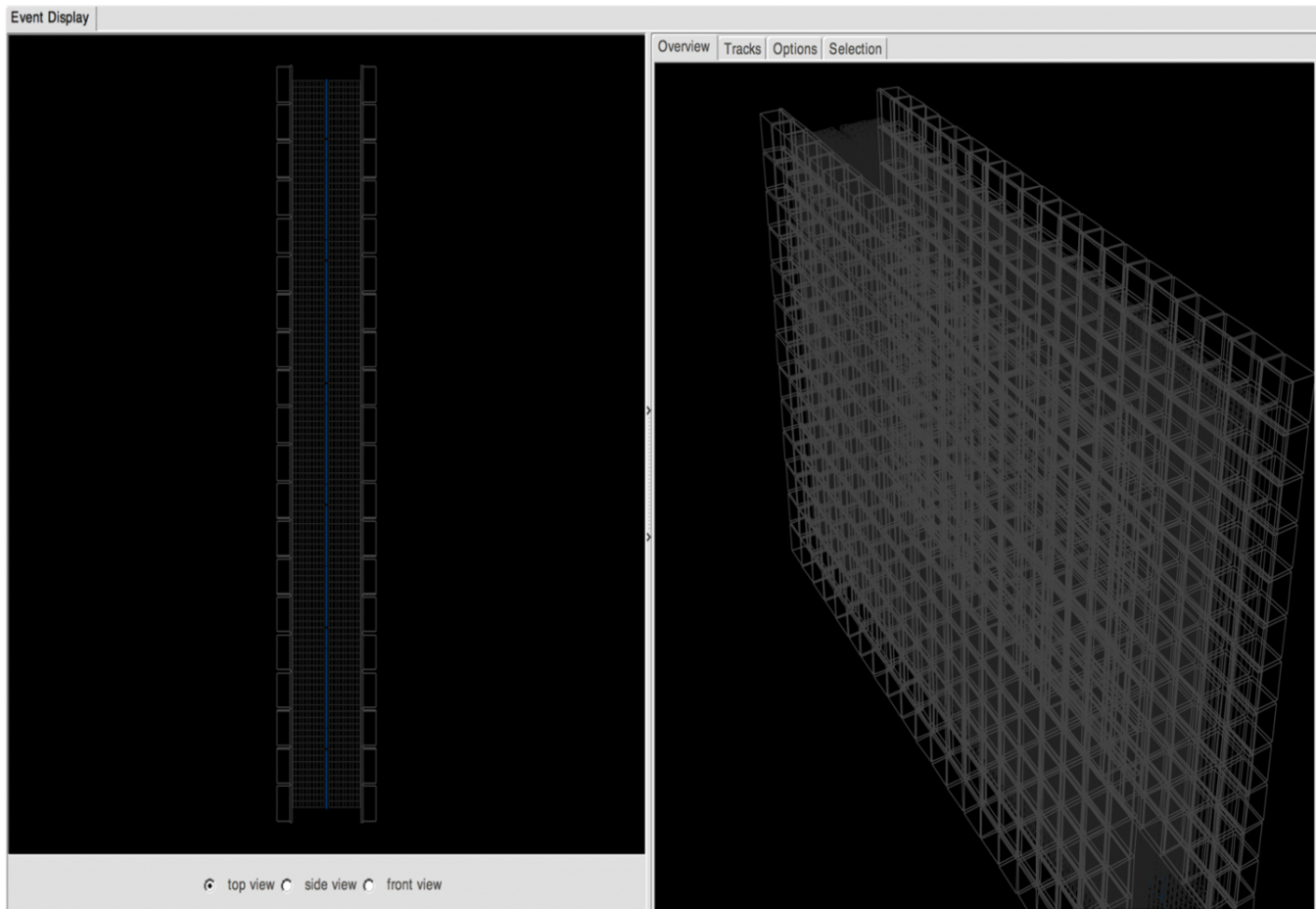


Figure 4.2: User interface of the Flvisualize tool used for visually displaying simulated and reconstructed events. The left hand side displays a 2D top view of the detector whereas the right hand side displays a 3D projection of the detector parallel to the foil.

#### 4.1.4 Secondary Particle Information

Secondary particle information provides increased true/GEANT level information, including additional insight into the properties of simulated particles, both primary and secondary. Secondary particle information provides the following:

- i Particle designation (electron/positron/photon) for all true simulated particle tracks
- ii Particle classification (primary or secondary) contingent on if the particle originated from the initial decay (primary) or from any other source (secondary)

- iii Number of true GEANT level hits for each particle track
- iv Simulated true track visuals in flvisualize

Additional simulations, with access to secondary particle information, were simulated in order to shed more light on the underlying mechanism behind the considerable number of double beta candidate events from external  $^{208}\text{Tl}$ . Understanding the underlying mechanism allowed for the background to be explicitly targeted and removed, in order to reduce the total background contamination, as will be discussed in chapter 7.

#### 4.1.5 Sensitivity Module

Sensitivity Module is a Falaise pipeline module which converts stored data from the Falaise data banks into easily readable ROOT nTuples. Sensitivity Module uses the output from flreconstruct to generate nTuples containing both simulated and reconstructed data. The combination of true and reconstructed data forms can be used to validate an analysis, by ensuring the true data supports inferences made using the reconstructed data.

Sensitivity Module can be uniquely compiled to add supplementary nTuple branches, containing a multitude of variables that may not already be encompassed into the pipeline. This allows additional parameters to be investigated as long as they can be computed from the Falaise data banks. By establishing the parameters necessary for identifying double beta decays, the selected parameters can be used to devise a double beta candidate cut flow.

The cut flow is a sequential application of data cuts, to determine the number of events in a particular decay channel, such as the  $2e$  signal channel or one of the many background channels ( $e\alpha$  and  $e\gamma$ ). Events that pass all of the selected cuts are labelled as candidate events for the corresponding decay channel. During experimentation, the cut flow will be used on real data to probe various channels. By measuring the efficiency of reconstructing backgrounds in the two electron channel, the contribution of individual backgrounds to the  $0\nu\beta\beta$  sensitivity can be determined.

## 4.2 Reconstructed Topologies

To identify double beta candidate events from reconstructed data, the reconstructed topology of charged particles must first be established so that the corresponding cuts can be identified and applied to the Sensitivity Module root nTuples. A double beta candidate event, in the 2e channel has a two electron topology, so the reconstructed topology of two electrons are combined. For the multitude of different background channels like  $e\alpha$  and  $e\gamma$ , the reconstructed topologies of the photon and alpha particle are required.

### 4.2.1 Electrons and Positrons

Electrons are the primary particles for double beta decay so it is vital they are identified and differentiated from other particle topologies. Within the Falaise environment, the light charged particles (electron/positron) are characterized by a curved reconstructed track, with a vertex on the source foil and an associated calorimeter hit, as defined above. The subtle difference between the particle topology of an electron and a positron is the curvature of the track under an applied magnetic field as shown in figure 4.3. As a result of its' positive charge, the positron curves in the opposite direction to the electron; clockwise from a top down perspective. Whereas the negatively charged track curves anti-clockwise from a top down view. The curvature of a charged particle is also dependant upon the direction of travel, so for a positron travelling from the calorimeter to the source, the direction of curvature is identical to an electron travelling from the source to the calorimeters and vice versa. Charged particles travelling from the calorimeters to the foil can still be differentiated from source electrons by using timing and time of flight cuts.

Electrons and positrons are identical under reconstruction until the charge is identified. For no field there is no separation of charge and so electrons and positrons cannot be differentiated. By separating electrons and positrons, double beta candidate events that involve positrons can be identified and removed. The electron topology is most important for probing the 2e channel which is the decay channel used to search for neutrinoless double beta decay. The requirements for double beta candidate events in the two electron channel will be discussed in section 6.1.

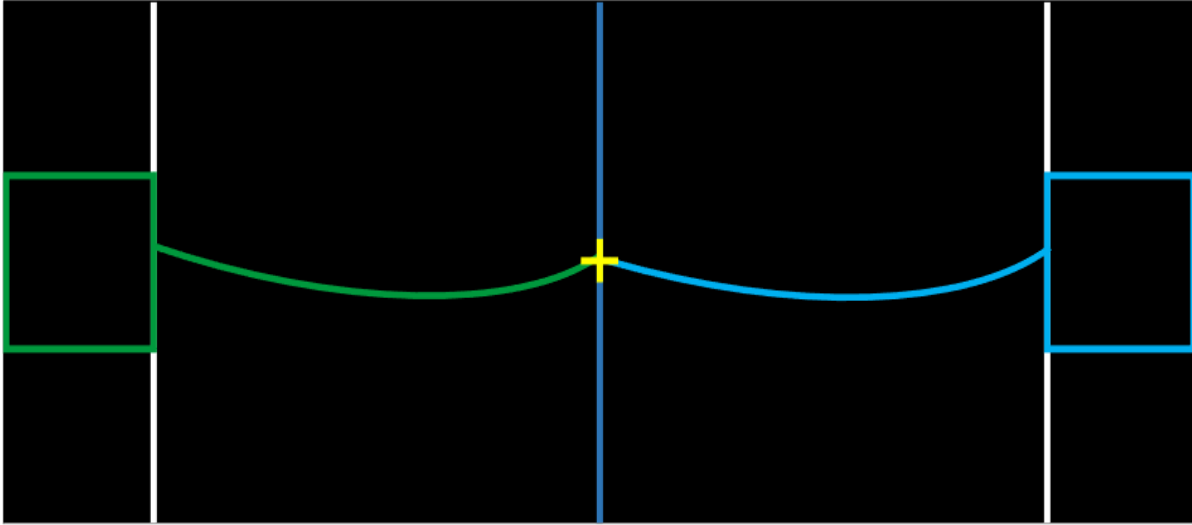


Figure 4.3: Representation of a reconstructed event with two charged particle tracks, the first belonging to an electron (blue track) and the second to a positron (green track), with an initial decay vertex on the source foil.

#### 4.2.2 Gammas

When attempting to identify and measure the activities of selected backgrounds, it is important to establish the reconstructed topology of particles other than the electron and positron. Neutrinos are of course undetectable by the SuperNEMO demonstrator however the detector does allow for both photons and alpha particles to be identified. The beta decay of  $^{208}\text{Tl}$  results in the emission of multiple photons alongside the beta electron and  $^{214}\text{Bi}$  beta decay is followed by the emission of a delayed alpha particle (figures 6.2 and 6.3). Establishing the additional particles that constitute these background decays helps to identify and remove them, reducing the total background count.

Unlike electrons and positrons, photons do not leave tracks in the detector and can only be identified by unassociated calorimeter hits, that is, calorimeter hits with no associated track or initial vertex. Furthermore, the time of flight cuts (internal and external probabilities) can be used to determine whether the timing of the unassociated calorimeter hit corresponds to that of a photon or an electron travelling from the source foil to the calorimeter. Calorimeter hits with energies lower than the detector trigger energy of 50 keV are labelled as noise regardless of whether there is an associated track or not. Reconstructed gammas often have noise hits close to the stricken calorimeter, however if the energies of these hits are below 50 keV, again the hits are labelled as noise. In the Falaise environment gammas can be identified by a yellow calorimeter hit with a dashed yellow originating at the particle source, as illustrated in figure 4.4.

The  $1e2\gamma$  channel is the main gamma background channel and the primary channel for measuring the contamination of  $^{208}\text{Tl}$ . The  $1e2\gamma$  channel contains events with a single electron accompanied

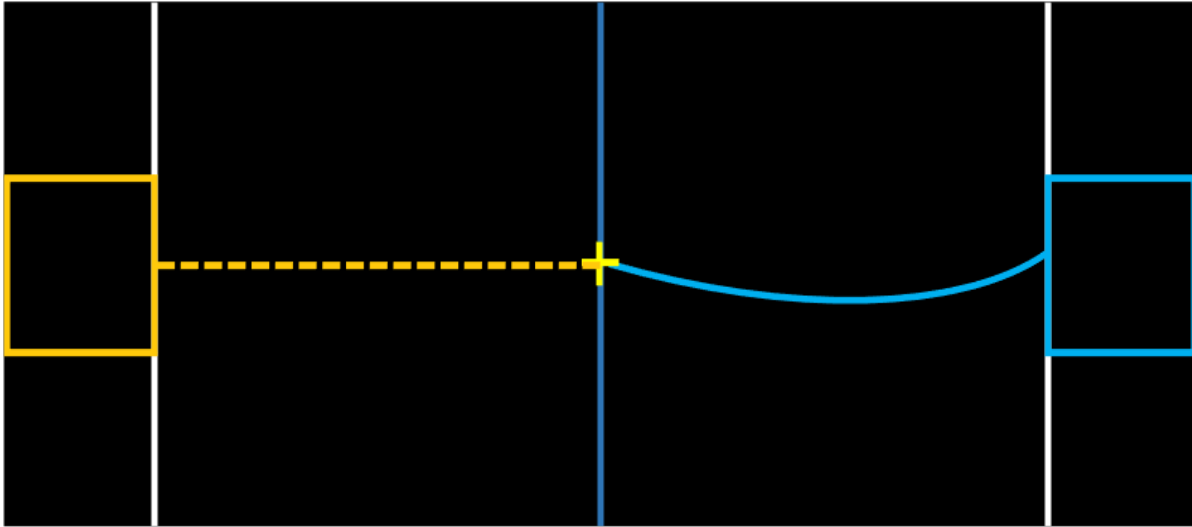


Figure 4.4: Representation of a reconstructed event with one electron (blue track) as well as a photon (yellow calorimeter hit with an unassociated/dashed track), with an initial decay vertex on the source foil.

by two photons. For  $^{208}\text{Tl}$ , the majority (99.8%) of decays result in the emission of a high energy 2.6 MeV photon which is often emitted alongside a number of lower energy photons. The decay scheme of  $^{208}\text{Tl}$  is complicated (figure 6.2) and can result in more than two photons being emitted from the decay, however the most populated background channel is the  $1e2\gamma$  channel. Measuring  $eN\gamma$  channels combines the reconstructed topologies of the electron and gamma, with addition of a shared vertex between the particles. Similarly,  $^{214}\text{Bi}$  decays can result in the emission of multiple photons although the addition of the delayed alpha in  $^{214}\text{Bi}$  beta decay allows for it to be measured in the  $1e1\alpha$  decay that will be discussed in the following section.

### 4.2.3 Alphas

Alpha particles have short straight delayed tracks, confined to the tracker volume. The large mass of the alpha particle suppresses its propagation through the tracker and it rapidly loses its energy within the tracker in close vicinity to the source foil. The main source of alpha particles for SuperNEMO is the beta decay of  $^{214}\text{Bi}$  to  $^{214}\text{Po}$ , from the  $^{238}\text{U}$  decay chain shown in figure 3.8.  $^{222}\text{Ra}$  diffuses into the tracker volume and undergoes a number of decays, eventually resulting in the presence of  $^{214}\text{Bi}$  on the surface of the source foil and tracker wires.  $^{214}\text{Bi}$  undergoes beta decay to  $^{214}\text{Po}$  which subsequently decays via alpha emission, with a half-life of  $164.3 \mu$ . The short red track in figure 4.5 demonstrates a typical reconstructed delayed alpha track alongside an electron. As mentioned earlier in the chapter, the number of tracker hits for a reconstructed alpha can be fewer than the three tracker hits required for a charged particle track. For non delayed tracker hits that are not part of a larger track, the hits are registered as noise, whereas isolated delayed hits are

reconstructed as alphas.

Reconstructed alphas permit the BiPo ( $^{214}\text{Bi}$ - $^{214}\text{Po}$ ) activity to be measured in the  $1e1\alpha$  channel, throughout the detector. The rate of  $1e1\alpha$  decays and consequently the BiPo activity within the different parts of the detector can be used to determine the contamination level of  $^{214}\text{Bi}$  at those locations. For the  $1e1\alpha$  channel, the reconstructed variables outlined for the electron and alpha, are combined with the following additional constraints:

- There only being one prompt track
- The delayed alpha track occurs at least  $4\mu\text{s}$  after the prompt electron track
- The two tracks share a vertex

As no other SuperNEMO background produces a delayed alpha, the  $1e1\alpha$  channel can be precisely measured to determine the BiPo activity.

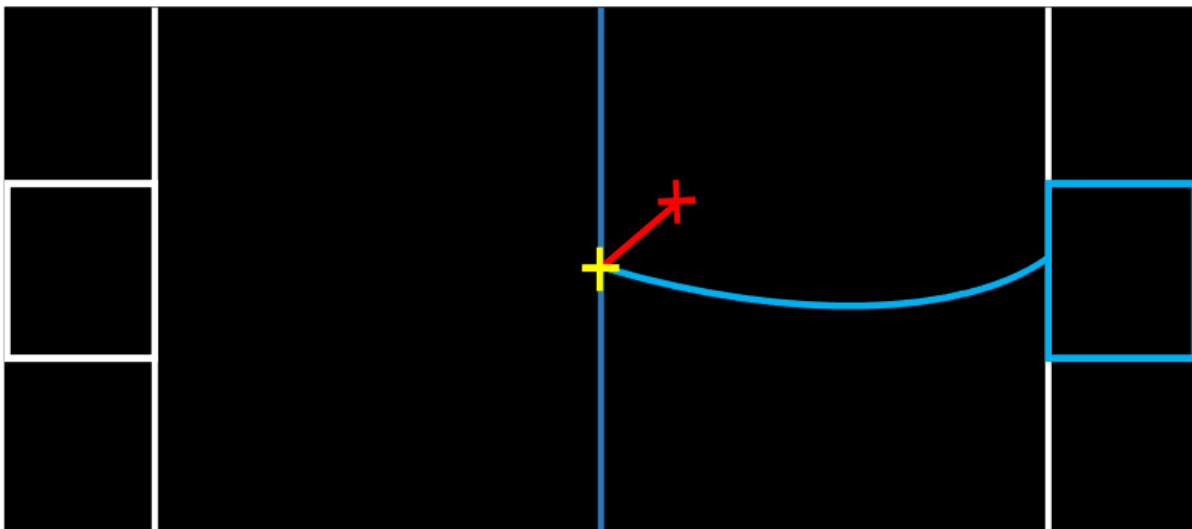


Figure 4.5: Representation of a reconstructed event with one electron (blue track) as well as an alpha (short red track), with an initial decay vertex on the source foil.

### 4.3 Internal/External Hypothesis

Any internal contribution, whether signal ( $0\nu\beta\beta$ ) or background, must originate from within the source foil and should not be induced by interactions originating from a source external to the  $^{82}\text{Se}$  source foil. Time of flight information is used to establish the origin of the initial decay. The time of flight cuts used are the internal and external probabilities, which estimate the probability that a reconstructed event was induced by a decay interior or exterior to the source foil. The external probability does not differentiate between an event originated from radon in the tracker or one of the many external background sources outlined earlier. For  $0\nu\beta\beta$ , time of flight information is most useful for identifying and removing double beta like events that may have originated from a source external to the source foil, whilst simultaneously the internal probability is used to ensure that any real double beta decays originated from within the source foil.

The internal hypothesis assumes a measured particles originated from within the source foil and the probability of this hypothesis can be calculated using the calorimeter hit timing of the particles. To calculate the internal probability, given two different calorimeter hit times  $t_1^{\text{meas}}$  and  $t_2^{\text{meas}}$ , first the theoretical time of flight  $t_i^{\text{tof}}$  is calculated using

$$t_i^{\text{tof}} = \frac{l_i}{\beta_i} \quad (4.1)$$

with  $l_i$  the length of the particle track which is curved for charged particles and straight line for photons. Additionally, for photons  $\beta_i = 1$  and for electrons is calculated using

$$\beta_i = \frac{\sqrt{E_i(E_i + 2m_e)}}{E_i + m_e} \quad (4.2)$$

with  $E_i$  the calibrated energy recorded by the calorimeter and  $m_e$  the rest mass of an electron. The emission time of a particle,  $t_i^{\text{int}}$ , takes into account the measured time in the calorimeter as well as the theoretical time of flight and is given as

$$t_i^{\text{int}} = t_i^{\text{meas}} - t_i^{\text{tof}} = t_i^{\text{meas}} - \frac{l_i}{\beta_i} \quad (4.3)$$

A  $\chi^2$  test representing the approximately Gaussian timing distribution is used with the corresponding  $\chi^2$  variable

$$\chi_{\text{int}}^2 = \frac{\left( \left( t_1^{\text{meas}} - \frac{l_1}{\beta_1} \right) - \left( t_2^{\text{meas}} - \frac{l_2}{\beta_2} \right) \right)^2}{\sigma_{t_1^{\text{int}}}^2 + \sigma_{t_2^{\text{int}}}^2} \quad (4.4)$$

where  $\sigma_{t_i^{\text{int}}}^2$  represents the variance of the emission timing  $t_i^{\text{int}}$ .  $\sigma_{t_i^{\text{int}}}^2$  depends on multiple factors including the uncertainties on the measured time, particle speed and distance travelled. For photons, the particle speed is  $c$  and so there is no uncertainty on this value, however the uncertainty surrounding the path length is unknown as photons are not tracked in SuperNEMO.

$\chi_{\text{int}}^2$  is converted into a probability by transforming the Gaussian distribution into a flat distribution between 0 and 1. The internal probability is therefore defined as

$$P(\chi_{\text{int}}^2) = 1 - \frac{1}{\sqrt{2\pi}} \int_0^{\chi_{\text{int}}^2} x^{-\frac{1}{2}} e^{-\frac{x}{2}} dx \quad (4.5)$$

Unlike the internal hypothesis, the external hypothesis assumes an incident external photon interacts with the detector to produce either a  $1e1\gamma$  event or a crossing electron. The external background results in the generation of an event in the  $2e$  channel via a number of mechanisms that will be outlined later on. Calculating the external probability is done in a similar manner to the internal probability, but the time of flight  $t^{\text{tof}}$  is given as

$$t^{\text{tof}} = \frac{l_1}{\beta_1} + \frac{l_2}{\beta_2} \quad (4.6)$$

which sums the timing for both particle tracks.

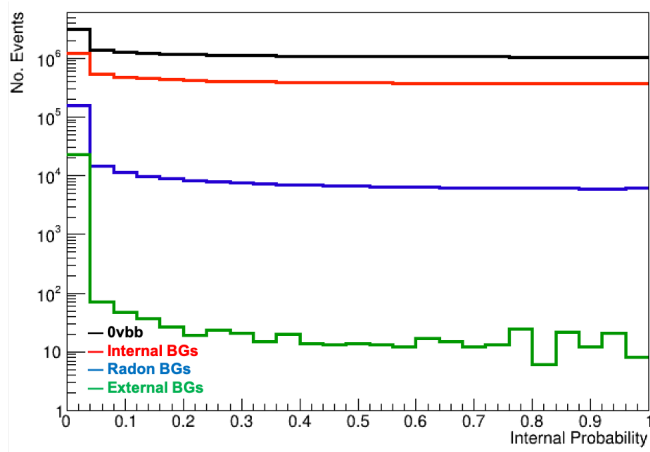
The  $\chi^2$  for the external hypothesis is then

$$\chi_{\text{ext}}^2 = \frac{\left( (t_2^{\text{meas}} - t_1^{\text{meas}}) - \left( \frac{l_1}{\beta_1} + \frac{l_2}{\beta_2} \right) \right)^2}{\sigma_{t_1^{\text{ext}}}^2 + \sigma_{t_2^{\text{ext}}}^2} \quad (4.7)$$

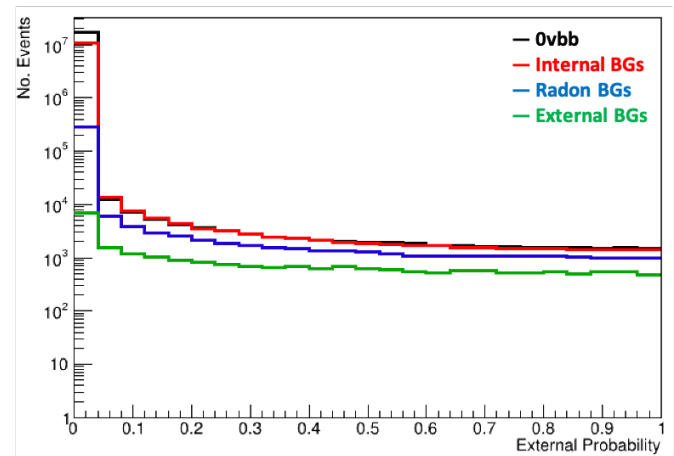
where  $\sigma_{t_i^{\text{ext}}}^2$  is the equivalent variance of emission for the external hypothesis. Like the internal probability in equation 4.5, the external probability is calculated with

$$P(\chi_{\text{ext}}^2) = 1 - \frac{1}{\sqrt{2\pi}} \int_0^{\chi_{\text{ext}}^2} x^{-\frac{1}{2}} e^{-\frac{x}{2}} dx \quad (4.8)$$





(a) Internal probability



(b) External probability

Figure 4.6: Internal probability for  $0\nu\beta\beta$ , internal, radon and external backgrounds with reconstructed  $2e$  topologies. The internal probability distributions were calculated using the equation above

#### 4.4 Number of Expected Events

In order to determine the contribution of different backgrounds to a decay channel (for  $0\nu\beta\beta$  this is the 2e channel), the number of expected events ( $N_{exp}$ ) of the background is first calculated. The number of expected events represents the total number of expected decays of a particular background during the detectors operational lifetime and is calculated differently for backgrounds located in different parts of the detector in order to correctly represent the changing exposure throughout the detector. The ratio of successfully reconstructed events in a given channel, from a known number of Monte Carlo simulations is denoted the detection efficiency and is given as the following,

$$\epsilon = \frac{N_{Survived}}{N_{TOTMC}} \quad (4.9)$$

with  $N_{Survived}$  equal to the number of events that pass all the cuts and  $N_{TOTMC}$  the total number of simulated events. The number of expected events of  $^{82}\text{Se}$  two neutrino double beta decay, in the source foil, is given by,

$$N_{2\nu\beta\beta} = \frac{N_A \times \ln 2 \times \epsilon \times m \times t}{T_{1/2}^{2\nu\beta\beta} \times M(^{82}\text{Se})} \quad (4.10)$$

where  $N_A$  is Avogadro's constant,  $\epsilon$  is the previously quoted reconstruction efficiency ratio,  $m$  is the total mass of the  $^{82}\text{Se}$  source foil (6.23 Kg),  $t$  is the total run time of the experiment,  $T_{1/2}^{2\nu\beta\beta}$  is the half life of  $^{82}\text{Se}$  and  $M(^{82}\text{Se})$  is the mass number for  $^{82}\text{Se}$ . For other internal backgrounds, such as  $^{208}\text{Tl}$  and  $^{214}\text{Bi}$ , the number of expected events is

$$N_i = A_i \times \epsilon_i \times m \times t \quad (4.11)$$

with  $A_i$  and  $\epsilon_i$  designated as the activity and reconstruction efficiency respectively, for background  $i$ .

Radon induced backgrounds are calculated using the activity of the background within the volume of the tracker chamber. The volume of the tracker replaces the source foil mass in equation 4.11 and so the number of expected events for Radon simulations is given by,

$$N_i = A_i \times \epsilon_i \times V \times t \quad (4.12)$$

with  $V$  as the volume of the tracker chamber. External backgrounds were only simulated on the PMT glass bulbs, so the activity is a proportion of the total activity from the entire PMTs. The number of expected events for external backgrounds is given by,

$$N_i = A_{Glassbulb,i,j} \times \epsilon_i \times t \quad (4.13)$$

with  $A_{Glassbulb,i,j}$  the activity of the PMT glass bulb for a given background  $i$  and PMT location  $j$ .

The number of expected events represents the total contribution of a decay to a particular channel. For SuperNEMO, the signal detection efficiency and the contribution of different backgrounds in the 2e channel are used in order to estimate the overall  $0\nu\beta\beta$  half-life sensitivity of the demonstrator.

## 4.5 Half-Life Calculation

The sensitivity of an experiment is often given as a half-life  $T_{1/2}$ , which incorporates the detection efficiency and  $N_{exp}$  from section 4.4. To derivation of the half-life formula is shown below, starting with the exponential decay of a radioactive isotope,

$$N(t) = N(0)e^{-\lambda t} \quad (4.14)$$

with  $N(t)$  the number of remaining atoms of the isotope at time  $t$ ,  $N(0)$  the number of atoms at the beginning of the experiment and  $\lambda$  the decay constant.  $\lambda$  is related to the half-life  $T_{1/2}$  by the following

$$\lambda = \frac{\ln(2)}{T_{1/2}} \quad (4.15)$$

The half-life of two neutrino  $^{82}\text{Se}$  double beta decay is approximately of the order  $10^{20}$  years and even greater for neutrinoless double beta decay so equation 4.14 can be Taylor expanded in  $\lambda t$  to give the approximation

$$e^{-\lambda t} \simeq (1 - \lambda t) \quad (4.16)$$

The number of observed events can therefore be written as

$$N_{\text{obs}} = \epsilon N(0) (1 - e^{-\lambda t}) \simeq \epsilon N(0) \lambda t = \epsilon N(0) \frac{\ln(2)}{T_{1/2}} t \quad (4.17)$$

with the  $\epsilon$  the detection efficiency of  $0\nu\beta\beta$  and  $t$  the running time of experimentation. The number of atoms at the beginning of the experiment,  $N(0)$  is given by

$$N(0) = \frac{N_A m}{A} \quad (4.18)$$

and by inserting the definition of  $N(0)$  into equation 4.17, the half life of  $0\nu\beta\beta$  can be calculated using

$$T_{1/2} = \frac{\epsilon}{N_{\text{obs}}} \frac{N_A m}{A} \ln(2)t \quad (4.19)$$

### 4.5.1 Half Life Approximation

There are various methods to approximate the half-life sensitivity established in section 4.5 , the most common of which use the entire energy spectrum of both signal and background and separate them to determine their respective contributions. In this thesis, a basic counting approach is utilized, which determines the number of expected events found in a selected energy window to calculate the half-life. For  $^{82}\text{Se}$  neutrinoless double beta decay, the initial counting window is established as 2.8 to 3.2 MeV (highlighted in figure 4.7), encompassing the  $^{82}\text{Se}$  Q valu, corresponding to the peak of the  $0\nu\beta\beta$  energy distribution. Counting methods are less precise than the more thorough complete energy spectrum methods, however as this thesis is a comparative analysis to determine which of the three magnetic field is most suitable for detector operation, a less precise but relative study between the three magnetic fields is beneficial. By attempting to compare the relative performance of the three magnetic fields, the precision of the sensitivity estimation can be compromised in order to increase the speed of the analysis.

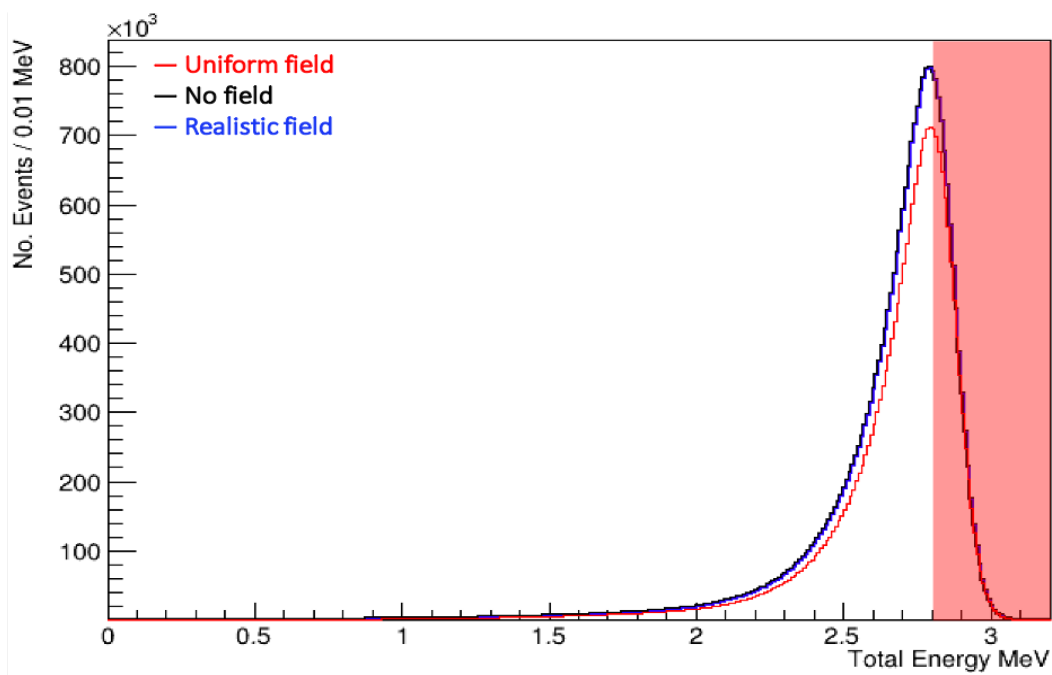


Figure 4.7: Energy spectra of  $0\nu\beta\beta$  for all three magnetic field configurations, highlighting the region of interest (2.8 - 3.2 MeV)

## 4.6 Limit Setting Procedures

As mentioned, for this work, a counting approach is utilized for estimating the half-life sensitivity of the SuperNEMO demonstrator. The first counting method is a Gaussian approximation, which is particularly useful for studies with low numbers of expected backgrounds. For the Gaussian approximation at 90% CL,  $T_{1/2}^{0\nu}$  is defined as,

$$T_{1/2}^{0\nu} > 4.16 \times 10^{26} \text{yr} \left( \frac{\epsilon amt}{M(^{82}\text{Se})} \right) \left( \frac{1}{1.64\sqrt{N_B}} \right) \quad (4.20)$$

with  $\epsilon$  the efficiency of detecting  $0\nu\beta\beta$  (from equation 4.9),  $a$  the isotopic abundance (given as 1 for the refined source foil),  $mt$  the exposure,  $M(^{82}\text{Se})$  the  $^{82}\text{Se}$  mass number and  $N_B$  the number of expected background events. The  $\sqrt{1.64}$  denominator term represent a 90% confidence level (CL). Although not as precise as the other methods, the Gaussian approximation is a simple and fast approach for comparing the performance of three magnetic field configurations, although as the number of background events increases, the precision of the Gaussian approximation reduces significantly.

### 4.6.1 Poissonian Window Approximation

An alternative to the Gaussian approximation is the Poissonian approximation which provides greater precision for an analysis with increased statistical data. Poissonian approximations use equation 4.19 with the extraction of  $N_{obs}$  dependent upon a selected method. The methods used to calculate the number of observed events include the Helene method from [29], the Feldman-Cousins method found in [30] and finally the Minimum Detectable Activity (MDA) method all of which are outlined below.

### 4.6.2 Helene Method

The Helene method described in [29] outlines three different variables:

- A - which is the upper limit of the peak and the value used for  $N_{obs}$ .
- B - the number of background events
- C - the total event count in a known bin

Using a defined confidence limit (usually 90%), the value for A can be determined from the graphs shown below, where B takes the X axis and C is the curve from which the corresponding value of A can be extrapolated from. In this case  $C \approx B$  as the number of backgrounds is calculated the region of interest which is also the binned region for C.

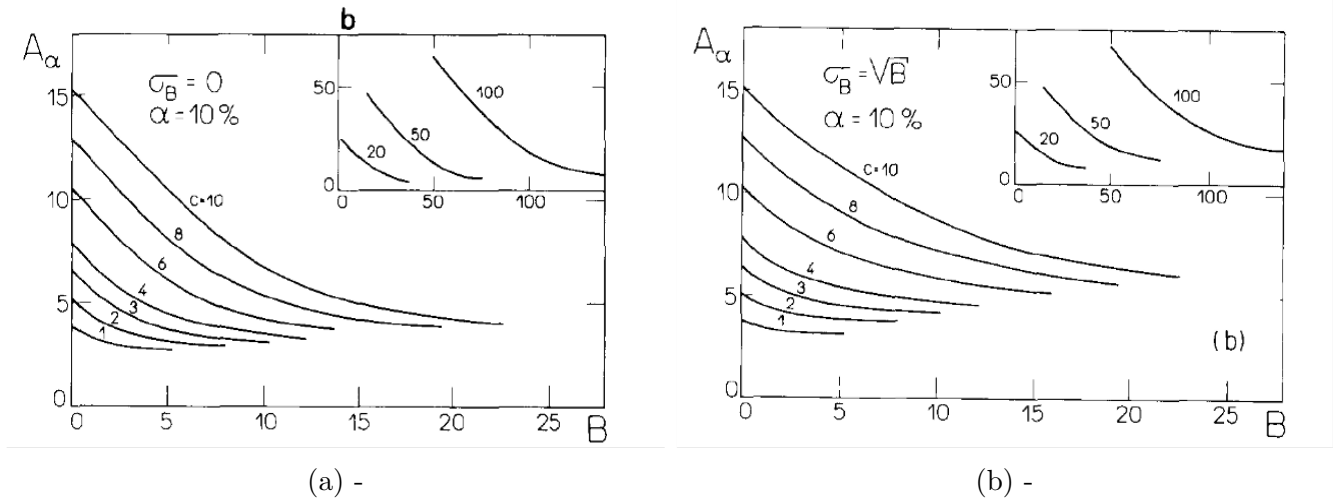


Figure 4.8: Helene where  $\sigma_b$  is the error on the background and  $\alpha$  is equal to 1 - CL

### 4.6.3 Feldman-Cousins

The Feldman-Cousins approach is often used to quote limits on the size of a signal, given the background contamination. For a known background and confidence limit, for a Poissonian signal such as equation 4.21, Feldman-Cousins provides an estimate for  $N_{\text{obs}}$  which is then used to calculate equation 4.19.

$$P(s | b, N) = \frac{e^{-(s+b)}(s+b)^N}{N!} \quad (4.21)$$

## 4.7 Minimum Detectable Activity

In this thesis, the definition used for the minimum detectable activity is the definition given in 'Radiation Detection and Measurement' by G. F. Knoll. Knoll uses a binary pretence of whether the detector output represents a background only or that there is also the presence of signal.

the probability of a false positive is established as the probability a signal event is present even though only background is present and a false negative is established as the probability a signal event is misidentified as a background.

To determine the presence of signal, a critical count number  $n_c$  is defined and if the total observed count number is greater than  $n_c$ ,

the definition of Minimum Detectable Activity (MDA) given in 'Radiation Detection and Measurement' by G. F. Knoll is used

G. Knoll, Radiation Detection and Measurement, ISBN-9780470131480 (2000)

\*\*\* Yet to complete \*\*\*



# Chapter 5

## Double Beta Decay Event Selection

The sensitivity to neutrinoless double decay is the primary metric of success for the magnetic field analysis described in this work. The results from the double beta decay simulations (signal) will be discussed, including the impact of the 2e topology cuts from chapter 4 on the concurrent and final detection efficiency for each of the three magnetic field scenarios. For the  $0\nu\beta\beta$  analysis,  $2\nu\beta\beta$  is treated as a background and contributes to the total background contamination. The high energy window/region of interest established in the previous chapter ensures the contamination of  $2\nu\beta\beta$  is suppressed however a very small number of  $2\nu\beta\beta$  events still remain. Additionally, the best case scenario SuperNEMO detector will be discussed, that is, a radiopure detector with only  $2\nu\beta\beta$  as an irreducible background to  $0\nu\beta\beta$ . With improved processing methods it may be feasible to reduce or eliminate other backgrounds, improving detector conditions for probing neutrinoless double beta decay.

### 5.1 Neutrinoless Double Beta Decay ( $0\nu\beta\beta$ )

The primary goal of the SuperNEMO experiment is to search for the neutrinoless double beta decay of  $^{82}\text{Se}$ , by optimising the sensitivity of the detector to the decay. Parallel to this, SuperNEMO aims to improve on the previous half-life measurement for the two neutrino decay of  $^{82}\text{Se}$  and increase the precision of the two neutrino decay nuclear matrix elements. In order to determine the neutrinoless double beta decay sensitivity, the detection efficiency of  $0\nu\beta\beta$  (equation 4.9) must first be extracted from simulated data. For each of the three magnetic fields,  $10^8$  simulated decays of  $0\nu\beta\beta$  were uniformly distributed in the bulk of the source foil using the official Falaise 4.0.0 reconstruction with an exposure of  $15.275 \text{ Kg yr}^{-1}$  ( $6.110\text{Kg} \times 2.5 \text{ years}$ ). As previously mentioned, the cut flow is applied to simulated data in order to extract  $N_{Survived}$ , which is used to calculate the detection efficiency of the simulated isotope in the 2e channel and is briefly described below.

## 5.2 Identifying Double Beta Events

The search for  $^{82}\text{Se}$  neutrinoless double beta decay is measured in the two electron channel, but not all events found in the two electron channel are necessarily from real double beta decays and may in fact materialise from specific backgrounds. The reconstructed topology of an electron was established, in section 4.2.1, as a negatively curved track with a vertex on the source foil and an associated calorimeter hit. For a double beta candidate event in the 2e channel, the reconstructed topologies of two electrons are combined with additional constraints, all of which are outlined below.

### 5.2.1 2e Channel Selection

- Two calorimeter hits

Two calorimeter hits above 50 keV, with at least one hit above 150 keV, measuring the energies of the two double beta decay electrons. The minimum energy requirement is determined by the trigger energy of the detector.

- Two tracker clusters and two tracks

Two tracks, derived from two tracker clusters are selected to represent the tracks of the two emitted electrons during double beta decay.

- Each track associated to a unique calorimeter

Each track is associated to a calorimeter ensuring the two beta electron tracks correspond to the two calorimeter hits. Additionally the two calorimeter hits belong to two unique calorimeters. One of the main benefits of SuperNEMO is that it allows the energy of each individual electron to be measured which can only be achieved when electrons hit separate calorimeters.

- Two vertices on the source foil

The two electron vertices should be located on the source foil, ensuring a reconstructed path from the foil, through the tracker and finally into the calorimeters for the two electrons.

- Internal and External Probability

The timing of the calorimeter hits must be within a certain boundary to ensure the electrons originated from within the source foil and did not enter the tracker from an external source. Internal and external probability essentially act as time of flight cuts.

- No Positrons

The double beta decay charged particle tracks can belong to either electrons or positrons. The charge of each track can be identified from the curvature of the track so electrons and positrons can be differentiated. Identifying both tracks as electrons is the final step for 2e

selection.

### 5.2.2 2e Channel Optimization

The 2e channel cuts help to identify double beta candidate events however additional cuts are necessary for improving the overall detection efficiency of double beta decay simulations. Three additional optimization cuts are,

- Maximum vertex separation

The maximal separation between the vertices is  $\Delta R < 1\text{cm}$  and  $\Delta Z < 3\text{cm}$ , where  $\Delta R$  represents the radial separation and  $\Delta Z$  the vertical separation.

- No delayed alpha tracks

No delayed/alpha tracks, between 13 and 700  $\mu$ . The 13  $\mu\text{s}$  lower limit includes detector effects like the tracker response time and the upper limit is approximately  $4 \times$  the half-life of  $^{214}\text{Po}$ . The delayed window is kept open so as to measure BiPo decays.

- ROI energy

No events are allowed outside of the energy window (ROI). The nominal ROI is 2.8 - 3.2 MeV for  $^{82}\text{Se}$ , however the ROI is subject to optimization. The ROI selects a bin of a specified width for estimating the sensitivity using a counting method.

Together, the two electron channel and optimization cuts combine to form the double beta decay cut flow, for the purpose of extracting the detection efficiency and subsequently the contribution of background decays, such as  $2\nu\beta\beta$ , to the  $^{82}\text{Se}$  sensitivity. The cuts are selected in order to maximise the reconstruction efficiency of true double beta decays, whilst reducing the prevalence of background induced two electron events.

Cut Descriptions	Magnetic Field Configuration		
	Uniform Field	No Field	Realistic Field
Only two calorimeter hits above 50keV, at least one >150keV	0.562	0.594	0.589
Two tracker clusters with 3 or more cells	0.380	0.446	0.436
Two reconstructed tracks	0.378	0.443	0.433
Remove events with two electron hits to the same calorimeter	0.373	0.438	0.429
Each track associated to a calorimeter	0.338	0.400	0.390
Two vertices on the source foil	0.337	0.399	0.389
Vertex $\Delta R < 1\text{cm}$ and $\Delta Z < 3\text{cm}$ (separation between vertices)	0.240	0.281	0.274
Internal Probability >1% and External Probability <4%	0.226	0.265	0.259
No delayed alpha tracks (no tracks with $13\mu\text{s} < t < 700\mu\text{s}$ )	0.226	0.265	0.259
Remove positrons (unavailable for no field)	0.211	- <sup>†</sup>	0.179
ROI energy (between 2.8 and 3.2 MeV)	0.0653	0.0790	0.537

Table 2:  $0\nu\beta\beta$  cut flow for the three B field configurations. Each row lists a short description of the cut as well as the concurrent detection efficiency.

<sup>†</sup>For no field, the no positron cut is not applied as without a magnetic field, the charges of the particle tracks are indeterminable. The magnetic field curves electrons and positrons in opposite directions as a result of their differing charges and so without a magnetic field, the charged particle tracks are straight, ignoring any low energy scattering.

The breakdown of the  $0\nu\beta\beta$  cut flow is provided in table 2, illustrating how the detection efficiency changes with each sequential cut. A short description of each of the cuts is provided. The cut flow follows the ordering shown in section 5.2.1, however the three additional optimization cuts; the maximum vertex separation, no delayed tracks and the energy window (or ROI) are added to the cut flow as cuts seven, nine and eleven respectively. The order of the cut flow is important for studying the impact of each individual cut on the concurrent detection efficiency and importantly, understand how the different magnetic fields influence the overall final detection efficiency. In the following section, a short explanation for the difference in detection efficiency between the three fields is given for the most impactful cuts.

### 5.2.3 Most Impactful Cuts

\*\*\* intro here all cuts but some impactful and target specific backgrounds\*\*\*

Applying the two calorimeter cut removes almost 50% of events, for all three magnetic fields. Requiring two calorimeter hits is most effective for removing  $1e2(+)\gamma$  events that have more than two calorimeter hits and any  $1e$  events from background decays or improper double beta decays where one of the electrons doesn't escape the foil or tracker volume. Removing events with two electron hits to the same calorimeter ensures the energy of individual electrons can be measured which is one of the significant advantages of the SuperNEMO demonstrator. The fifth cut, which requires both particle tracks to be associated to a calorimeter, targets both  $1e1\gamma$  and  $1e1\alpha$  backgrounds that have only one associated track, belonging to the single electron.

Additional noteworthy cuts include the vertex separation, no positron and finally the ROI window. The vertex separation cut applies a harsher constraint compared to previous studies. In [31],  $\Delta R$  is required to be  $<6\text{cm}$  and  $\Delta Z <7\text{cm}$ , culminating in over 95% of double beta candidate events from the source foil surviving the cut, compared to the approximately 70% survival rate with  $\Delta R <1\text{cm}$  and  $\Delta Z <3\text{cm}$ . The appointed constraint is a consequence of the expected spatial resolution of roughly 8% , with an effective maximum longitudinal resolution of  $\approx 1.1\text{ cm}$  at the mid length of a cell [32].

The penultimate no positron cut is used to remove double beta candidate events that have at least one charged particle labelled as a positron. As previously stated, the no positron cut is inapplicable for the no field scenario. Moreover, the cut removes a large number of events for the realistic field, around 30%, and close to 7% of events for the uniform field, as the increased field strength increases the efficiency of labelling charged particles correctly. Finally, the energy window removes the majority of remaining events as the ROI encompasses only a small segment of the overall energy spectrum. Between the three magnetic fields, the shape of the spectra is unchanged, resulting in a similar proportion of events removed.

### 5.3 Two Neutrino Double Beta Decay ( $2\nu\beta\beta$ )

Cut Descriptions	Detection Efficiency $\epsilon$		
	Uniform Field	No Field	Realistic Field
Only two calorimeter hits above 50keV, at least one >150keV	0.237	0.287	0.279
Two tracker clusters with 3 or more cells	0.147	0.205	0.195
Two reconstructed tracks	0.146	0.204	0.194
Remove events with two electron hits to the same calorimeter	0.143	0.201	0.191
Each track associated to a calorimeter	0.125	0.179	0.170
Two vertices on the source foil	0.125	0.178	0.169
Vertex $\Delta R < 1\text{cm}$ and $\Delta Z < 3\text{cm}$ (separation between vertices)	0.072	0.101	0.096
Internal Probability >1% and External Probability <4%	0.068	0.095	0.090
No delayed alpha tracks (no tracks with $13\mu\text{s} < t < 700\mu\text{s}$ )	0.068	0.095	0.090
Remove Positrons (unavailable for no field)	0.063	- <sup>†</sup>	0.060
ROI energy (between 2.8 and 3.2 MeV)	$3 \times 10^{-8}$	$2 \times 10^{-8}$	$1 \times 10^{-8}$
Number of Expected Events	0.15 $\pm 0.09$	0.10 $\pm 0.07$	0.05 $\pm 0.05$

Table 3:  $2\nu\beta\beta$  cut flow and number of expected events for all three magnetic field configurations. Each row lists a short description of the cut as well as the concurrent detection efficiency for each magnetic field.

<sup>†</sup> No positron cut for no field scenario.

The cut flow for  $2\nu\beta\beta$  double beta candidate events is shown in table 3, alongside the number of expected events with 2.5 years of exposure. The overall detection efficiency is significantly lower for  $2\nu\beta\beta$  compared to  $0\nu\beta\beta$ , particularly in the ROI, where the detection efficiencies are of the order  $10^{-8}$ . A low detection efficiency for  $2\nu\beta\beta$  is important when measuring the sensitivity to neutrinoless double beta decay as  $2\nu\beta\beta$  is the single irreducible background for the neutrinoless search.

The sum of the two electron distribution is shown in figure 5.1. For neutrinoless double beta decay, the total energy correlates well with the expected Landau distribution seen for charged particles traversing a thin film. The distribution peaks around the decay energy of  $^{82}\text{Se}$  (\*\*reference Q energy from intro\*\*) and the Landau tail extends back to the 200 keV trigger energy. The shape of the distribution is unchanged between the three magnetic fields. The tail of the two neutrino distribution barely penetrates into the  $^{82}\text{Se}$  ROI, resulting in the low detection efficiencies for the three fields as shown in table 3. The majority of  $2\nu\beta\beta$  events are found at lower energies, with the peak of the distribution close to 1 MeV.

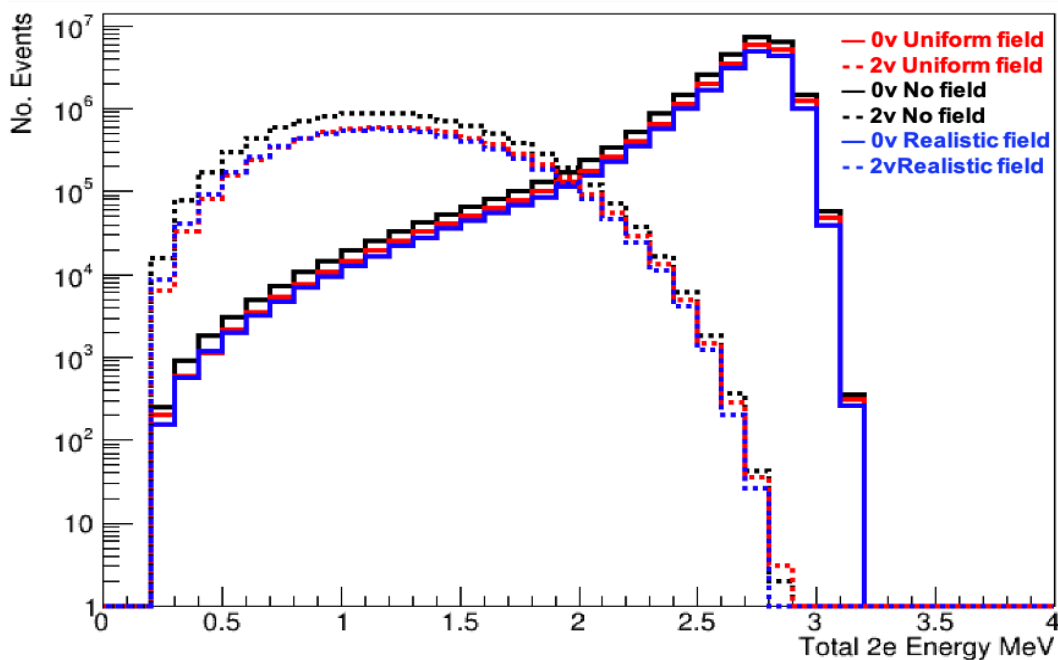


Figure 5.1: 2e energy spectra for  $0\nu/2\nu\beta\beta$  double beta candidate events.

SuperNEMOs modular structure provides the ability to reconstruct the entire topology of individual particles. One of the most important variables for studying the intermediate decay mechanism of  $^{82}\text{Se}$   $0\nu/2\nu\beta\beta$  decay, is the single electron energy. The single electron energy distribution is presented in figure 5.2, for both  $0$  and  $2\nu\beta\beta$  and can be used to infer the mechanism underlying the decay itself and whether the decay prefers HSD or SSD as discussed in chapter \*\*ref HSD/SSD

Again, the distribution shape is independent of the magnetic field choice, for both the neutrinoless and two neutrino decays.

Similarly, the angular distribution is also sensitive to the underlying decay mechanism of  $0\nu\beta\beta$  and the cosine of the angle between the two electron tracks is shown in figure 5.3. The  $\cos(\theta)$  curve for  $0\nu\beta\beta$  is expected to follow a  $1 - \cos(\theta)$  distribution, however, as shown in figure 5.3, the number of events reduces as you get closer to  $\cos(\theta) = 0$ . For  $2\nu\beta\beta$ , the angular distributions skew

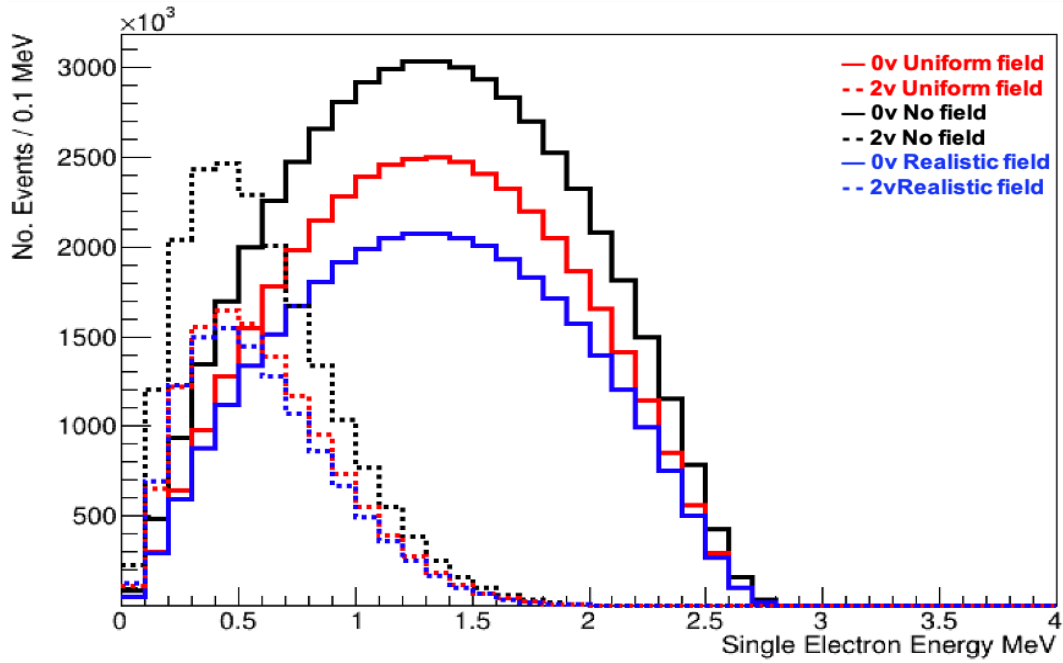


Figure 5.2: Single electron energy spectra for  $0/2\nu\beta\beta$  double beta candidate events.

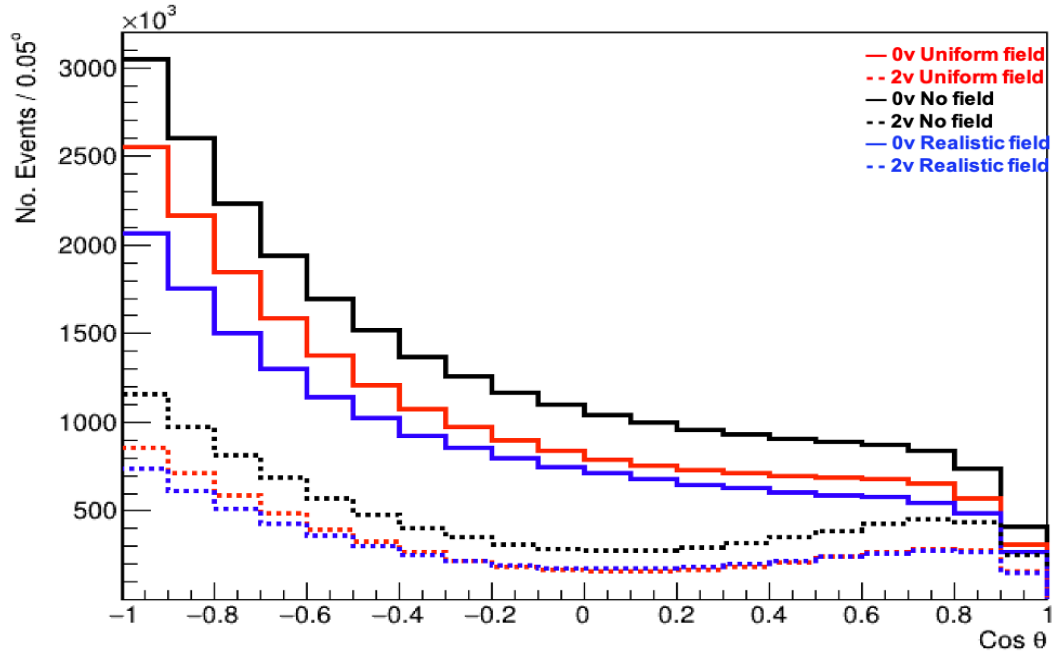


Figure 5.3:  $\text{Cos}\theta$  spectra for  $0/2\nu\beta\beta$  double beta candidate events of all energies.



towards lower angles, peaking at  $\cos(\theta) = 0.8$ . Again, the different magnetic fields do not bring about any change in the shape of the distribution. \*\*\*rid of detail + correct distribution ??? \*\*\*

### 5.3.1 SuperNEMO Sensitivity with $2\nu\beta\beta$ Background Only

Prior to investigating the contributions from the other background sources, it is useful to consider the case of the best case scenario detector, which only includes the irreducible  $2\nu\beta\beta$  as a background. Although SuperNEMO has a number of different backgrounds that contribute towards the  $^{82}\text{Se}$  ROI, from internal, radon and external sources, it may be possible to further reduce and perhaps eliminate all of the reducible backgrounds. To reduce the internal contamination, the source foils can undergo increased processing which is made easier by the modular structure of the SuperNEMO demonstrator, allowing the source foils to be easily removed and replaced. Radon and external backgrounds can be reduced by improving the radon flushing inside the tracker and increasing shielding prowess respectively. For the best case scenario detector, this would result in a reduction or elimination of all backgrounds leaving only  $2\nu\beta\beta$ . The best tool for minimising the  $2\nu\beta\beta$  backgrounds contribution is the decay energy. The  $2\nu\beta\beta$  total energy spectra is skewed to lower energies, whereas the  $0\nu\beta\beta$  energy spectra peaks around the  $^{82}\text{Se}$  ROI (figure 5.1), as there are no neutrinos to reduce the energy carried by the electrons. By maximising the energy resolution, the rare  $0\nu\beta\beta$  background peak can be most optimally separated from the  $2\nu\beta\beta$  background continuum, particularly when probing the ROI at the  $^{82}\text{Se}$  Q value. The width and position of the ROI is dependent upon the energy resolution of the experiment, so it is important to maximise this resolution, particularly for the ideal case scenario, where the most optimal strategy for separating the signal and  $2\nu$  background uses the measured energy of the decay progeny.

Using the associated cut flows and expected events, the sensitivity of the idealistic detector setup with no reducible backgrounds is shown in figure 4.

	Sensitivity $\times 10^{24}$		
	Uniform Field	No Field	Realistic Field
Sensitivity Gaussian $e^{24}$	7.97	11.80	1.14
Sensitivity Helene ( $A \approx 1$ )	-	-	-
Sensitivity Feldman-Cousins	2.22	2.63	1.75
MDA	-	-	-

Table 4:  $0/2\nu\beta\beta$  detection efficiency as well as the number of expected events for  $2\nu\beta\beta$

As mentioned in section 4.5, the Poissonian approximation provides greater precision with higher statistics but struggles with a number of expected backgrounds close to zero. However for a relative study between the three magnetic field scenarios it can still be useful for determining which magnetic field delivers the greatest detector sensitivity. Of the three fields, no field has the highest sensitivity with all three estimation methods, culminating in a sensitivity of  $1.180 \times 10^{25}$  with the Gaussian approximation, owing to the much greater detection efficiency of  $0\nu\beta\beta$ . \*\*\* calc detection efficiency of MDA \*\*\*

## 5.4 Summary of Double Beta Decays

	Magnetic Field Configuration		
	Uniform Field	No Field	Realistic Field
$0\nu$ Detection Efficiency	0.0653	0.0790	0.0537
$2\nu\beta\beta$ Detection Efficiency	$3 \times 10^{-8}$	$2 \times 10^{-8}$	$1 \times 10^{-8}$
$2\nu\beta\beta$ Number of Expected Events	$0.15 \pm 0.09$	$0.10 \pm 0.07$	$0.05 \pm 0.05$
Sensitivity Gaussian $e^{24}$	7.966	11.803	1.135
Sensitivity Helene	-	-	-
Sensitivity Feldman-Cousins	2.217	2.625	1.747
MDA	-	-	-

Table 5:  $0/2\nu\beta\beta$  detection efficiency as well as the number of expected events for  $2\nu\beta\beta$

Of the three magnetic field configurations, the no field scenario maintains the greatest detection efficiency after applying the two electron cut flow outlined in section 4.5. Additionally, as a result of the high energy region of interest, the two neutrino detection efficiency is suppressed and accordingly the background contribution is extremely small. When considering the ideal detector scenario, the highest sensitivity is achieved for no field as a result of the superior 0.0790 detection efficiency. The Poissonian approximations of the sensitivity are imprecise for low background statistics, nonetheless, when taking into account the additional background sources, the precision should improve. Although the idealistic detector assumes zero non DBD backgrounds, the current demonstrator module has non-zero background contributions from all different parts of the detector. To measure the sensitivity inclusive of the other backgrounds, the same procedure carried out to determine the  $2\nu\beta\beta$  background count will be used for the remaining reducible backgrounds.

# Chapter 6

## Estimation of Backgrounds for SuperNEMO

As demonstrated in section 4.5, the sensitivity to neutrinoless double beta decay is inversely proportional to the background level, therefore in order to maximise the sensitivity, the background contamination should be reduced or eliminated without significantly suppressing the signal detection efficiency. Additionally, the non-linear dependence between the sensitivity and background indicates an increase in sensitivity can still be achieved with a reduced signal detection efficiency as long as the background is reduced proportionally. The sensitivity can also be improved with an increased exposure (Activity  $\times$  Time), usually involving an increase in the source mass and run time of the experiment. Nevertheless, for the SuperNEMO demonstrator, the initial run time is expected to be around 2.5 years, with a  $^{82}\text{Se}$  source foil mass of 6109.62g \*\*\*ref internal paper\*\*\*.

This chapter is devoted to identifying the different sources of backgrounds as well as concluding how they materialise within the different parts of the detector. The  $2e$  topology cuts discussed in chapter 5 are applied to the non-DBD backgrounds in order to determine the number of double beta candidate events that originate from background decays. Additionally, the simulated data will be used to predict how background decays mimic double beta candidate events. For the three magnetic fields, the contribution of the different backgrounds to the  $0\nu\beta\beta$  sensitivity will be calculated and the most significant backgrounds will be identified. To estimate the different background contributions, they will first be divided by their location. As stated in chapter 3, the three background locations are internal, radon and external, which will first be examined separately and combined to give the total background contamination for each magnetic field configuration.

In chapter 5, the sensitivity of the best case scenario detector, with zero non double beta decaying backgrounds, was investigated. Chapter 6 introduces the non  $2\nu\beta\beta$  background contributions, integrating their contributions into the total background count, with the intention of calculating the total background contamination for the three magnetic fields, putting together all the pieces needed for the final sensitivities to be calculated in the chapter 7.

## 6.1 Background Classification and DBD Mimicking Mechanisms

### 6.1.1 Internal Background

Internal backgrounds are defined as backgrounds which originate within the confines of the source foil. The most substantial backgrounds found within the source foil are  $^{208}\text{Tl}$  and  $^{214}\text{Bi}$ , from the decay chains of  $^{232}\text{Th}$  and  $^{238}\text{U}$  respectively, as shown in figures 3.9 and 3.8.  $^{232}\text{Th}$  and  $^{238}\text{U}$  are two naturally occurring backgrounds found in small amounts within all materials. Source foils underwent processing in order to reduce the contamination of these naturally occurring radioisotopes, however a small amount of contamination still remains \*\*\* reference purification paper which is currently internal paper only\*\*\*.

The final source of internal backgrounds is the two neutrino double beta decay of the same isotope, discussed in chapter 5. At higher energies, two neutrino double beta decay is an irreducible background for  $0\nu\beta\beta$ . In the ROI,  $2\nu\beta\beta$  is indistinguishable from  $0\nu\beta\beta$  and can only be separated from the neutrinoless signal using the energy spectra of the two decays, demanding a high energy resolution. The results from  $2\nu\beta\beta$  decays were shown in the previous chapter and will be reintroduced in order to complete the total background contamination subsequently.

Both the naturally occurring backgrounds,  $^{208}\text{Tl}$  and  $^{214}\text{Bi}$ , undergo beta decay within the source foil and it is the interaction of the beta electron with the source foil that brings about events in the 2e channel as illustrated in figure 6.1. The first double beta generating mechanism is Møller scattering, which is a low angle electron-electron scattering where two electrons exchange a virtual photon transferring momentum between the two electrons. The beta electron emitted during the decay scatters an electron found within the dense source foil, resulting in the emission of two electrons from the source foil. As Møller scattering is a prompt interaction, the two electrons are emitted from the foil in parallel.

Compton scattering is the scattering of light by a charged particle, transferring momentum from the photon to the electron, ejecting the electron if the momentum transfer is sufficiently high. During beta decay, both  $^{208}\text{Tl}$  and  $^{214}\text{Bi}$  radiate photons of various energies (figures 6.2 and 6.3) which can initiate Compton scattering within the foil. The final mechanism for generating pseudo double beta events from internal backgrounds is internal conversion. Following the initial beta decay, the decaying isotope may reach an excited intermittent state during which it releases a photon for the purpose of de-excitation. Certain isotopes are able to de-excite via internal conversion, with an electron from one of the inner shells of the atom ejected from the unstable atom. The internal conversion electron can provide the second electron for the 2e topology although as a result of the de-excitation mechanism the electron emission is slower compared to prompt scattering interactions.

Although the increased density of the source foil amplifies the rate of electronic interactions, the foil also inhibits the charged particles from exiting, trapping them within the source foil or causing them to lose energy prior to emission. For this reason the source was processed into long thin sheets (foils) with the intention of minimising the energy loss for electrons prior to emission.

\*\*\* ref thickness of sf from detector chapter \*\*\*

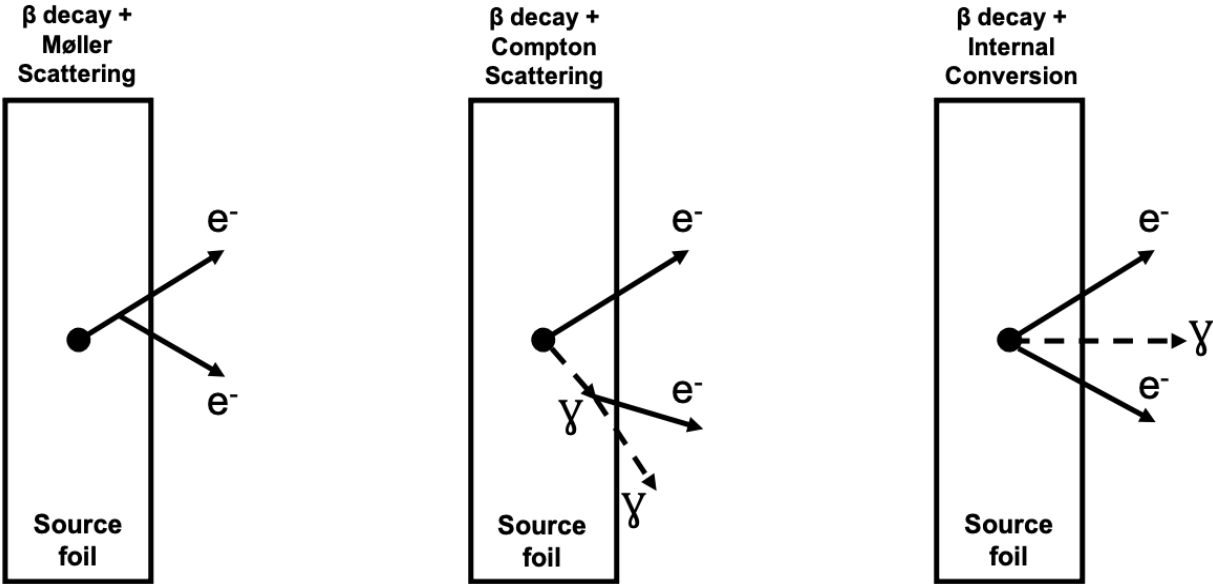


Figure 6.1: Illustrations of the dominant mechanisms, through which beta decaying internal backgrounds mimic double beta candidate events.

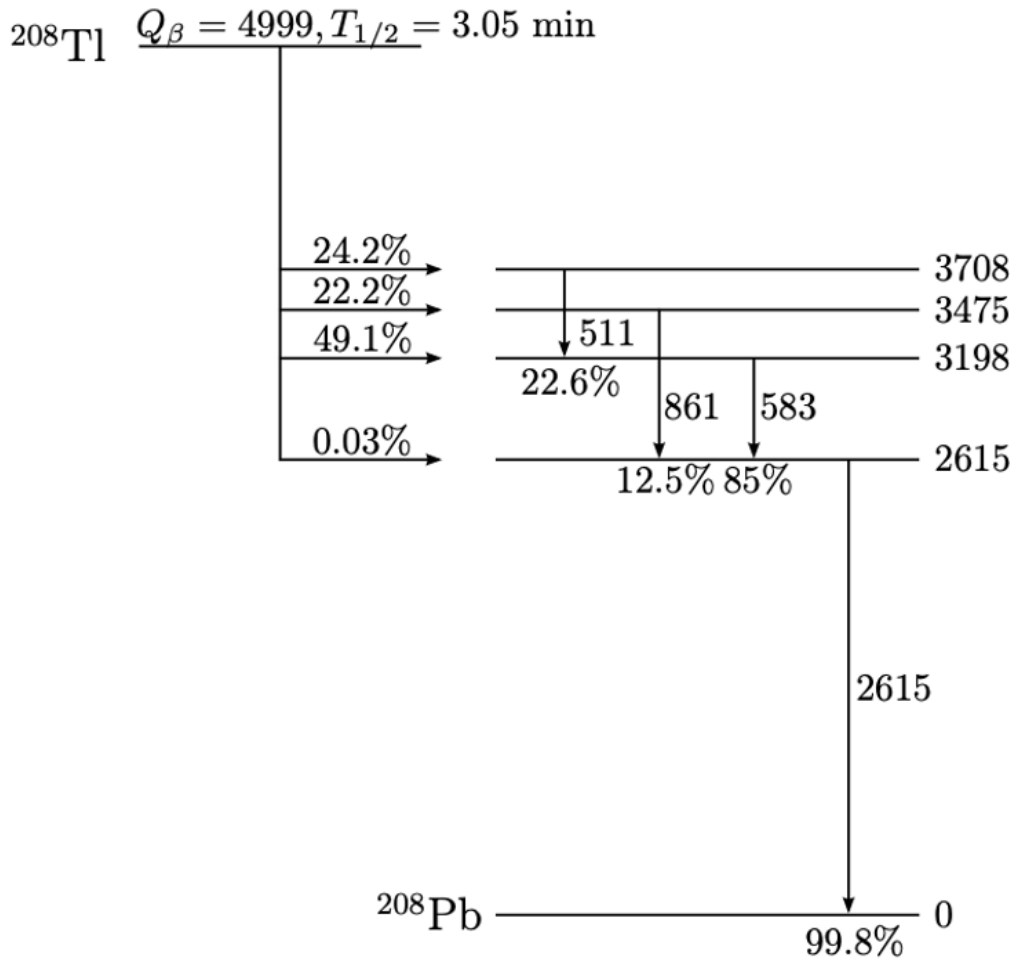


Figure 6.2: Simplified decay scheme for  $^{208}\text{Tl}$  undergoing beta decay into  $^{208}\text{Pb}$ , illustrating the most common transition lines, with the energies in keV.

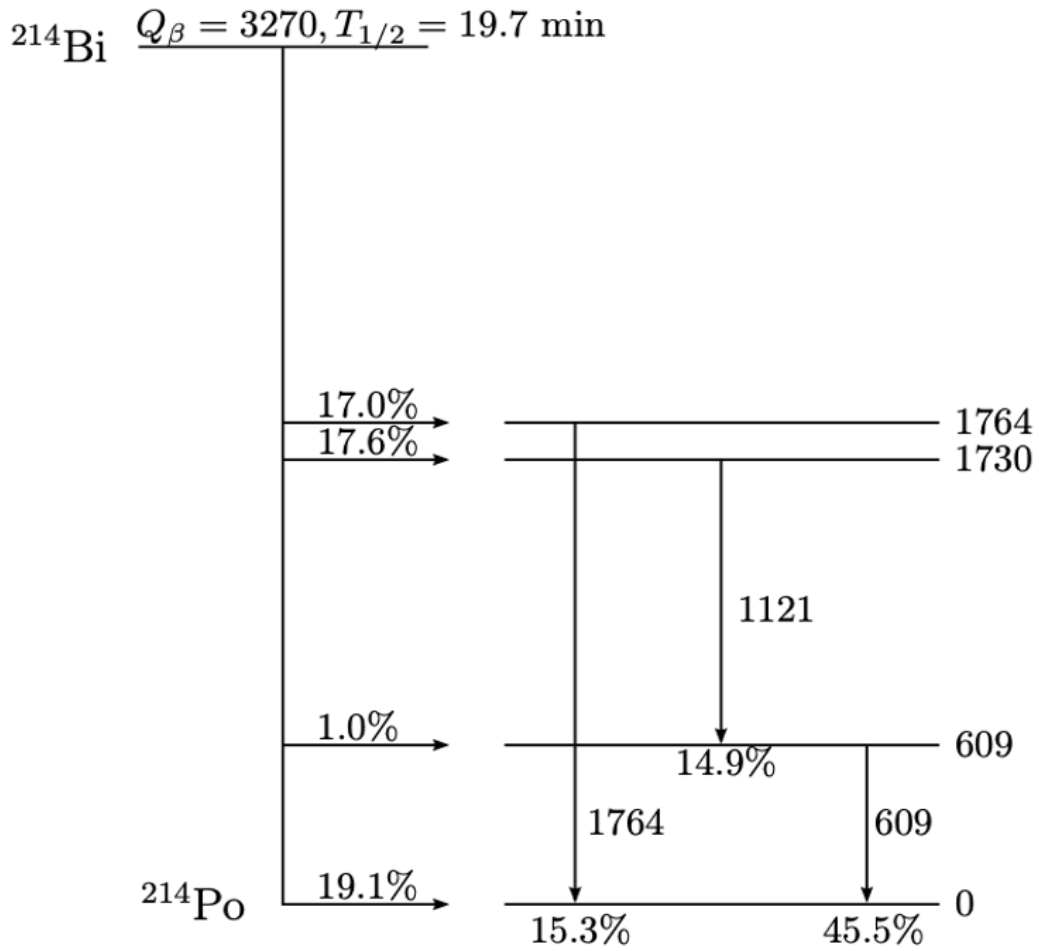


Figure 6.3: Simplified decay scheme for  $^{214}\text{Bi}$  undergoing beta decay into  $^{214}\text{Po}$ , illustrating the most common transition lines, with the energies in keV.

### 6.1.2 Radon Backgrounds

Radon is a highly diffusive gas and readily enters the tracker volume via emanation from detector components or during construction.  $^{222}\text{Rn}$  has a lifetime of roughly 3.8 days, allowing plentiful time for the gas to diffuse into the detector and undergo various decays into  $^{214}\text{Bi}$  which is deposited on the surface of the source foil and tracker wires (figure 3.8). The decay of  $^{222}\text{Rn}$  was explained in section 4.2.3, culminating in the emission of an beta electron from  $^{214}\text{Bi}$  decaying into  $^{214}\text{Po}$  and a subsequent delayed alpha from the decay of  $^{214}\text{Po}$  to  $^{210}\text{Pb}$ . Radon backgrounds interact at a much lower rate compared to the internal backgrounds as a result of the reduced density away from the source foil. The dense source foil amplifies the interaction rate of internal backgrounds as well as the Radon backgrounds on the surface of the source foil, however for decays in the tracker volume, the surrounding density is much lower.

The SuperNEMO target activity for radon in the tracker volume is  $<0.15\text{mBq/m}^3$  and to achieve this target three additional procedures were selected to reduce and control the radon level within the detector volume;

- Screening of materials to ensure only the highest radiopure materials were used
- Monitoring of the radon background levels
- Purification of the tracker gas

The most significant reduction in radon levels is achieved by flushing out the contaminated tracker gas with clean gas at a controlled rate. At a certain point, increasing the rate at which gas flows through the tracker becomes detrimental to the performance of the tracking detector and so a compromise between the performance and radon levels is met at a maximal flow rate of  $2\text{m}^3/\text{h}$  \*\*\* ref fang thesis\*\*\*.

The mechanisms for generating double beta candidate events from radon backgrounds are similar to those observed for internal backgrounds (shown in figure 6.1), with scattering being the dominant process. Unlike internal backgrounds, radon induced backgrounds originate in tracker volume (or on the surface of the source foil) resulting in a reduced interaction rate for the beta particles emitted from the background decays. The high density of the source foil increases the cross section for both photonic and electronic interactions, increasing the rate at which internal backgrounds generate additional electrons. Additionally, charged particles originating on wires in the outer layers of the tracker are unlikely to have their vertices extrapolated back to the source foil, resulting in the aforementioned DBD candidates being rejected.



### 6.1.3 External Backgrounds

External backgrounds are defined as any non-radon backgrounds originating outside of the source foil. The majority of external backgrounds come about as a result of decays within the detector components, radioactive decays in the rocks surrounding the laboratory and neutron capture. External backgrounds materialise in a variety of decay channels including  $1eN\gamma$ , however it is possible for external backgrounds to bring about double beta like decays reconstructed from the source foil.

An array of mechanisms can result in the production of double beta candidate events from external backgrounds. Unlike internal backgrounds which mimic double beta decay via mostly low angle scattering, external backgrounds primarily generate pseudo double beta decays by way of photonic interactions with the dense source foil and other detector components. Pair production and Compton scattering from external photons provide the two principal mechanisms by which external backgrounds contribute towards the double beta decay channel.

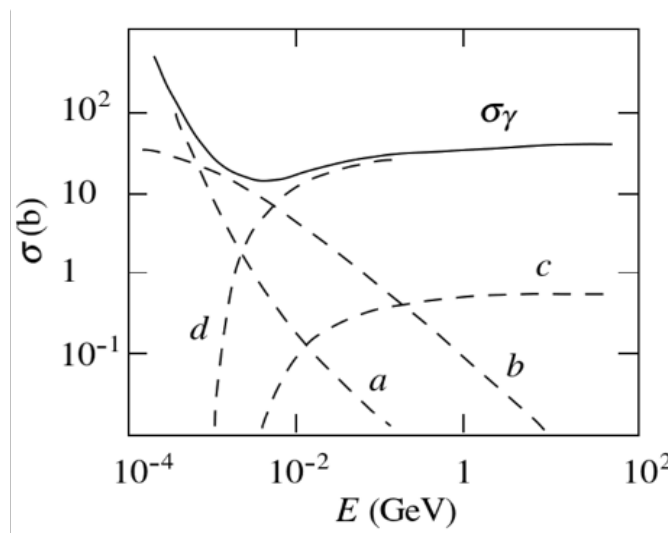


Figure 6.4: A

For external backgrounds, the mechanisms for producing two electron topologies more often involve photonic interactions (figure 6.5 as opposed to the internal and radon backgrounds which mostly produce two electrons via beta decay plus low angle electronic scattering. Multi energy photons from external decays first interact with the source foil, producing an electron positron pair or a single Compton electron. The electron can then Møller scatter to eject a second electron from the source foil. Additionally, the incident photon can directly beget two electrons via double Compton scattering as the photon pass through the foil. Pair production requires a photon of energy greater than 1.022 MeV to interact with dense source material and produce an electron positron pair. The minimum energy threshold of 1.022 MeV, represents twice the rest mass energy of an electron, so it is impossible for lower energy photons to pair produce. Both  $^{208}\text{Tl}$  and  $^{214}\text{Bi}$  beta decays produce high energy ( $>1.022$  MeV) photons capable of pair producing as shown by the decay

schemes in figures 6.2 and 6.3.  $^{208}\text{Tl}$  in particular, produces a 2.615 MeV photon at a rate of 99.8%. The electron positron pair emitted from the source foil, can be misconstrued as a two electron event if the positron is labelled as an electron. For no field this is particularly troublesome, as the absence of magnetic flux within the tracker volume results in straight tracks that cannot be differentiated by charge. At lower energies, the likelihood of Compton scattering and the photoelectric effect increases, although from the decay schemes shown in figures 6.2 and 6.3, Compton scattering and pair production are the likely processes associated with externally induced double beta candidate events.

In addition to the contributions from external  $^{208}\text{Tl}$  and  $^{214}\text{Bi}$ ,  $^{40}\text{K}$  is an additional relevant external background as mentioned in chapter \*\*\*ref background.  $^{40}\text{K}$  can undergo both beta decay and electron capture resulting in the emission of a single electron or an electron followed by a photon after electron capture. Nonetheless, the decay energy of  $^{40}\text{K}$  is significantly lower than both  $^{208}\text{Tl}$  and  $^{214}\text{Bi}$ , at approximately 1.4 MeV \*\*\* confirm, reducing the rate at which  $^{40}\text{K}$  decays mimic double beta candidate events, particularly in the high energy ROI.

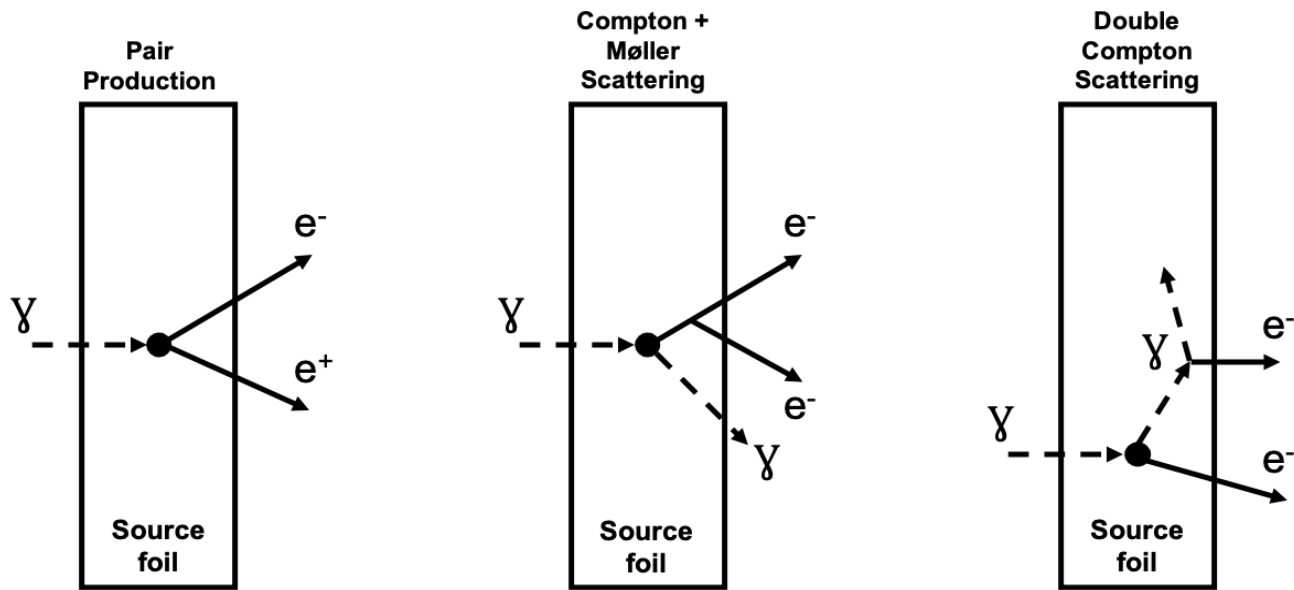


Figure 6.5: Illustrations of the dominant mechanisms, through which external backgrounds interacting with the source foil mimic double beta candidate events.

## 6.2 Background Activities

### 6.2.1 Table of Activities

Isotope	Location	Activity mBq	No of Decays From Nominal Exposure
$2\nu\beta\beta$	Source Foil Bulk	X	X
$^{208}\text{Tl}$	Source Foil Bulk	0.55 *	43,000
$^{214}\text{Bi}$	Source Foil Bulk	4.94 *	389,500
$^{208}\text{Tl}$	Tracker Wire Bulk	$0.24 \pm 0.05$	18,900
$^{214}\text{Bi}$	Source Foil Surface	$0.33 \pm 0.04$	26,000
$^{214}\text{Bi}$	Tracker Wire Bulk	$0.49 \pm 0.10$	38,600
$^{214}\text{Bi}$	Tracker Wire Surface	$3.92 \pm 0.44$	309,000
$^{40}\text{K}$	8" Main Wall PMT Glass Bulb	$230 \pm 23$	18,133,200,000
$^{40}\text{K}$	5" Main Wall PMT Glass Bulb	$23 \pm 2.3$	1,813,320,000
$^{40}\text{K}$	X Wall PMT Glass Bulb	$37 \pm 3.7$	2,917,080,000
$^{40}\text{K}$	G Veto Wall PMT Glass Bulb	$19 \pm 1.9$	1,497,960,000
$^{208}\text{Tl}$	8" Main Wall PMT Glass Bulb	$41 \pm 4.1$	3,232,440,000
$^{208}\text{Tl}$	5" Main Wall PMT Glass Bulb	$1 \pm 0.1$	78,840,000
$^{208}\text{Tl}$	X Wall PMT Glass Bulb	$2 \pm 0.2$	157,680,000
$^{208}\text{Tl}$	G Veto Wall PMT Glass Bulb	$1 \pm 0.1$	78,840,000
$^{214}\text{Bi}$	8" Main Wall PMT Glass Bulb	$136 \pm 13.6$	10,722,240,000
$^{214}\text{Bi}$	5" Main Wall PMT Glass Bulb	$18 \pm 1.8$	1,419,120,000
$^{214}\text{Bi}$	X Wall PMT Glass Bulb	$30 \pm 3.0$	2,365,200,000
$^{214}\text{Bi}$	G Veto Wall PMT Glass Bulb	$15 \pm 1.5$	1,182,600,000

Table 6: Total activities for all backgrounds simulated with an internal, radon and external vertex. The activity (mBq) for each isotope is given alongside the expected exposure of 6.25 Kg over 2.5 years of running time. For internal  $^{208}\text{Tl}$  and  $^{214}\text{Bi}$  the activities are provided as an upper limit. For the external backgrounds the listed activities are given in Bq.

All external backgrounds have a total error of 10% \*\*\*ref Ferederic \*\*\*

The internal background activities within the source foil were measured throughout the volume of the detector and this contamination level was noted at multiple intervals. For  $^{214}\text{Bi}$ , the activity is given as a maximum limit from a BiPo measurement, with a 90% confidence. The target activity for  $^{214}\text{Bi}$  is  $10\mu\text{Bq/Kg}$  and  $2\mu\text{Bq/Kg}$  for  $^{208}\text{Tl}$ .

Radon in the tracker provides the contamination level for  $^{214}\text{Bi}$  on both the surface of the source foil as well as the tracker wires. The most accurate prediction states that approximately 7.8% of the radon contamination in the tracker deposits onto the surface of the tracker wires and the remaining 92.2% on the source foil surface. The division of activity is based on the width of the tracker-source air gap and the width of the tracker *\*\*ref docdb papaer\*\*\**. As mentioned earlier in the chapter, the radon activity is given as a function of the flushing rate, which is expected to be  $1\text{m}^3/\text{h}$ . The tracker wire bulk activity was directly measured alongside the anode wire bulk, however anode wire events were not simulated so the activity data is not included.

## 6.3 Background Simulations

### 6.3.1 Table of Simulations

Vertex Location	$^{40}\text{K}$	$^{208}\text{Tl}$	$^{214}\text{Bi}$	$2\nu\beta\beta$	Number of Simulations on Vertex
Source Foil Bulk		✓	✓	✓	$10^8$
Source Foil Surface		✓	✓		$10^8$
Tracker Wire Bulk		✓	✓		$10^8$
Tracker Wire Surface		✓	✓		$10^8$
8" Main Wall PMTs*	✓	✓	✓		$1.1 \times 10^{9\dagger}$
5" Main Wall PMTs	✓	✓	✓		$10^9$
X Wall PMTs	✓	✓	✓		$10^9$
G Veto Wall PMTs	✓	✓	✓		$10^9$

Table 7: Simulation vertex locations and the isotopes simulated at those locations

<sup>†</sup> For the external  $^{208}\text{Tl}$  simulations, 15 billion events were simulated for no field and 11 Billion events for the remaining two magnetic fields.

All simulations were generated using Falaise 4.0.0 detailed in chapter 4. Simulated events were then reconstructed using the official Falaise 4.0.0 reconstruction configuration. For each isotope simulated at a vertex location, the number of simulations were generated for all three magnetic field configurations. In addition, although the tracker wire bulk activity is not derived from the radon contamination in the tracker volume, backgrounds in the tracker wires closely resemble those observed with other radon backgrounds and so it is included within the radon backgrounds.

## 6.4 Background Results

### 6.4.1 Internal Backgrounds

Cut Descriptions	Magnetic Field Configuration		
	Uniform Field	No Field	Realistic Field
Only two calorimeter hits above 50keV, at least one >150keV	0.2387	0.2342	0.2349
Two tracker clusters with 3 or more cells	0.0311	0.0239	0.0253
Two reconstructed tracks	0.0309	0.0238	0.0251
Remove events with multiple hits to the same calorimeter	0.0134	0.0119	0.0122
Each track associated to a calorimeter	0.0017	0.0024	0.0022
Two vertices on the source foil	0.0016	0.0023	0.0022
Vertex $\Delta R < 1\text{cm}$ and $\Delta Z < 3\text{cm}$ (separation between vertices)	0.0008	0.0012	0.0011
Internal Probability >1% and External Probability <4%	0.0007	0.0010	0.0009
Delayed Alpha Hits (no hits allowed after 13 $\mu\text{s}$ )	0.0007	0.0010	0.0009
Remove Positrons (unavailable for no field)	0.0006	-	0.0006
Energy Cut (between 2.8 and 3.2 MeV)	$1907 \times 10^{-8}$	$2527 \times 10^{-8}$	$1637 \times 10^{-8}$
Number of Expected Events	0.82 $\pm 0.02$ (stat)	1.09 $\pm 0.02$ (stat)	0.69 $\pm 0.02$ (stat)

Table 8: Internal  $^{208}\text{Tl}$  cut flow for the three magnetic field configurations. Each row lists a short description of the cut as well as the concurrent detection efficiency.

As defined in section 6.1, internal backgrounds are those which originate from within the bulk of the source foil. For SuperNEMO, this includes the  $2\nu\beta\beta$  contribution discussed in the previous chapter as well as  $^{208}\text{Tl}$  and  $^{214}\text{Bi}$ . The number of internal simulations generated for each magnetic field is shown in table 7. Following simulation and reconstruction, the two electron cut flows and number of expected events are shown for  $^{208}\text{Tl}$  and  $^{214}\text{Bi}$  in tables 8 and 9 respectively.

From table 8, the final detection efficiency and consequently the magnetic field with the greatest

number of expected events is the no field scenario, followed by the uniform and realistic fields respectively. The most significant reason for this is the impact of the charge cut on reducing the uniform and realistic field, specifically the realistic field, whereas for no field the cut is not applied. The reduced field strength of the realistic field reduces the overall radius of curvature for realistic field events, decreasing the rate at which electron tracks are successfully reconstructed. Straighter charged particle tracks are more likely to be reconstructed as positrons increasing the number of events removed by the charge cut for the realistic field. Prior to the associated tracks cut, the uniform field has the greatest detection efficiency, as the increased track radius of curvature increases the number of reconstructed tracks. For  $0/2\nu\beta\beta$ , the increased rate of track fitting for the uniform field resulted in an increased number of events with three or more reconstructed tracks, as the two double beta electrons generated three electron tracks. However, for the single beta decaying backgrounds, the poor track fitting procedure increases the number of tracks from one to two and the photon provides a second calorimeter hit, resulting in an increased initial detection efficiency for the uniform field. After applying the remaining cuts however, the difference in detection efficiency between the uniform field and the other two fields is reduced as these events are identified and removed by other cuts.

Cut Descriptions	Magnetic Field Configuration		
	Uniform Field	No Field	Realistic Field
Only two calorimeter hits above 50keV, at least one >150keV	0.2375	0.2392	0.2389
Two tracker clusters with 3 or more cells	0.0315	0.0261	0.0271
Two reconstructed tracks	0.0303	0.0251	0.0260
Remove events with multiple hits to the same calorimeter	0.0157	0.0148	0.0150
Each track associated to a calorimeter	0.0032	0.0042	0.0040
Two vertices on the source foil	0.0028	0.0036	0.0035
Vertex $\Delta R < 1\text{cm}$ and $\Delta Z < 3\text{cm}$ (separation between vertices)	0.0013	0.0017	0.0017
Internal Probability >1% and External Probability <4%	0.0012	0.0016	0.0015
Delayed Alpha Hits (no hits allowed after 13 $\mu\text{s}$ )	0.0012	0.0016	0.0015
Remove Positrons (unavailable for no field)	0.0011	-	0.0010
Energy Cut (between 2.8 and 3.2 MeV)	$362 \times 10^{-8}$	$477 \times 10^{-8}$	$315 \times 10^{-8}$
Number of Expected Events	1.41 $\pm 0.07$ (stat)	1.86 $\pm 0.09$ (stat)	1.23 $\pm 0.92$ (stat)

Table 9: Internal  $^{214}\text{Bi}$  cut flow for the three magnetic field configurations. Each row lists a short description of the cut as well as the concurrent detection efficiency.

The detection efficiency of  $^{214}\text{Bi}$  is inferior to  $^{208}\text{Tl}$ , however, as a result of the greater  $^{214}\text{Bi}$  activity in the source foil (table 6), the number of expected backgrounds from  $^{214}\text{Bi}$  is higher. On average, the detection efficiency of internal  $^{208}\text{Tl}$  is around  $5\times$  greater compared to  $^{214}\text{Bi}$ , but after normalising to the activity, the number of expected events is roughly  $1.7\times$  greater for  $^{214}\text{Bi}$ . From figure 6.6, the reduced detection efficiency of  $^{214}\text{Bi}$  can be explained from tail of the energy spectrum, which falls to zero within the region of interest, akin to  $2\nu\beta\beta$ . For internal  $^{208}\text{Tl}$ , the energy spectrum extends well beyond the  $^{82}\text{Se}$  ROI, increasing the total number of two electron events found within the region.

The results for  $2\nu\beta\beta$  were discussed in chapter 5 which completes the internal background



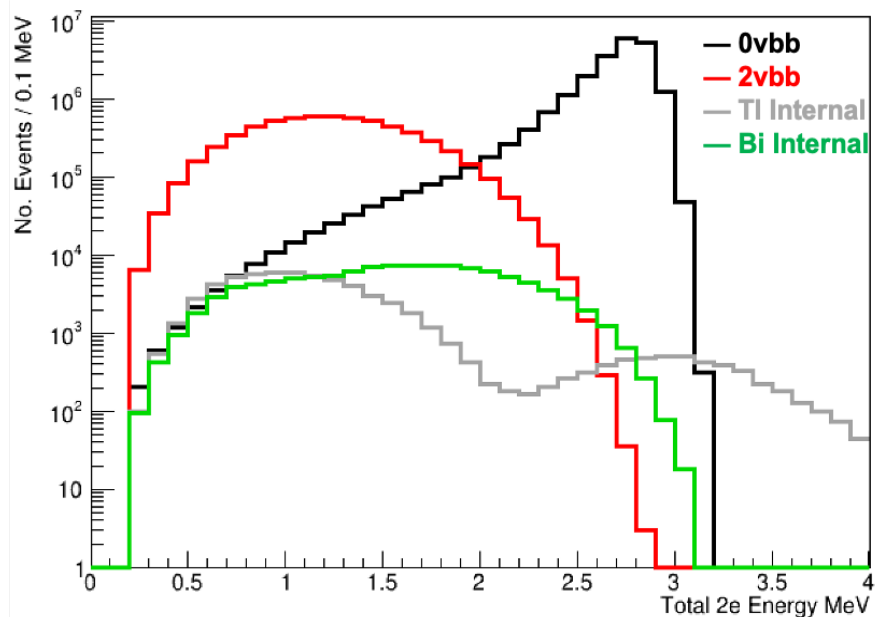


Figure 6.6: InternalSpectrum

contributions. The number of expected events from  $2\nu\beta\beta$  is shown in table 10, alongside the results from internal  $^{208}\text{Tl}$  and  $^{214}\text{Bi}$ . The total internal background count for each magnetic field configuration is also provided.

Internal Background	Number of Expected Events		
	Uniform Field	No Field	Realistic Field
$2\nu\beta\beta$	$0.15 \pm 0.09$ (stat)	$0.10 \pm 0.07$ (stat)	$0.05 \pm 0.05$ (stat)
$^{208}\text{Tl}$	$0.82 \pm 0.02$ (stat)	$1.09 \pm 0.02$ (stat)	$0.69 \pm 0.02$ (stat)
$^{214}\text{Bi}$	$1.41 \pm 0.07$ (stat)	$1.86 \pm 0.09$ (stat)	$1.23 \pm 0.92$ (stat)
Total	$2.38 \pm$ (stat)	$3.05 \pm$ (stat)	$1.97 \pm$ (stat)

Table 10: Number of expected events for all internal backgrounds for the three magnetic field configurations. The activities used to calculate the number of expected events are upper limits and so no systematic error is given.

Of the three backgrounds,  $^{214}\text{Bi}$  has the greatest number of expected events followed by  $^{208}\text{Tl}$  and  $2\nu\beta\beta$ . As a result of the low  $2\nu\beta\beta$  detection efficiency, the number of expected events is much lower compared to the other internal backgrounds whilst also having a high statistic uncertainty. Overall, the internal background contamination is highest for no field, followed by the uniform field and realistic field respectively.

## 6.4.2 Radon Backgrounds

Isotope	Location	Detection Efficiency ( $\times 10^{-8}$ ) & Number of Expected Events		
		Uniform Field	No Field	Realistic Field
$^{208}\text{Tl}$	Tracker Wire Bulk	30	53	34
		$0.006 \pm 0.001$ (stat) $\pm 0.002$ (syst)	$0.010 \pm 0.001$ (stat) $\pm 0.004$ (syst)	$0.006 \pm 0.001$ (stat) $\pm 0.002$ (syst)
$^{214}\text{Bi}$	Source Foil Surface	314	373	247
		$0.08 \pm 0.004$ (stat) $\pm 0.009$ (syst)	$0.10 \pm 0.005$ (stat) $\pm 0.011$ (syst)	$0.06 \pm 0.004$ (stat) $\pm 0.007$ (syst)
$^{214}\text{Bi}$	Tracker Wire Bulk	9	9	6
		$0.003 \pm 0.001$ (stat) $\pm 0.001$ (syst)	$0.003 \pm 0.001$ (stat) $\pm 0.001$ (syst)	$0.002 \pm 0.001$ (stat) $\pm 0.001$ (syst)
$^{214}\text{Bi}$	Tracker Wire Surface	6	9	6
		$0.019 \pm 0.008$ (stat) $\pm 0.002$ (syst)	$0.028 \pm 0.009$ (stat) $\pm 0.003$ (syst)	$0.019 \pm 0.008$ (stat) $\pm 0.002$ (syst)

Table 11: Detection efficiency of all radon simulations for the three magnetic field configurations.

Radon backgrounds contribute significantly fewer expected events to the  $^{82}\text{Se}$  ROI compared to those from the internal sources. For  $^{208}\text{Tl}$  in the bulk of the tracker wires, both the detection efficiency and activity are lower than the corresponding internal background, resulting in the  $^{208}\text{Tl}$  radon contribution being roughly 1% of the total internal  $^{208}\text{Tl}$  expected events.

For  $^{214}\text{Bi}$ , there are three sources of radon backgrounds, including the surface of the source foil,

tracker wire bulk and tracker wire surface. The combined contribution from the three radon sources is dwarfed by internal  $^{214}\text{Bi}$ , accounting for only 7% of the internal contribution. Primarily this is a consequence of the lower  $^{214}\text{Bi}$  activity on the surface of the source foil and the low detection efficiency of the tracker wire simulations. The detection efficiency of  $^{214}\text{Bi}$  on the source foil surface is similar to that observed with  $^{214}\text{Bi}$  inside of the source foil however, as the activity is an order of magnitude lower the number of expected events is similarly reduced. The detection efficiencies for  $^{214}\text{Bi}$  on the surface and within the bulk of the tracker wires are significantly lower than that seen for  $^{214}\text{Bi}$  on the source foil surface because the event vertices are less likely to be reconstructed back to the foil.

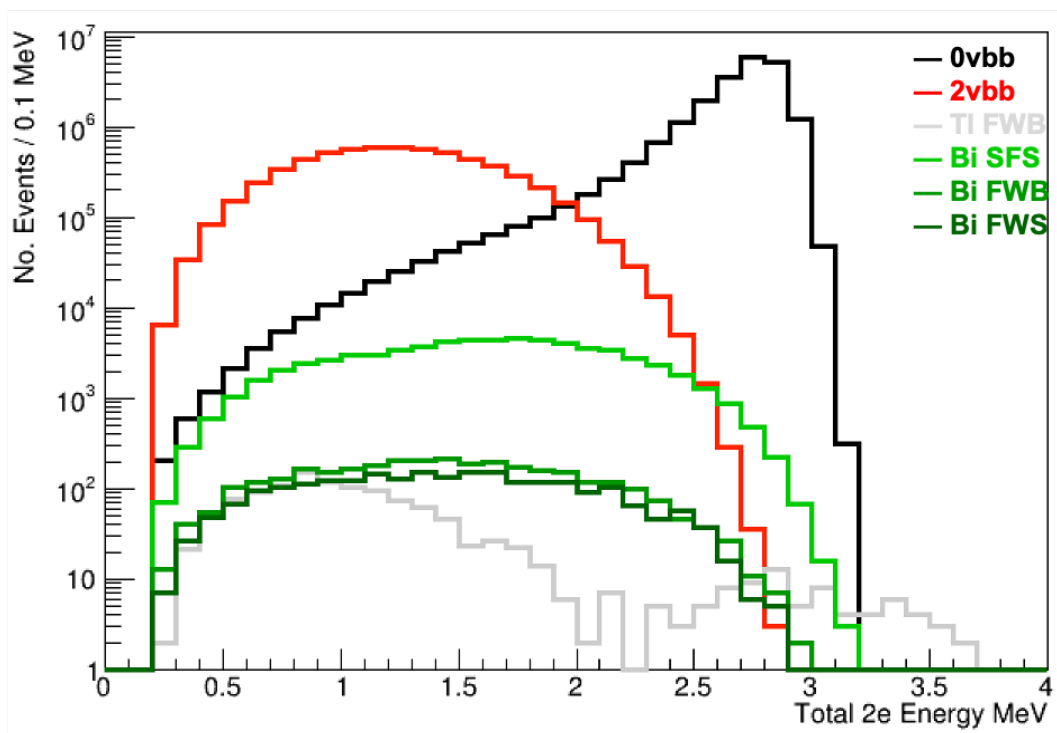


Figure 6.7: 0

Like internal  $^{214}\text{Bi}$ , the radon  $^{214}\text{Bi}$  energy spectra curtail within the  $^{82}\text{Se}$  ROI, reducing the detection efficiency compared to  $^{208}\text{Tl}$ . Additionally, the energy profile for  $^{214}\text{Bi}$  on the surface of the source foil is extremely similar to the internal  $^{214}\text{Bi}$  spectra.

### 6.4.3 External Backgrounds

Isotope	Location	Detection Efficiency & Number of Expected Events		
		Uniform Field	No Field	Realistic Field
$^{208}\text{Tl}$	8" Main Wall PMTs	$\frac{2^*}{1.1 \times 10^{10}}$	$\frac{110^\dagger}{1.5 \times 10^{10}}$	$\frac{10^*}{1.1 \times 10^{10}}$
		$0.58 \pm 0.41$ (stat) $\pm 0.06$ (syst)	$23.5 \pm 2.24$ (stat) $\pm 2.35$ (syst)	$2.91 \pm 0.92$ (stat) $\pm 0.29$ (syst)

Table 12: Number of simulations and expected events for external  $^{208}\text{Tl}$  on the 8" Main wall PMTs for the three magnetic field configurations.

From  $^\dagger 15$  billion and  $^* 11$  billion simulated events.

From the external PMTs, the sole background contribution to the  $^{82}\text{ROI}$  came from  $^{208}\text{Tl}$  on the 8" Main wall PMTs. No Monte Carlo simulated events were found in the ROI for any of the other isotopes simulated in all of the external locations. As a result of the non-zero contribution from external  $^{208}\text{Tl}$  on the 8" Main wall PMTs, an increased number of events were simulated (from the original  $10^9$ ) in order to reduce the statistical uncertainty on the simulated data. For no field, including the additional secondary particle simulations, a total of 15 billion events were simulated, whereas for the uniform and realistic fields, 11 billion decays were simulated, with no secondary particle simulations.

Following simulation and normalization to both the exposure as well as the number of simulated events, the cut flow detection efficiency and total number of expected events for  $^{208}\text{Tl}$  on the 8" Main wall PMT glass bulb is shown in table 12. The number of expected events of 23.5 for no field represents almost 90% of the total backgrounds for the no field scenario. Although the detection efficiency is much lower for external  $^{208}\text{Tl}$ , the much greater activity from external sources (table 6) results in an increased number of expected backgrounds compared to other background sources. Similarly, for the realistic field, external  $^{208}\text{Tl}$  is the largest background however it only represents approximately 60% of the total activity. For the uniform field external  $^{208}\text{Tl}$  is the third largest background contribution behind internal  $^{208}\text{Tl}$  and internal  $^{214}\text{Bi}$ . The extremely large contribution from external  $^{208}\text{Tl}$ , particularly for no field and the realistic field requires further multi variate analysis in order to create additional, targeted cuts for reducing this particular background. In the following chapter, the underlying mechanism producing the background will be discussed and used to rationalize the extra cuts and finally the impact of these cuts will be exhibited.

The energy spectra for the four simulated sources of external  $^{208}\text{Tl}$  are shown in figure 6.8 alongside the energy spectra for 0 and  $2\nu\beta\beta$ . The remaining three external  $^{208}\text{Tl}$  vertex locations

lead to the generation of double beta candidate events however no such events has energy greater than 2.5 MeV.

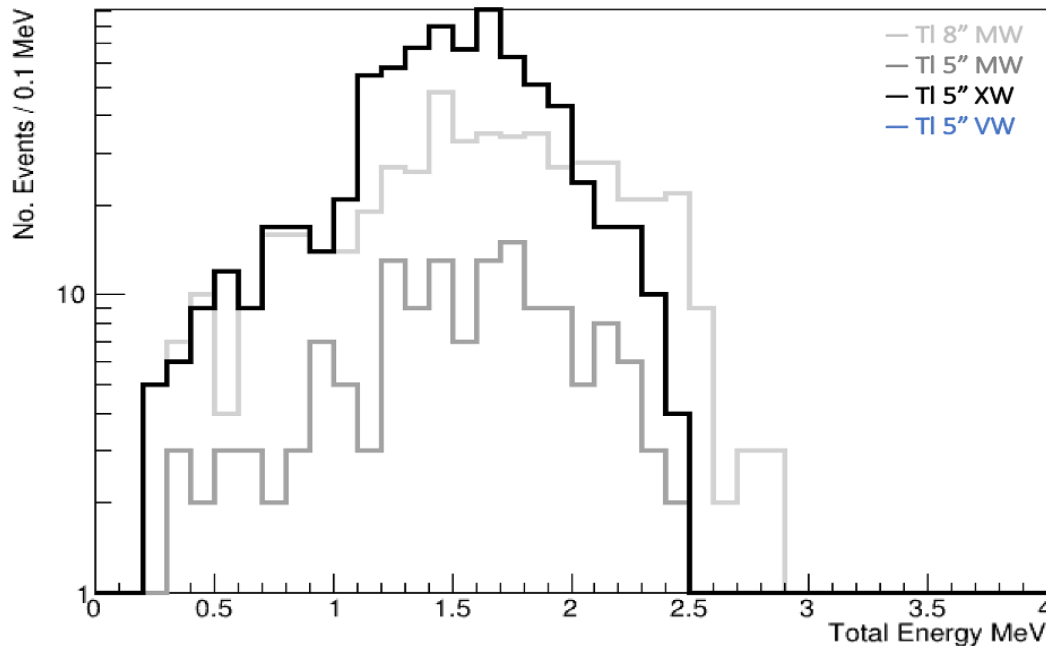


Figure 6.8: Energy spectra of all external  $^{208}\text{Tl}$  double beta candidate events.

There were no background contributions from any of the isotopes simulated on the 8" Main Wall, 5" Main wall, X wall and Veto wall PMT glass bulbs. Backgrounds from the two rows of 5" Main wall PMTs, located at the top and bottom of the Main walls, are encumbered by their location, reducing the number of external backgrounds reaching the source foil. A similar but more severe impact is observed for the G Veto simulations with no double beta candidate events of any energy being generated. Although the X wall events are less suppressed by their location within the detector, the double beta candidate events have energies outside the region of interest.

The energy spectra of the three isotopes simulated on the 8" Main wall PMTs is shown in figure 6.9, with only the  $^{208}\text{Tl}$  tail surpassing 2.8 MeV. The lower energy decays of  $^{40}\text{K}$  and  $^{214}\text{Bi}$  results in the potential double beta candidate events to be removed by the 2.8 - 3.2 MeV energy cut. Additionally, the low energy spectra shown in figure 6.9 indicate no double beta candidate events would be found from simulating on the X and G Veto walls and so no events were simulated. The Main wall represents the most probable external vertex location for inducing two electron events and so it is not expected for either external  $^{40}\text{K}$  or  $^{214}\text{Bi}$  to contribute to the  $^{82}\text{Se}$  ROI.

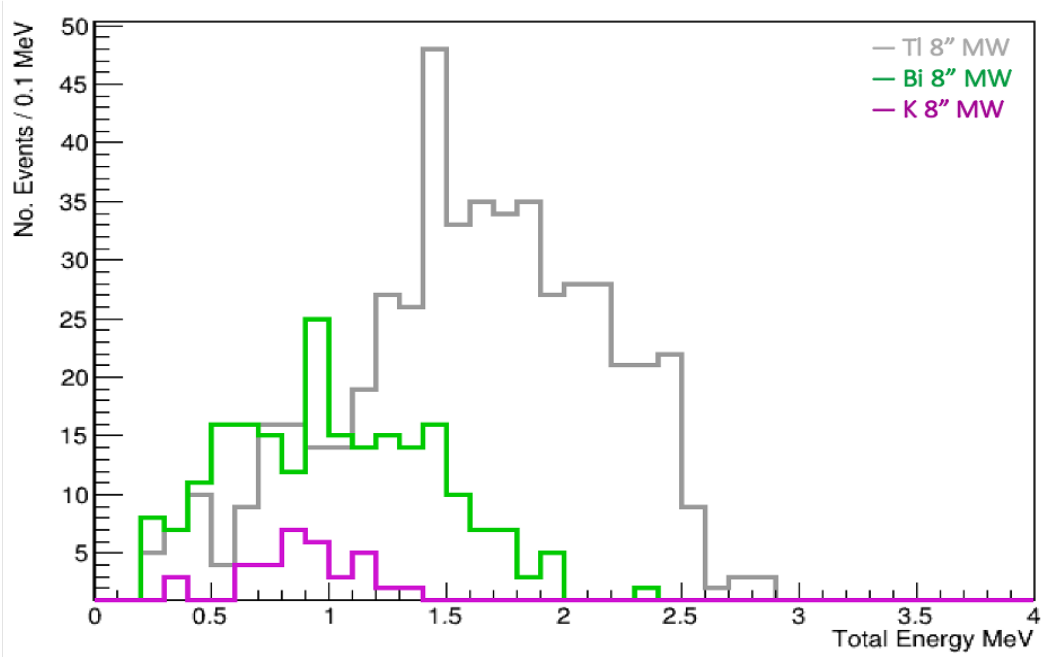


Figure 6.9: Energy spectra of all 8" Main wall backgrounds for no field. 1 billion

## 6.4.4 Total Background Contributions

Background	Number of Expected Events/ $10^8$ MC Simulations		
	Uniform Field	No Field	Realistic Field
Internal $^{208}\text{Tl}$	0.82	1.09	0.69
Internal $^{214}\text{Bi}$	1.41	1.86	1.23
Radon $^{208}\text{Tl}$	0.006	0.010	0.006
Radon $^{214}\text{Bi}$	0.104	0.128	0.086
*External $^{208}\text{Tl}$ 8" Main Wall PMTs	0.58	23.5	2.91
Total Number of Expected Events	2.92	26.5	4.92

Table 13: Number of expected events of the different background isotopes and their locations within the detector. The total number of expected backgrounds for all three magnetic fields is also provided.

Table 13 gives the total number of expected events for each isotope that contributes a non-zero amount to the  $^{82}\text{Se}$  region of interest. Of the three magnetic field configurations, no field has the greatest number of expected backgrounds, roughly 5x greater than the realistic field and close to 9x the uniform field. The discrepancy between the three fields is largely a result of the contribution from external  $^{208}\text{Tl}$  on the 8" Main Wall PMTs which contributes significantly more for no field. Overall, the number of expected events from each background is highest for no field, largely as a result of the increased rate of associated calorimeter hits for charged particle tracks but also the inability to cut particles based on their charge.

For the realistic field, the number of expected events from each background source is the lowest amongst the three fields except for external  $^{208}\text{Tl}$ , which increases the total backgrounds for the realistic field to be greater than the uniform field. From the cut flows in tables 8 and 9, the detection efficiency of double beta candidate events is greater for the realistic field until the charge and energy cuts are applied at which the lower magnetic field strength of the realistic field reduces the efficiency at which electrons charges are accurately reconstructed therefore reducing the number of possible double beta candidate events.

Additionally, the increased contribution from external  $^{208}\text{Tl}$  is a result of the incredibly high activity of the external backgrounds as the detection efficiencies of the external backgrounds are generally much lower compared to the internal or radon simulations. By identifying the mechanism behind the external  $^{208}\text{Tl}$  it may be possible to target and remove the small number of reconstructed

events that result in the large background contribution. At the same time it may also be possible to reduce the other backgrounds, in particular, internal  $^{208}\text{Tl}$  and  $^{214}\text{Bi}$ , however it should not come at the cost of significantly reducing the signal detection efficiencies shown in the previous chapter, in order to maintain a high sensitivity to  $^{82}\text{Se}$  neutrinoless double beta decay.

\*\*\*\*\* may want to incorporate \*\*\*\*

#### 6.4.5 $e\gamma$ Channels

The  $1e2\gamma$  channel is the main background channel for measuring the contamination of  $^{208}\text{Tl}$ . The  $1e2\gamma$  channel contains events with a single electron accompanied by two photons. The isotopic photon flux shown in figure ?? provides the chief photon energies and fluxes for the three external backgrounds. For  $^{208}\text{Tl}$ , the majority of the decays (99.8%) result in the emission of a high energy 2.6 MeV photon which is often emitted alongside a number of lower energy photons. The decay scheme of  $^{208}\text{Tl}$  is complicated (figure 6.2) and can result in more than two photons being emitted from the decay, however the most populated background channel is the  $1e2\gamma$  channel. Similarly,  $^{214}\text{Bi}$  decays can result in the emission of multiple photons although the addition of the delayed alpha in  $^{214}\text{Bi}$  beta decay allows for it to be measured in the  $1e1\alpha$  decay that will be discussed in the following section.


By setting a high minimum energy the channel can be further optimised to measure  $^{208}\text{Tl}$ , removing some of the lower energy backgrounds from  $^{40}\text{K}$  and  $^{214}\text{Bi}$  which also contribute to the  $1e2\gamma$  channel.



# Chapter 7

## Sensitivity And Optimization

From the previous chapter it was shown that the major background contributions came from internal  $^{208}\text{Tl}$  /  $^{214}\text{Bi}$  as well as external  $^{208}\text{Tl}$  on the 8" Main wall PMTs. Of the three magnetic field configurations being investigated, the no field scenario had the highest detection efficiency for reconstructing two electron events from all backgrounds. Consequently, the no field scenario had the greatest number of expected backgrounds, followed by the realistic and uniform field (table 13). Furthermore, the discrepancy in the number of expected backgrounds between no field and the other two magnetic fields was found to be extremely stark, with the number of expected events for no field being 5 and 9 times greater than the realistic and uniform field respectively. The primary reason for this was the greater detection efficiency of external  $^{208}\text{Tl}$  with no magnetic field. Additionally, in chapter 5, the detection efficiency of  $0\nu\beta\beta$  was shown to be highest for no field, followed by the uniform and realistic field. However, the difference in detection efficiency of  $0\nu\beta\beta$  across the three magnetic fields was much lower compared to the expected backgrounds.

In order to measure the performance of three magnetic field configurations, the sensitivity to  $^{82}\text{Se}$  neutrinoless double beta decay is calculated for each magnetic field and the magnetic field with the highest sensitivity is likely to provide the best performance during the detectors operational lifetime. The sensitivity is dependant upon multiple factors, including the  $0\nu\beta\beta$  detection efficiency and number of expected backgrounds discussed in the previous chapters. To maximize sensitivity, the  $0\nu\beta\beta$  detection efficiency should be as large as possible whilst simultaneously suppressing the background count. During this chapter, additional optimization cuts will be rationalised using the underlying mechanism generating the 2e events from external  $^{208}\text{Tl}$ . The impact of the additional optimization cuts on both the background contamination and signal efficiency will be presented. Subsequently, the current 2.8 - 3.2 MeV ROI will be optimised to minimise background and maximise the signal and finally the sensitivities of the three magnetic field scenarios will be approximated, using both Gaussian and Poissonian methods, with a view to determine which of the three magnetic field scenarios provides the greatest  $0\nu\beta\beta$  sensitivity. 

### 7.0.1 External Background Mechanism for DBD Candidates

The initial beta decay of  $^{208}\text{Tl}$  on the PMT glass bulbs results in the emission of an electron, as well as a number of gammas dictated by the decay scheme in figure 6.2. However, after generating additional simulations with true secondary particle information, the two reconstructed electron tracks were brought about by a single secondary electron emitted from the initial PMT. The single electron generates two reconstructed tracks by propagating from the primary PMT, to the source foil and backscattering off the foil before finally coming to rest in a second calorimeter close to the initial decay. This results in two reconstructed charged particles that appear to have a shared vertex on the foil.

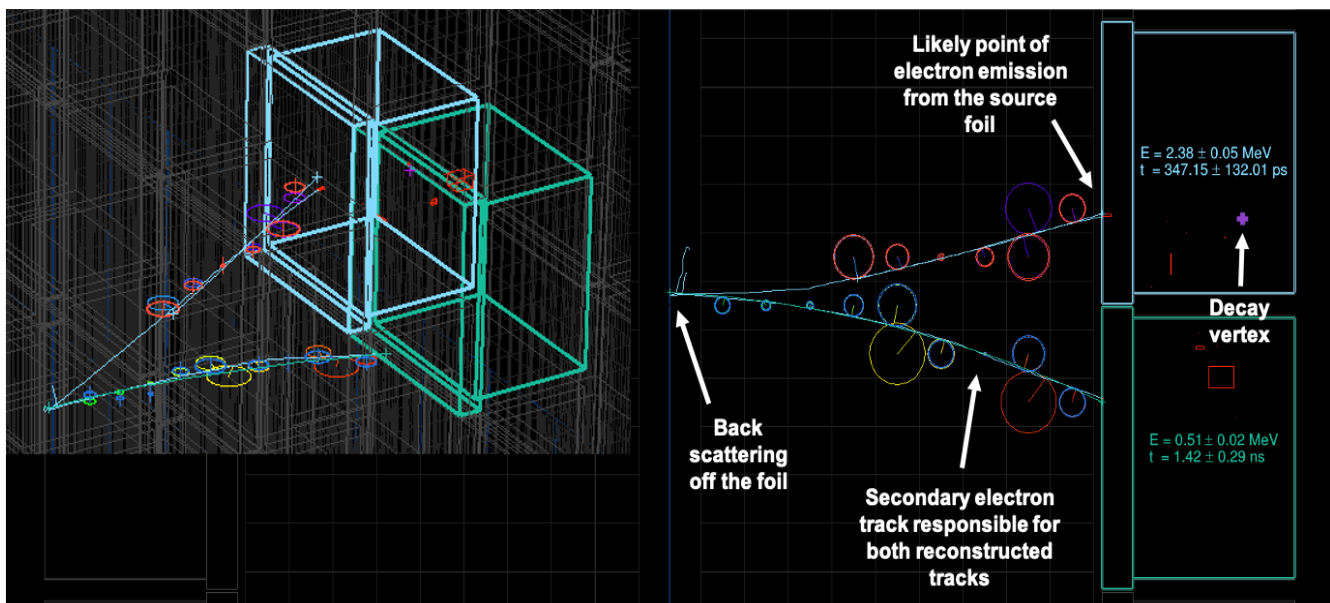


Figure 7.1: Event display illustrating the mechanism resulting in external  $^{208}\text{Tl}$  producing a double beta candidate event.


The mechanism resulting in the emission of the secondary electron is unclear as the interactions inside of the optical modules are often very complicated, although the electron is most likely to be emitted via Compton or low energy electron scattering. The emitted secondary electron is of low energy, but additional energy is provided by the primary photons, including the 2.6 MeV photon produced in almost all  $^{208}\text{Tl}$  decays as shown in figure 6.2. This additional energy is registered by either the initial or adjacent PMT, raising the total energy of the event into the  $^{82}\text{Se}$  ROI. Falaise only registers the timing of the first calorimeter hit, hence the initial primary decay inside the PMT provides the timing information for both calorimeters if energy is deposited during the initial decay. Therefore the separation in timing is determined by the time taken for energy to be deposited in the neighbouring calorimeter and not the time taken for the secondary electron to backscatter off the foil, allowing the events to pass the time of flight cuts (internal and external probability). This

combination of factors allows for external  $^{208}\text{Tl}$  events to pass all of the current cuts and contribute significantly towards the total background count, particularly for no field.


Therefore, to successfully generate a double beta candidate event from external  $^{208}\text{Tl}$ , the **incident secondary electron** must interact head on with the source foil so that the electron returns to the locale of the initial decay. For simulations on the X and G Veto wall PMTs, it is impossible for secondary electrons to strike the foil at an angle that can backscatter towards the initial vertex location because the X and G Veto walls do not face the exposed side of the source foil. Moreover, as the strength of the magnetic field increases, the number of double beta decay candidates generated from external  $^{208}\text{Tl}$  decays decreases as the probability of an electron backscattering off the foil and striking an adjacent calorimeter diminishes.

## 7.1 Background Optimization

As a result of the excessive number of expected events for external  $^{208}\text{Tl}$  on the 8" Main wall PMTs, further cuts are necessary for reducing the prevalence of the background. From chapter 6, external  $^{208}\text{Tl}$  was shown to represent over 90% of the total background for the no field scenario and increased the total background for no field to over 5 and 9 times the background count observed for the realistic and uniform field respectively. To explicitly target the external  $^{208}\text{Tl}$  background, three additional cuts were identified and include:

- i Setting a minimum opening angle for the 2e topology 
- ii Removing events with adjacent calorimeter hits
- iii Removing events in specific energies regions based on the decay scheme of  $^{208}\text{Tl}$

### 7.1.1 Minimum Opening Angle

As previously mentioned, pseudo double beta decays from background simulations, often results in 2e events with low opening angles. As shown in figure 5.3,  $0\nu\beta\beta$  follows a  **$1 - \cos\theta$  angular**  distribution, with the majority of events found at large angles. However, cutting on smaller angles does still remove a significant number of signal events so it pertinent to measure if there is an overall improvement in sensitivity when cutting out double beta candidate events with small angles. From the angular distributions shown in figures 7.2a and 7.2b the proportion of events at lower angles ( $\cos\theta \approx 1$ ) is greater for the backgrounds, particularly, external  $^{208}\text{Tl}$ . Cutting out events at low angles should disproportionately target these backgrounds whilst maintaining a high  $0\nu\beta\beta$  detection efficiency. The angular distributions for internal backgrounds is less skewed to lower angles (figure 7.3), relative to the radon and external contaminations, therefore they are not expected to have as many events removed at low angles.

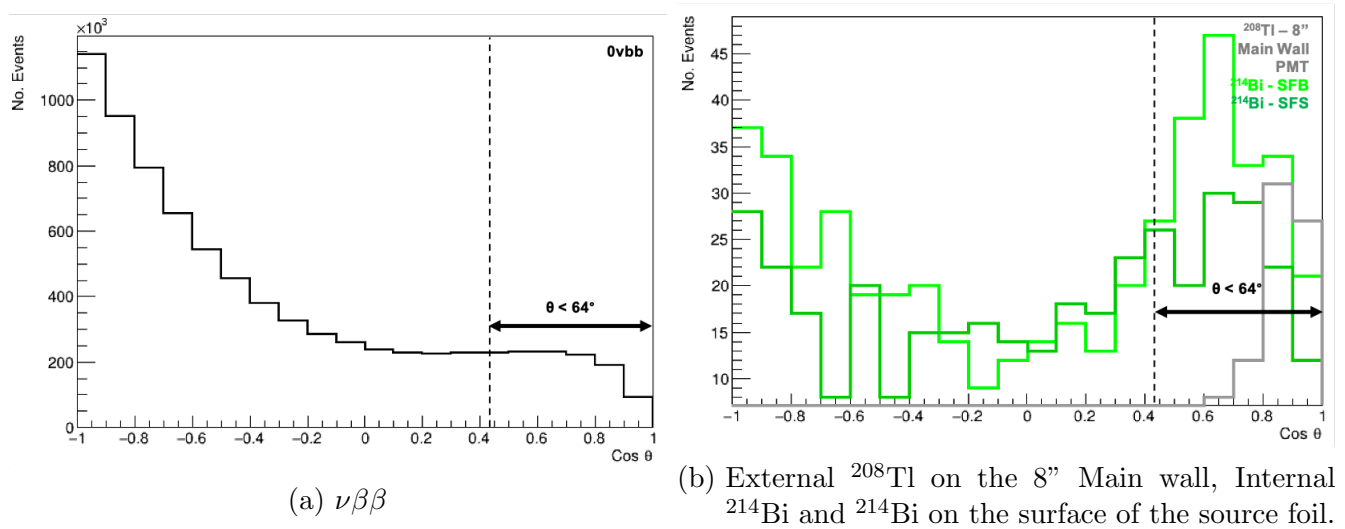


Figure 7.2: No field angular distributions for signal and backgrounds, including the **theoretical** maximum angle for two charged particles striking adjacent calorimeters (dashed line).

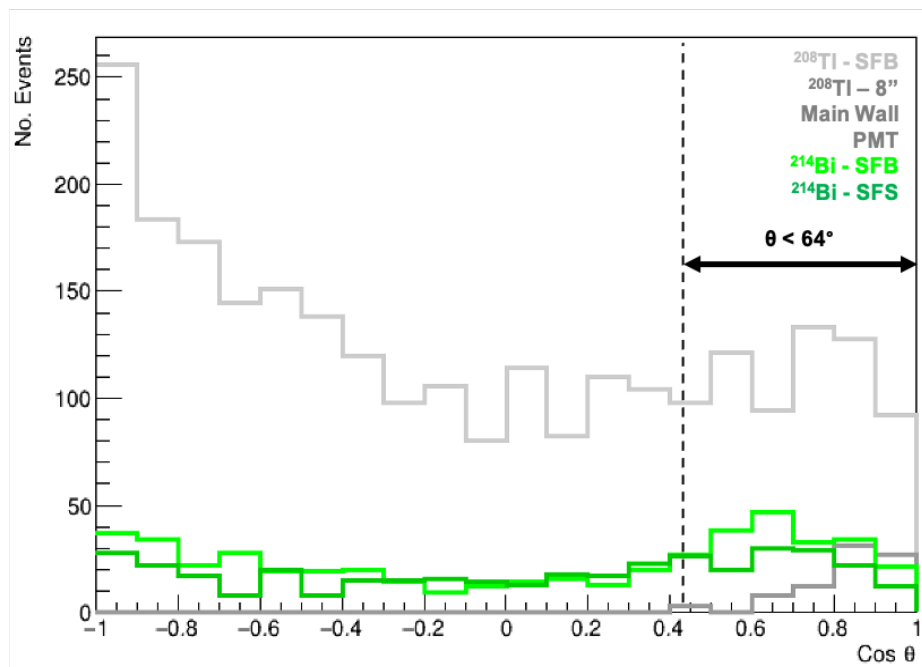


Figure 7.3:  $\text{Cos } \theta$  distribution for different backgrounds, including the **theoretical** maximum angle for two charged particles striking adjacent calorimeters (dashed line).

### 7.1.2 Minimum Angle Optimization

Prior to applying the minimum angle cut, the optimum angle was first determined by investigating a number of different minimum angles, ranging from  $0^\circ$  (no minimum angle), to  $100^\circ$ , increasing

in increments of  $10^\circ$ . The signal detection efficiency and background contributions was measured for each of the minimum opening angles and a simple Gaussian approximation (displayed in section ??) was used to plot figure 7.4 below.

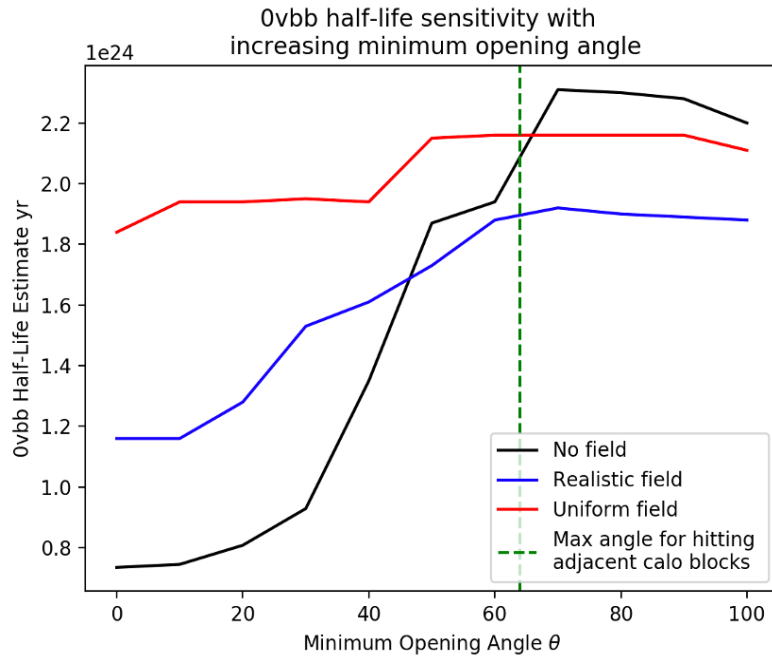


Figure 7.4: Minimum opening angle vs sensitivity for the three magnetic field configurations. Maximal sensitivity is achieved around a minimum angle of  $70^\circ$ .

For all three magnetic fields, the sensitivity to  $^{82}\text{Se } 0\nu\beta\beta$  was shown to increase as the minimum opening angle increased, until  $70^\circ$ , following which the sensitivity plateaus. Angles above  $100^\circ$  were not considered as they would begin to remove excessive amounts of signal events (figure 7.2a). The increase in sensitivity with increasing minimum opening angle was most abrupt for no field as the excessive number of low angle external  $^{208}\text{Tl}$  are removed, unlike the uniform and realistic fields which have much lower contributions from external  $^{208}\text{Tl}$ . At higher angles ( $>50^\circ$ ), the cut removes a greater number of internal backgrounds but also begins to remove a significant number of signal events resulting in the sensitivity plateauing.

For no field and the realistic field, as the minimum angle increases, the internal backgrounds become the dominant background as the external contribution is removed. At around  $70^\circ$ , the number of external backgrounds for all three magnetic fields is reduced to zero, corresponding to the peak sensitivities. From this we can assert that the optimum minimum opening angle cut should be between  $65^\circ$  and  $75^\circ$  and is the consensus for all three magnetic fields. At higher angles, the reduction in signal limits any improvement in sensitivity and at angles below  $65^\circ$ , the external backgrounds, particularly for no field and the realistic field, significantly degrade the sensitivity.

### 7.1.3 No Adjacent Calorimeter Hits

Double beta candidate events generated by external  $^{208}\text{Tl}$  are primarily low angle events, often resulting in events with hits in adjacent calorimeters. Adjacent calorimeter events are described as events with a second calorimeter hit, occurring in any of the horizontally, vertically or diagonally neighbouring calorimeters, to the first hit. A visual description of adjacent calorimeter hits is shown in figure 7.5 below. The dashed line in figures 7.2a-7.3, around  $64^\circ$ , represents the maximum **theoretical** angle for events with adjacent calorimeter hits, which is calculated using the angle between two maximally separated and diagonally adjacent calorimeter hits.

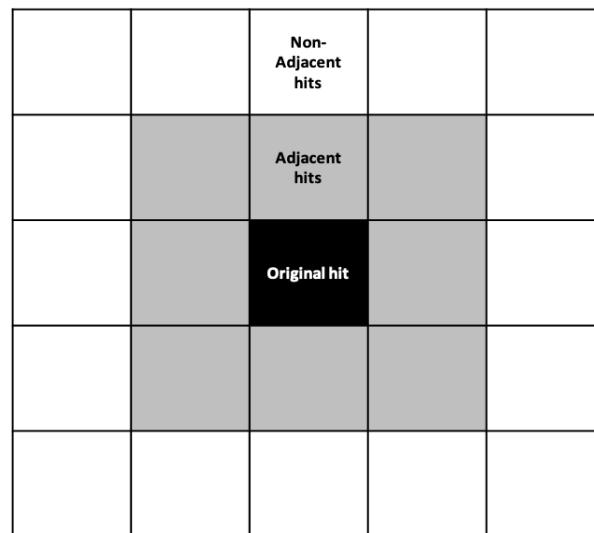


Figure 7.5: Illustration of the adjacent calorimeter hit definition. Any hit within a block horizontally, vertically or diagonally **adjCENT adjacent** to the original hit is labelled an adjacent calorimeter hit.

Removing events with hits in adjacent calorimeters provides an alternate approach to the minimum opening angle cut, in the hopes of removing the external backgrounds without significantly reducing the signal detection efficiency. Evidently, there will be a large overlap between the low angle and adjacent calorimeter events, although, the orientation of the reconstructed electrons emitted from the foil can result in low angle events hitting non-adjacent calorimeters. By explicitly targeting the adjacent calorimeter hits commonplace with external  $^{208}\text{Tl}$  2e events, the number of backgrounds may be reduced without reducing the signal efficiency as much as the angle cut. **Preserving the detection efficiency whilst reducing the background count is guaranteed to result in an increase sensitivity.**

The adjacent calorimeter cut had to be uniquely implemented into Sensitivity Module using multiple Falaise functions that extracted data from the various data banks. To determine whether an event consists of two adjacent calorimeter hits, the unique geometry identifier (GID) (found in the Falaise data banks 4.1) for the first calorimeter is extracted by the GetGID function. The

unique GID is then inputted into the GetNeighbourGIDs function, which provided the GIDs for all neighbouring calorimeters. If the second calorimeter hit GID matches one of the neighbouring GIDs, the event is designated as having an adjacent calorimeter hit.

#### 7.1.4 Tl Energy Split

$^{208}\text{Tl}$  beta decay occurs through the excited state of  $^{208}\text{Pb}$  with the emission of a 2.615 MeV photon (figure 6.2). As a result, there is an increased energy separation between the higher and lower energy calorimeter hits compared to  $0\nu\beta\beta$ , therefore, by exploiting this energy separation it may be possible to explicitly target the problematic external  $^{208}\text{Tl}$  background.

From [33], multiple exclusionary energy regions were selected for targeting  $^{208}\text{Tl}$  backgrounds. Upper and lower regions were identified, for the higher and lower electron energies respectively. For the purpose of this optimization process, the exclusion region for the lower energy electron was set as 0.2-0.9 MeV and for the higher energy electron, the exclusion region included electrons with energy between 2.3-2.59 MeV. Events with both the higher and lower energy electrons outside of these regions, pass the cut and contribute towards the total background count. From previous investigations for NEMO-2 and NEMO-3, this selective cut was shown not to result in an improved sensitivity for  $^{100}\text{Mo}$  neutrinoless double beta decay. The decay energy for  $^{82}\text{Se}$  is similar to  $^{100}\text{Mo}$  (table 3.2) and so the exclusionary energy regions are applicable for SuperNEMO.

### 7.1.5 Optimization Results

Similar to the minimum angle cut, the adjacent calorimeter hit cut was retrospectively applied to both signal and background to determine the influence of the cut on the sensitivity to neutrinoless double beta decay, for the three magnetic field configurations. Unlike the minimum angle cut, cut optimization was not required.

	$0\nu\beta\beta$ Detection Efficiency		
	Uniform Field	No Field	Realistic Field
Prior to optimization	0.0653	0.0790	0.0537
Angle $>70^\circ$	0.0551	0.0666	0.0451
No adjacent hits	0.0619	0.0754	0.0510
Tl energy separation	-	0.0470	-

Table 14:  $0\nu\beta\beta$  detection efficiency before and after the different optimization cuts.

Table 14 provides the detection efficiency of  $0\nu\beta\beta$  before and after the different optimization cuts. The highest detection efficiency, for all three magnetic field configurations, is with no additional cut and the lowest detection efficiency is observed with the  $^{208}\text{Tl}$  separation. Additionally, the  $^{208}\text{Tl}$  separation cut produces the highest number of expected backgrounds (table 15) whilst the minimum angle and adjacent calorimeter cuts successfully remove the external  $^{208}\text{Tl}$  events, significantly reducing the total background count.

Total Background Expected Events	Magnetic Field		
	Uniform Field	No Field	Realistic Field
Prior to optimization	2.92	28.4	4.92
Minimum Angle $70^\circ$	1.53	1.89	1.31
No adjacent hits	1.98	3.54	1.78
Tl energy separation	-	12	-

Table 15: Number of expected backgrounds before and after the different optimization cuts.





Although the detection efficiency of  $0\nu\beta\beta$  was reduced by the angle cut further than the adjacent calorimeter cut, the angle cut more successfully reduced the number of internal backgrounds. As show in figure 7.2b, there are a significant number of internal backgrounds at smaller angles and so the minimum angle cut is able to remove a greater number of backgrounds, whether internal, radon or external. Unlike the minimum angle cut, the adjacent calorimeter cut is more targeted towards removing external  $^{208}\text{Tl}$ , which generates double beta candidate events with adjacent hits.

The minimum angle cut brought about the highest sensitivity for all three magnetic fields. Most notably, the increase in sensitivity for no field, as a result of the reduced background, makes it the magnetic field with the highest sensitivity. Removing the adjacent calorimeter hits also significantly improved the sensitivity, however the increased detection efficiency vs the minimum angle cut is outweighed by the higher background count, which continues to encompass a small number of external  $^{208}\text{Tl}$  events. Removing adjacent calorimeter events does not reduce the internal and external backgrounds at the same rate as the minimum angle cut, resulting in a higher background count. Applying the  $^{208}\text{Tl}$  energy separation optimization to the MC data reduces the total backgrounds from all sources, however the detection efficiency of  $0\nu\beta\beta$  is also reduced to roughly 60% of the original value. Critically, the energy separation cut fails to remove the majority of the remaining external  $^{208}\text{Tl}$ .

### 7.1.6 Window Region Optimization

Throughout this work, the region of interest for  $^{82}\text{Se}$  neutrinoless was stated as 2.8-3.2 MeV as a consequence of the 3 MeV  $^{82}\text{Se}$  decay energy. However it is possible to fine tune this window region to maximise the expected sensitivity. To optimize the ROI window, the lower end of the ROI was shifted from 2.8 MeV to 2.6 MeV in increments of 0.05 MeV and at the same time the upper limit was shifted from 3.2 MeV to 3 MeV. With each changing ROI, the sensitivity was calculated after applying all cuts as well as the additional minimum angle optimization cut, which produced the highest sensitivity as shown in the previous section. Additionally the window optimization was only complete for the no field scenario. \*\*\* subject to change \*\*\*.

From the table above, the energy region shown to have the highest sensitivity is the 2.7-3.1 MeV region. This is mostly a result of the much greater detection efficiency for  $0\nu\beta\beta$  at this lower energy region whilst still suppressing the background contamination, in particular, from the problematic external  $^{208}\text{Tl}$ . The peak of the  $0\nu\beta\beta$  spectrum is between 2.7-3 MeV, however after 3 MeV number of successfully reconstructed events rapidly drops off and so shifting the ROI closer to 2.7 MeV increased the total number of reconstructed  $0\nu\beta\beta$  events in the energy region without equally increasing the number of expected backgrounds.

Below the 2.7 - 3.1 energy region, the increase in backgrounds is largely a result of an increase in the number of internal  $^{214}\text{Bi}$  events as the contamination level of internal  $^{208}\text{Tl}$  remains stable. Similar to  $0\nu\beta\beta$ , the top end of the energy distribution is within the 2.8 - 3.2 MeV region (figure

Region of interest MeV	Signal Efficiency	Expected Backgrounds	Sensitivity $\times 10^{24}$ yr.
2.80 - 3.20	0.0666	$1.890 \pm 3.59\%$	2.289
2.75 - 3.15	0.0989	$3.279 \pm 8.29\%$	2.581
2.70 - 3.10	0.1261	$6.201 \pm 7.08\%$	2.393
2.65 - 3.05	0.1464	$11.677 \pm 5.19\%$	2.024
2.60 - 3.00	0.1609	$24.22 \pm 3.69\%$	1.545

Table 16: Signal detection efficiency, number of expected events and sensitivity to  $0\nu\beta\beta$  for different regions of interest in the range from 2.6 to 3.2 MeV. Values provided are for the no field scenario after the additional minimum angle optimization.

??) and so by reducing the lower limit of the region of interest the number of  $^{214}\text{Bi}$  backgrounds increases significantly. Whereas for internal  $^{208}\text{Tl}$ , the number of backgrounds around the original region of interest remains constant and so by moving the ROI to lower energies the contribution from internal  $^{208}\text{Tl}$  remains steady.

ROI MeV	No. Of Expected Events			
	Internal $^{208}\text{Tl}$	Internal $^{214}\text{Bi}$	External $^{208}\text{Tl}$	$2\nu\beta\beta$
2.80 - 3.20	$0.774 \pm 2.40\%$	$1.036 \pm 6.10\%$	0	$0.02 \pm 70.71\%$
2.75 - 3.15	$0.789 \pm 2.33\%$	$1.757 \pm 4.71\%$	$0.214 \pm 100\%$	$0.600 \pm 28.87\%$
2.70 - 3.10	$0.788 \pm 2.33\%$	$2.894 \pm 3.67\%$	$0.427 \pm 70.71\%$	$2.249 \pm 14.91\%$
2.65 - 3.05	$0.779 \pm 2.35\%$	$4.498 \pm 2.94\%$	$0.427 \pm 70.71\%$	$7.247 \pm 8.30\%$
2.60 - 3.00	$0.776 \pm 2.35\%$	$6.602 \pm 2.43\%$	$0.214 \pm 100\%$	$20.341 \pm 4.96\%$

Table 17: Number of expected events for the most significant backgrounds as a with changing ROI

In the 2.8-3.2 MeV there is no external  $^{208}\text{Tl}$  contribution, but when reducing the energy limits of the window a smaller number of external  $^{208}\text{Tl}$  events ( $<2$ ) were found although they are completely drowned out by the internal background contributions.

From the window or region of interest optimization, the energy window giving the greatest sensitivity to  $^{82}\text{Se}$  neutrinoless double beta decay is the region between 2.7 and 3.1 MeV. Predominantly,

this is the case because below this region, the increase in background, particularly  $^{214}\text{Bi}$ , is no longer offset by the increase in the signal detection efficiency from moving the energy window closer to the bulk of the signal energy spectrum. Below 2.6 MeV, the energy window no longer encapsulates the decay energy of  $^{82}\text{Se}$   $0\nu\beta\beta$ . As mentioned previously, one of the benefits of using  $^{82}\text{Se}$  as a double beta decay isotope, is that the relatively high decay energy removes a lot of the lower energy backgrounds that may plight lower energy double beta decay searches.

Simultaneously, the width of the window was also subject to change and the sensitivity measured. Using tables 16 and 17, the minimum energy was set to 2.7 MeV and the ROI ranged from 0.15 to 0.5 MeV. As shown in table 17, below 2.7 MeV the contribution from  $2\nu\beta\beta$  begins to rapidly increase and becomes the dominant background. 0.15 MeV was selected as the narrowest ROI as a result of the calorimeter resolution, which is approximately 6% at the  $^{82}\text{Se}$  decay energy. The results of the different ROI widths are shown in table 18.

Region of interest MeV	Signal Efficiency	Expected Backgrounds	Sensitivity $\times 10^{24}$ yr.
2.70 - 3.20	0.1261	6.396 $\pm$ -%	2.401
2.70 - 3.15	0.1261	6.298 $\pm$ -%	2.429
2.70 - 3.10	0.1261	6.201 $\pm$ -%	2.448
2.70 - 3.05	0.1261	6.110 $\pm$ -%	2.466
2.70 - 3.00	0.1257	5.987 $\pm$ -%	2.483
2.70 - 2.95	0.1234	5.801 $\pm$ -%	2.476
2.70 - 2.90	0.1141	5.557 $\pm$ -%	2.340
2.70 - 2.85	0.0924	5.143 $\pm$ -%	1.969

Table 18: Signal detection efficiency, number of expected events and sensitivity to  $0\nu\beta\beta$  for different regions of interest in the range from 2.6 to 3.2 MeV. Values provided are for the no field scenario after the additional minimum angle optimization.

Above 3.05 MeV the increase in signal detection is minimal, whereas there is a small increase in the background count from internal  $^{208}\text{Tl}$ . Regardless, the sensitivity remains relatively stable above 2.70 to 3.00 MeV. Below the 3.00 MeV upper limit, the signal efficiency drops faster than the expected backgrounds resulting in a decrease in sensitivity. Using the data shown in tables 16-18, the optimal lower limit is around 2.70 MeV, below which the background count of  $2\nu\beta\beta$  and  $^{214}\text{Bi}$  exponentially increase. The upper limit is less prone to variations in sensitivity as the majority of the signal events are found below 3.05 MeV and increasing the upper limit of the ROI merely increases the internal  $^{208}\text{Tl}$  contamination.

### 7.1.7 Final Sensitivities For The Three Magnetic Fields

Three methods, Feldman-Cousins, Helene and MDA.

# Chapter 8

## Conclusion

Conclusion

A

# References

- [1] R. Davis, *A Review of the Homestake Solar Neutrino Experiment*, **Prog. Part. Nucl. Phys.**, **Vol. 32 (1994) 13-32**.
- [2] SNO Collaboration , A. Bellerive et al., *The Sudbury Neutrino Observatory*, **Nuclear Physics B (2016) arXiv:1602.02469v2 [nucl-ex]**.
- [3] B. Pontecorvo, *Mesonium and anti-mesonium*, **Sov.Phys.JETP 6 (1957) 429..**
- [4] B. Pontecorvo, *Inverse beta processes and nonconservation of lepton charge*, **Sov.Phys.JETP 7 (1958) 172–173**.
- [5] Z. Maki, M. Nakagawa, S. Sakata, *Remarks on the Unified Model of Elementary Particles*, **Progress of Theoretical Physics. 28, (1962) 870**.
- [6] P.A. Zyla et al.(Particle Data Group), *Prog. Theor. Exp. Phys.2020*, **083C01 (2020) and 2021 update**
- [7] X.Qian, P.Vogel, *Progress in Particle and Nuclear Physics*, **Vol. 83 (2015) 1–30**
- [8] P. F. de Salas, et al., *2020 Global reassessment of the neutrino oscillation picture* **arXiv:2006.11237**.
- [9] ATLAS Collaboration, *Combined measurements of Higgs boson production and decay using up to 80 fb<sup>-1</sup> of proton-proton collision data at  $\sqrt{s} = 13$  TeV collected with the ATLAS experiment*, **Phys. Rev. D 101 (2020) 012002**.
- [10] Majorana. E, *Teoria simmetrica dell’elettrone e del positrone*, **Nuovo Cim 14, (1937) 171**.
- [11] J. Angrik et al, *KATRIN design report 2004*, *KATRIN Collaboration*, **Technical report, KATRIN, 2005**.
- [12] M.Aker et al., *An improved upper limit on the neutrino mass from a direct kinematic method by KATRIN*, **arXiv:1909.06048v1 [hep-ex] (2019)**
- [13] M. Tanabashi et al., (*Particle Data Group*), **Phys. Rev.D 98, 030001 (2018)**.
- [14] S.R. Choudhury, S. Hannestad, *Updated results on neutrino mass and mass hierarchy from cosmology with Planck 2018 likelihoods*, **JCAP07(2020)037**.
- [15] A. Gando, et al., *Search for Majorana Neutrinos near the Inverted Mass Hierarchy Region with KamLAND-Zen*, **arXiv:1605.02889v2 [hep-ex] (2016)**

- [16] J.Mott, *Search for double beta decay of  $^{82}\text{Se}$  with the NEMO-3 detector and development of apparatus for low-level radon measurements for the SuperNEMO experiment*, **PhD Thesis, University College London (2013)**.
- [17] M. Goeppert-Mayer, *Double Beta-Disintegration*, **Phys. Rev.** **48**, (1935).
- [18] L. Simard, *The NEMO-3 results after completion of data taking*, **J. Phys. Conf. Ser.**, (2012) **375:042011**
- [19] M. Mirea et al, *Phase Space Factors for Double Beta Decay: an up-date*, **arXiv:1411.5506 [nucl-th] (2015)**
- [20] G. Racah, *On the symmetry of particle and antiparticle*, **Nuovo Cim.** **14** (1937) **322–328**.
- [21] W. H. Furry, *On Transition Probabilities in Double Beta-Disintegration*, **Phys. Rev.** **56** (1939), **1184-1193**.
- [22] J. Schechter, J. Valle, *Neutrino Masses in  $SU(2) \times U(1)$  Theories*, **Phys.Rev.** **D22** (1980) **2227**.
- [23] M. Doi, T. Kotani, H. Nishiura, E. Takasugi *DOUBLE BETA DECAY*, **Prog.Theor.Phys.** **69** (1983) **602**.
- [24] A. K. Chopra, *Construction and commissioning of the tracker for the SuperNEMO Demonstrator Module and unfolding the  $2\nu\beta\beta$  spectrum of  $^{100}\text{Mo}$  from the NEMO-3 experiment*.
- [25] N. Fatemi-Ghomi, *Measurement of the double beta decay half-life of  $^{150}\text{Nd}$  and search for neutrinoless decay modes with NEMO-3 detector*, (2009) **arXiv:0905.0822 [hep-ex]**.
- [26] SuperNEMO Collaboration, R. Arnold et al, *Probing New Physics Models of Neutrinoless Double Beta Decay with SuperNEMO*, **Eur.Phys.J.** **C70** (2010) **927–943**, **arXiv:1005.1241 [hep-ex]**
- [27] O. Ponkratenko, V. Tretyak, Y. Zdesenko, *The Event generator DECAY4 for simulation of double beta processes and decay of radioactive nuclei*, **Phys.Atom.Nucl.** **63** (2000) **1282–1287**, **arXiv:nucl-ex/0104018 [nucl-ex]**.
- [28] S. Agostinelli, et al., *Geant4—a simulation toolkit*, **Nuclear Instruments and Methods in Physics Research A** **506** (2003) **250–303**.
- [29] O. Helene, *Upper Limit of Peak Area*, **Nuclear Instruments and Methods in Physics** **212** (1983) **319**.
- [30] G. J. Feldman, R. D. Cousins, *A Unified Approach to the Classical Statistical Analysis of Small Signals*, **Phys.Rev.D****57:3873-3889** (1998) **arXiv:physics/9711021v2 [physics.data-an]**
- [31] D. Bourssette, *Neutrino physics with SoLid and SuperNEMO experiments.*, **High Energy Physics - Experiment [hep-ex]**. **Université Paris-Saclay, (2018)**. English.



- 
- [32] D. L. Hall, *Development of a simulation model for the SuperNEMO tracker module*, PhD thesis, University of Manchester, 2012.`.text`
- [33] R. Arnold, et al., *Possible background reductions in double beta decay experiments*, **Nuclear Instruments and Methods in Physics Research A** **503** (2003) **649-657**.